MONASH University

Compression of Fatigue Spectra for Composite Materials

Rowan Andrew Healey

B. Eng (Mechanical) Hons & B.Sc (Applied Mathematics)

A thesis submitted for the degree of *Doctor of Philosophy* at
Monash University, in 2022
Department of Mechanical and Aerospace Engineering

Abstract

Variable amplitude fatigue testing is a time consuming process and a necessary part of certification for aircraft structures. While the frequency of loading can be increased for testing metals, for composites this approach is limited due to heating effects. Hence it is more pertinent to develop effective methods for reducing/compressing fatigue test spectra for composite structures. Effective spectrum reduction techniques mainly include a spectrum truncation method which removes load cycles that negligibly effect fatigue damage initiation/growth, and a cycle merging method that combines cycles to form a cycle with the equivalent effect on fatigue damage initiation/growth. Application of these methods requires understanding of the fatigue mechanisms. These techniques have seen wide use for metallic structures, with comparatively small amounts of literature existing for composite materials. For composites this is more complex due to their non-isotropic, non-homogeneous, multi-failure mode characters. Due to the lack of research concerning spectrum reduction for composites, there are no widely accepted simplification approaches with the exception of omitting low stress levels.

In this study a ground up approach was taken to develop a spectrum simplification methodology which was utilised with unidirectional and woven specimens undergoing mode II delamination. Residual strength and crack growth rate models were developed from constant amplitude fatigue data, which informed the application of truncation and cycle merging. Experimental results showed good agreement with predictions for the truncation sequences which achieved damage conservative length reductions of 77% and 74% for the unidirectional and woven specimens respectively. However, the application of solely cycle merging revealed several factors which resulted in notable changes to spectrums damage content including: the merging algorithm and the equivalent damage

calculations. Through adjustment of the cycle merging algorithm and by first performing truncation to omit large numbers of non-damaging cycles which contributing to rounding errors, cycle merging was successfully implemented achieving a 95% reduction in spectrums length with similar fidelity to the uncompressed spectrum. The application of iterative scaling following cycle merging allowed for damage to be re-introduced/removed into the spectrum, enabling the damage content to be matched with the original spectrum.

Declaration

This thesis contains no material which has been accepted for the award of any other degree or diploma at any university or equivalent institution and that, to the best of my knowledge and belief, this thesis contains no material previously published or written by another person, except where due reference is made in the text of the thesis.

Signature: ……

Print Name: …….

Date: …….

Publications during enrolment

Healey, R., Chowdhury, N.M., Chiu, W.K. and Wang, J., 2019. Experimental and numerical determination of mode II fracture toughness of woven composites verified through unidirectional composite test data. *Polymers and Polymer Composites*, *27*(9), pp.557-566.

Chowdhury, N.M., Healey, R., Wang, J., Chiu, W.K. and Wallbrink, C., 2020. Using a residual strength model to predict mode II delamination failure of composite materials under block fatigue loading. *International Journal of Fatigue*, *135*, p.105563.

Healey, R., Wang, J., Wallbrink, C. and Chiu, W.K., 2021. Predicting mode II delamination growth of composite materials to assist simplification of fatigue spectra by truncating non-damaging cycles validated with experiment. *International Journal of Fatigue*, *145*, p.106117.

Healey, R., Wang, J., Chiu, W.K., Chowdhury, N.M., Baker, A. and Wallbrink, C., 2021. A Review on Aircraft Spectra Simplification Techniques for Composite Structures. *Composites Part C: Open Access*, p.100131.

Healey, R., Wang, J., Wallbrink, C., Chiu, W.K. and Xu, Z., 2021. The application of cycle merging and an extension of a fatigue spectrum simplification methodology from unidirectional to woven composite materials, *International Journal of Fatigue*, Under Review

Chowdhury, N.M., Chiu, W.K., Wallbrink, C., Wang, J. and Healey, R., 2019. Towards accelerated mode II variable amplitude fatigue testing for composite materials. In *AIAC18: 18th Australian International Aerospace Congress (2019): HUMS-11th Defence Science and Technology (DST) International Conference on Health and Usage Monitoring (HUMS 2019): ISSFD-27th International Symposium on Space Flight Dynamics (ISSFD)* (p. 450). Engineers Australia, Royal Aeronautical Society.

Healey, R., Chowdhury, N.M., Chiu, W.K. and Wang, J., 2019. Experimental and numerical determination of the mode II fracture toughness of woven composites. In *ICCM22 2019* (pp. 3721-3729). Melbourne, VIC: Engineers Australia.

Acknowledgements

I would like to express my gratitude and thanks to my supervisors, Professor Wing Kong Chiu and Dr John Wang from Defence Science and Technology Group, for their support and guidance throughout my candidature. Their expertise was invaluable and their approachability made this an enjoyable experience. I would like to thank Dr Chris Wallbrink for his technical guidance and feedback.

I would also like to thank Mr Alan Coram from the Institute of Railway and Technology for access to the servo-hydraulic machines located in the High Bay area as well as the support he provided with operation and troubleshooting. I would also like to extend my appreciation to Mr Chris Pierson and the other Mechanical and Aerospace Engineering Workshop Staff for manufacturing the reversible three point bending fixture and assisting with specimen machining.

I would like to acknowledge the Dr Jinan Cao from Fortburn for manufacturing the composite specimens and Dr Zhou Xu for the use of the instruments and scientific and technical assistance at the Monash Centre for Electron Microscopy.

This research was partially funded by Capability Acquisition and Sustainment Group, Australian Department of Defence. This research was supported by an Australian Government Research Training Program (RTP) Scholarship.

Lastly, I would like to give thanks to my family. Thank you to my loving parents who have provided me with the support that has enabled me to complete this thesis.

Contents

List of Figures

List of Tables

Nomenclature

Symbol	Description
α, β	Parameters obtained by fitting static strength and constant amplitude data to equation 2.32
Γ	Arbitrary contour
δ, γ	Shape and scale parameters of equation 2.31
$\delta_{max}, \delta_{min}$	Maximum displacement level, minimum displacement level
θ	Angle the crack propagates along relative to the initial crack tip
κ	Adjusted dependant on plane stress and plane strain
μ	Shear modulus
μ_f	Fitting parameter for G_{eq} equation (4.8)
ν	Poisson's ratio
$\sigma_a,\ \sigma_{min},\ \sigma_{max}$	Alternating stress, minimum stress, maximum stress
σ_r, σ_0	Residual strength, static/virgin strength
σ_{ar}	Equivalent completely reversed stress amplitude
σ_u	Ultimate tensile strength
σ_m	Mean stress
σ^2	Standard deviation
A, m	Fitting parameters for compliance calibration equation (4.1)
A_w, b_w, γ_w	Fitting parameters for the Walker equation (2.16)
a	Crack length
a_0	Initial crack length
a_t	Crack length after which the effects of the Teflon insert were negligible

Symbol	Description
B	Specimen width
b	Fatigue strength exponent
C	Compliance
C_p, m_p	Fitting parameters for Paris' law (2.36)
C_0, C_1, C_2, C_3	Constants of cubic polynomial for determining compliance equation (2.6)
D	Total damage
D_p, n_p	Fitting parameters for crack growth rate equation (4.9)
da/dN	Crack growth rate
E	Young's modulus
E_{11}	In-plane Young's modulus in 1-material direction
E_{22}	In-plane Young's modulus in 2-material direction
E_{adj}	Adjustment factor which aligns crack growth rate data (for $a < a_t$)
F_{σ_0}, F_N	Cumulative distributions of in the initial strength and life respectively
G_{12}	In-plane shear modulus
G_{13}	Interlaminar shear modulus in the 1-3 plane
$G_{Ic}, G_{IIc}, G_{IIIc}$	Critical mode I, II and III interlaminar fracture toughness
$G, \Delta G$	Strain energy release rate, strain energy release rate range
ΔG_{II}	Mode II strain energy release rate range
$G_{max}, G_{II,max}$	Maximum strain energy release rate, maximum mode II strain energy release rate
$G_{II,max,adj}$	Adjusted value of maximum mode II strain energy release rate
G_{eq}	Equivalent strain energy release rate

Symbol	Description
$\Delta\sqrt{G_{thr}}$	The value of $\Delta\sqrt{G}$ at threshold
h	Specimen thickness
J	J integral
$K, \Delta K$	Stress intensity factor, stress intensity range
N	The number of load cycles
N_f	The number of load cycles until failure
P	Load level
P_{max}	Maximum load level
R	Stress ratio ($\sigma_{min}/\sigma_{max}$)
R_d	Amplitude ratio ($\delta_{min}/\delta_{max}$)
r	Distance between the crack tip and node immediately in front of the crack tip
r_d	Displacement level ($\delta_{max}/\delta_{static}$)
S	Applied stress range
T_i	Traction vector
U	Elastic strain energy
u_x, u_y	Horizontal and vertical displacement of nodes after application of loading
W	Strain energy density
x	Displacement

Acronyms

Abbreviation	Definition
ASTM	American Society for Testing Materials
CC	Compliance calibration
CGRM	Crack growth rate model
C-C	Compression-compression
C-T	Compression-tension
DBC	Double cantilever beam
ENF	End-notched flexural
FALSTAFF	the Fighter Aircraft Loading STAndard For Fatigue
FE, FEA	Finite element, finite element analysis
FRPMC	Fibre reinforced polymer matrix composites
GFRP	Glass fibre reinforced polymer
H-L/HL	High to low amplitude (block loading sequence)
L-H/LH	Low to high amplitude (block loading sequence)
MERG-S	Cycle merging where segments are replaced with a single turning point
MERG-B	Cycle merging where segments are replaced with a block of turning points
MTS	Material test suite
PCM	Polymer composite material
RSM	Residual strength model
SERR	Strain energy release rate

Abbreviation	Definition
SHCM	Sequential Half Cycle Method
SRFM	Segmented Rainflow Method
SWT	Smith-Watson-Topper
S-N	Stress-life
T-C	Tension-compression
T-T	Tension-tension
UCS	Ultimate compressive strength
UTS	Ultimate tensile strength
VA	Variable amplitude
VCCT	Virtual crack closure technique

Chapter 1

Introduction

1.1 Background

The move towards light-weight, high-stiffness structures has led to the replacement of metallic materials with fibre reinforced polymer composites. This trend has led to further challenges in regard to certification and through-life support as damage mechanisms in composites differ significantly from those in metals. In order to make informed safe-life predictions for composite materials a robust understanding of both fatigue characteristics and damage growth behaviour is required.

For aircraft certification testing procedures, variable amplitude fatigue spectra are taken from in-service structures. As these sequences commonly consist of high numbers of turning points this results in long test times and significant expenses. While the frequency of loading can be increased for testing metals, for composites this approach is limited due to heating effects. Hence

it is more pertinent to develop effective methods for reducing/compressing fatigue test spectra for composite structures. Effective spectrum reduction techniques mainly include a spectrum truncation method which removes load cycles that negligibly effect fatigue damage initiation/growth, and a cycle merging method that combines cycles to form a cycle with the equivalent effect on fatigue damage initiation/growth. Application of these methods requires understanding of the fatigue mechanisms. These techniques have seen wide use for metallic structures, with comparatively small amounts of literature existing for composite materials. For composites this is more complex due to their non-isotropic, non-homogeneous, multi-failure mode characteristics. Due to the lack of research concerning spectrum reduction for composites, there are no widely accepted simplification approaches with the exception of omitting low stress levels. Research is therefore required to develop and test methods for accelerating variable amplitude fatigue tests for composite aircraft structures.

1.2 Research Objectives

The purpose of this research was to develop a methodology to conservatively compress a fatigue spectrum which was used to load composite specimens. Spectrum reduction for composite materials is a field which has seen limited work especially when compared to the plethora of literature examining reduction techniques for metallic materials [1].

Due to the complexity associated with composite layups and the numerous combinations of reinforcement and matrix, the importance of a general procedure with flexibility cannot be understated. To illustrate the generality of the detailed work the methodology was first performed on a relatively simple unidirectional composite specimen, after which an extension was made to a woven specimen type with a more complex layup.

Spectrum reduction techniques such as truncation and cycle merging utilise an estimated damage associated with each cycle within a sequence. To calculate such a measure accurately a robust damage prediction model is required, which needs considerable amounts of experimental data

from a broad range of loading values. A ground up approach was therefore taken starting with static testing before progressing to constant amplitude fatigue testing. After which simple variable amplitude fatigue testing was performed in the form of block loading followed by loading under a variable amplitude spectrum.

Due to the significant amounts of error that can arise from failure prediction models, confirmation of a prospective model's accuracy is required at more simplistic loading conditions before progression to complex loading. Furthermore, damage conservation is a primary goal of reduction techniques (besides shortening sequences) ensuring that significant amounts of damage aren't removed, thereby preventing a new sequence from being created which no longer represents the original.

1.3 Thesis Structure

A review of published works examining composite materials, delamination and several analytical models is presented in Chapter 2. Mode II delamination is focussed on in this chapter with discussion of useful experimental measures and numerical methods for determining said measures. The two main forms of fatigue testing are explained with considerable efforts given to detailing numerous fatigue failure models utilised for composite materials, some being adapted from metallics. Two distinct modelling types are examined; damage models and crack propagation models, the development of each and their benefits/shortcomings are considered.

Several fatigue spectrum reduction techniques utilised in the field of metallics are discussed including the many successful conservative reductions that have been achieved. Application of these techniques to composite materials sees several promising findings when considering the possibility of small cycle omissions, but the relative lack of literature does highlight the need for further work.

In Chapter 3 the experimental processes and setups utilised in this thesis are detailed. Manufacturing and material information of the two types of composite specimens tested

(unidirectional and woven) are provided as well as batch comparisons. This chapter focusses on the main components of the test setup; the servo hydraulic machine, test fixture, camera, supports, measuring technique and accompanying software which all enable mode II delamination fatigue testing to be conducted.

Static, constant amplitude fatigue and simple variable amplitude fatigue testing for the unidirectional specimen type are detailed in Chapter 4, with the aim being to develop analytical model(s) for prediction of fatigue failure. Two types of model are developed; a residual strength model and a crack growth rate model, examining the benefits and shortcomings of both.

Chapter 5 utilises the modelling performed in Chapter 4 to reduce the length of selected fatigue spectrum through truncation/small cycle omission and cycle merging, with the methods from Chapter 4 being extended for the woven specimen. The adjustments of the original fatigue spectrum are detailed as well as the resulting characteristics.

Having achieved conservative compression of the selected fatigue spectra, Chapter 6 involves the addressing of several sources of error in the cycle merging procedure, including the combination of truncation and cycle merging to enable the creation of more representative sequences.

Conclusions from this thesis are summarised in Chapter 7. The major findings and contributions that this work adds to the fields of composite materials and aerospace will be highlighted. Recommendations for the scope of future research is offered within this chapter.

End of Chapter 1

Chapter 2

Literature Review

2.1 Introduction

The following chapter is a literature review of the established procedures for testing delamination properties of composite materials as well as a recounting of the current methods and theory behind fatigue testing and the various means by which damage can be modelled. With the later sections focusing on the reduction of fatigue spectra, detailing the methods implemented for metallic materials and the lack of general techniques for composite materials.

2.2 Delamination

A common type of composite failure occurs when two adjacent plies in a layup separate corresponding to matrix failure, it is known as delamination. It is of high importance when

considering damage tolerance as crack propagation brought upon by delamination is detrimental to the strength of the composite laminate, hence leading to reductions in a parts/structures life.

When considering the manner in which delamination can occur there are three distinct modes (Figure 2.1), mode I (opening/tensile), mode II (In-plane shearing), mode III (Out of plane shearing), or a combination of the three modes which is referred to as, mixed mode delamination.

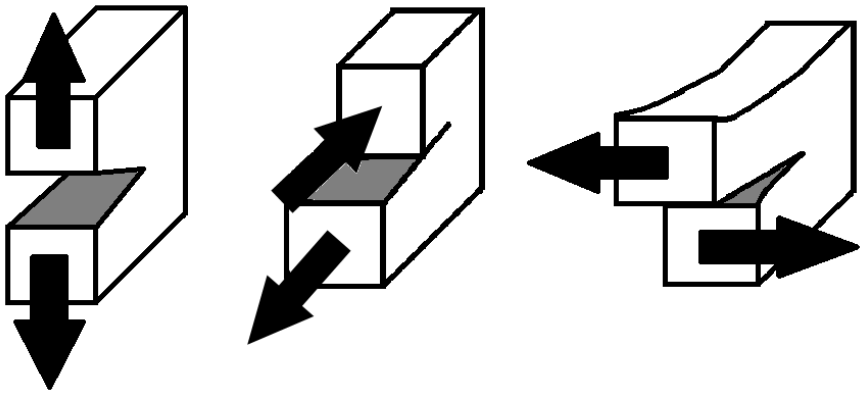

(a) (b) (c)

Figure 2-1 Visual Representation of Mode (a) I, (b) II and (c) III delamination

A measure known as the critical strain energy release rate (G_c) is generally accepted as a means for determining the total amount of energy required to propagate an existing crack. Depending on the mode of delamination being examined this property may be expressed as $G_{Ic}, G_{IIc}, G_{IIIc}$ to refer to the corresponding value of G_c.

Much work has been done to accurately measure G_c for fibre reinforced polymer matrix composites (FRPMC), such that accepted testing methodologies and ASTM standards exist for testing each mode of delamination including mixed mode setups [2-6], a number of these standards have been designed for simple unidirectional carbon/glass fibre layups and accordingly have a limited scope. Mode I setups consist of a double cantilever beam (DBC), where a rectangular shaped composite specimen is loaded by pulling the pre-cracked specimen apart, this can be achieved with piano hinges or loading blocks [6]. Mode II fracture testing involves static

testing of an end-notched flexure specimen (ENF) by a three point bend test rig [7] and Mode III delamination is tested by edge crack torsion tests.

The focus of this work is on Mode II delamination, hence only the three point bending test setup will be examined thoroughly.

2.2.1 Experimental Determination of Mode II Fracture Toughness

When conducting ENF testing, specimens are placed in a conventional three point bend test fixture with two support rollers and a single loading roller. The specimens are aligned such that the crack tip is a certain horizontal distance from the support roller located on the cracked length of the specimen (a). The distance between the support roller and load roller are set dependant on the ENF specimen being tested, the ASTM 7905 uses a half span length (horizontal distance from support roller to load roller) of 50mm, with a specified specimen width between 19mm and 26mm, a thickness of 3.4mm to 4.7mm and an initial crack length of at least 45mm (see Figure 2.2 and 2.3). Fabrication and machining of these ENF specimens is detailed in the ASTM D5687/D5687M [8], and is utilised by the ASTM 7905.

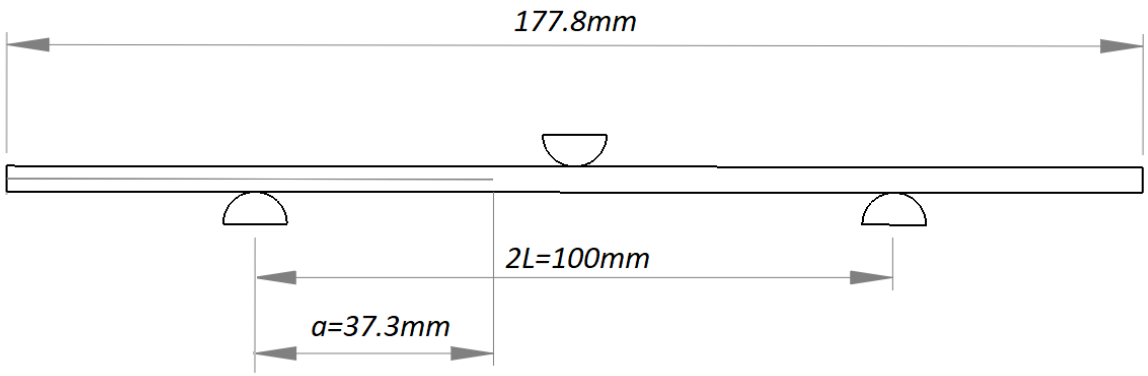

Figure 2-2 2D view of the specimen positioned in the three point bending setup with measurements corresponding to a crack length of 37.3mm

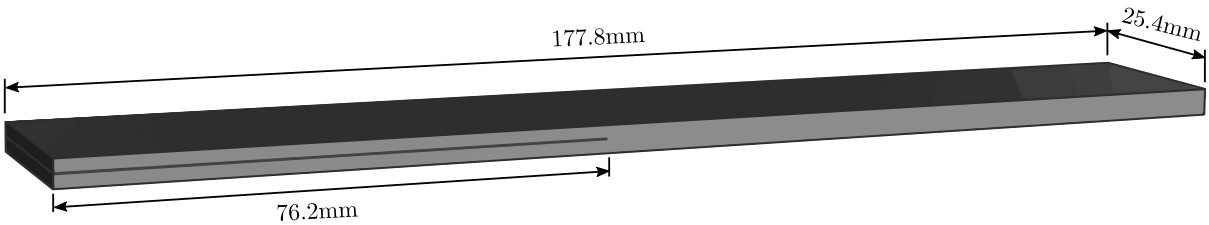

Figure 2-3 Detailed drawing/plan of ENF specimen (with pre-crack)

The value of a is then set and the specimens are statically loaded under displacement control by the loading roller on the top surface of the specimen while the two support rollers on the bottom side of the specimen provide the necessary support to enable bending to occur without slipping. From the beginning of the loading process to until the point at which the test is halted, displacement and force data is recorded. Using compliance calibration as detailed in the ASTM 7905 enables the determination of G_{IIc}.

To relate the compliance (*C*) to the strain energy release rate (SERR), the change in energy of a specimen as the crack grows needs to be considered [9]. A load, *P* will induce an elastic strain energy *U*,

$$U = \frac{1}{2}Px = \frac{1}{2}P^2C \qquad \text{Equation 2.1}$$

The solid will behave like a linear spring due to its elasticity, hence Equation 2.1 represents that of a spring. If the crack is now extended by distance δa, during said growth there will be an increase in load $(P + \delta P)$ and displacement $(x + \delta x)$ respectively. Similarly both the strain energy $(U + \delta U)$ and compliance $(C + \delta C)$ will increase. During the formation of the new crack surfaces energy will be released, this energy will be equivalent to the amount of potential energy removed from the specimen, hence Equation 2.2 represents this energy balance.

$$GB\delta a = -[(U + \delta U) - U - P\delta x] \qquad \text{Equation 2.2}$$

Where *G* is the SERR and *B* is the width of the specimen, hence $B\delta a$ represents the newly created crack area assuming a uniform crack front. Now by applying the relative changes due to the crack extension to Equation 2.2,

$$U + \delta U = \frac{1}{2}(C + \delta C)(P + \delta P)^2 \approx \frac{1}{2}CP^2 + CP\delta P + \frac{1}{2}\delta C P^2 \qquad \text{Equation 2.3}$$

Note that relatively small terms have been truncated, hence all terms which consisted of the product of two small changes in any variables (i.e. $\delta C\delta P, (\delta P)^2$) were removed. Performing a similar process for the change in displacement,

$$x + \delta x = (C + \delta C)(P + \delta P)$$

$$\rightarrow \delta x = (C + \delta C)(P + \delta P) - CP$$

$$\approx C\delta P + P\delta C \qquad \text{Equation 2.4}$$

By substituting Equations 2.3 and 2.4 into Equation 2.2,

$$GB\delta a = \frac{1}{2}P^2\delta C = \frac{1}{2}P^2\frac{dC}{da}\delta a$$

$$\rightarrow G = \frac{1}{2}\frac{P^2}{B}\frac{dC}{da} \qquad \text{Equation 2.5}$$

Therefore Equation 2.5 depicts how the energy release rate relates to the specimen compliance.

For a given crack length (a), by performing a linear least square curve fit to collected load-displacement data the resulting gradient can be utilised to calculate the compliance [10]. A series of *C vs a* data can then be modelled to one of many different equations which differ by the inclusion of lower order terms.

$$C = C_0 + C_1 a + C_2 a^2 + C_3 a^3 \qquad \text{Equation 2.6}$$

Where $C_0, C_1, C_2, and\ C_3$ are constants, Equation 2.6 is a cubic polynomial including all low order terms. A common form of this equation which was used by [10] and the ASTM7905 [7] omits the first and second order terms.

$$C = C_0 + C_3 a^3 \qquad \text{Equation 2.7}$$

By substituting Equation 2.7 into Equation 2.5 (SERR-compliance equation), the Mode II critical SERR is given by,

$$G_{IIc} = \frac{P^2}{2b}(3C_3 a^2) = \frac{3mP_{max}^2 a^2}{2B} \qquad \text{Equation 2.8}$$

Where the right hand side of Equation 2.8 corresponds to the form provided by the ASTM7905, with $C_3 = m \; and \; b = B$.

Use of the lower order terms has been shown to reduce associated error in measurements of *C*, A.B. Pereira et al [11] denoted the CC performed using Equation 2.7 as CC1 and the retention of the C_1 term resulted in a variation of Equation 2.7 referred to as CC2, utilising both models for G_{IIc} determination of glass/epoxy multidirectional laminates. Associated percentage error values were all less than ~5% for both CC1 and CC2 across four different layups, with the larger error predominantly residing with CC1.

2.2.2 Numerical Determination of Mode II Fracture Toughness

Virtual Crack Closure Technique (VCCT)

The virtual crack close technique (VCCT) is used to predict the propagation of a crack through the comparison of the local SERR and the critical SERR (G_c). In the finite element analysis software ABAQUS, VCCT is implemented through a contact interaction between two surfaces which represents the growing cracks path (Figure 2.4).

The base assumption of VCCT is that the energy released during the advance of a crack is equal to the energy required to close the crack by the length it progressed.

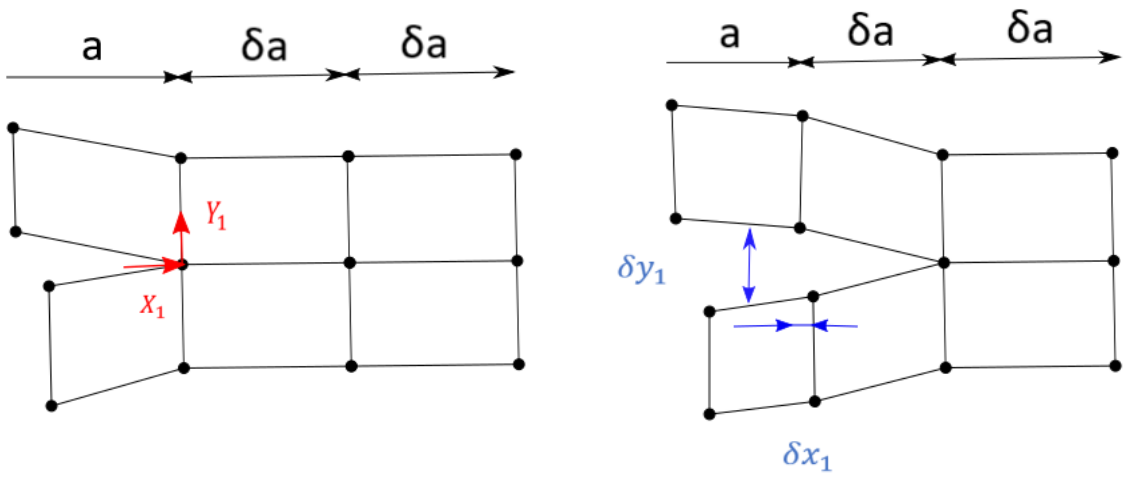

Figure 2-4 VCCT 2D where the forces X_1 and Y_1 close the crack after crack growth resulting in relative displacements of δx_1 and δy_1. Hence the energy required to grow a crack by length δa is equal to the energy required to close it by the same length

As previously mentioned a comparison is made between the local SERR and the interlaminar fracture toughness of the material to determine whether crack growth occurs or not. In the event that the local SERR exceeds the critical value the node representing the crack tip is released allowing for propagation. Stability is retained through the gradual release of the force at the crack tip before advance.

VCCT has been utilised in finite element (FE) simulations for the pure delamination modes: I [12-14], II [14-16] and III [17], as well as mixed modes [14, 18]. It is widely utilised when determining the interlaminar fracture toughness of separate modes due to its simplicity though it is very sensitive to mesh sizing and requires an initial crack [13].

J Integral

The J-Integral is a two-dimensional contour integral which encloses the crack tip, while possessing starting and finishing points on the crack faces (Figure 2.5). It is commonly used to determine the energy release rate observed with the growth of a crack. ABAQUS has an inbuilt user interface which enables J Integrals to be calculated, though the mesh close to and inside the

contour needs to be tailored for consistent results. ABAQUS requires that inside the contour a sweeping mesh algorithm is used.

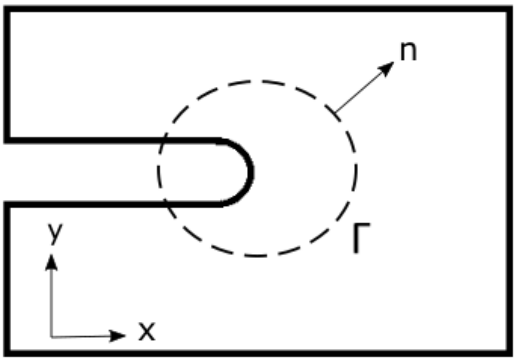

Figure 2-5 Diagram of the line integral known as a J-Integral, encompassing a notch in two dimensions.

The integral which was originally introduced by Rice [19] is defined as

$$J = \int_{\Gamma} \left(W dy - T_i \frac{\delta u}{\delta x} ds \right) \qquad \text{Equation 2.9}$$

Where $W = \int_0^{\varepsilon_{ij}} \sigma_{ij} d\varepsilon_{ij}$ is the strain energy density, $T_i = \sigma_{ij} n_j$ is the traction vector, Γ is an arbitrary contour around the crack tip, n is the unit vector normal to Γ, while $\sigma, \varepsilon,$ and u are the stress, strain and displacement field respectively and ds is the element of arc along the path Γ.

The J integral approach has displayed good agreement with the measurement techniques of ASTM standards [20, 21], hence bolstering it as a valid method for determining the interlaminar fracture toughness of composites.

Displacement Field

Displacement field utilises the relative change in the horizontal and vertical displacements of nodes after the application of loading. Through the measuring of displacements before and after loading the mode II interlaminar fracture toughness is determined by the following,

$$u_x = \frac{K_{II}}{8\mu\pi}\sqrt{2\pi r}\left[(2\kappa + 3)sin\frac{\theta}{2} + sin\frac{3\theta}{2}\right] \quad \text{Equation 2.10}$$

$$u_y = -\frac{K_{II}}{8\mu\pi}\sqrt{2\pi r}\left[(2\kappa - 3)cos\frac{\theta}{2} + cos\frac{3\theta}{2}\right] \quad \text{Equation 2.11}$$

Where r is the distance between the crack tip and nodes that are immediately in front of the crack tip along the direction of propagation, μ is the shear modulus, κ is and adjustment dependant on plane stress and plane strain, ν is Poisson's ratio, E is Young's modulus, θ is the angle the crack propagates along relative to the initial crack tip, u_x and u_y are the nodal displacement between two nodes in coincidence before crack propagation [22].

Chowdhury et al [23, 24] utilised the displacement field method through post nodal analysis to determine the strain energy release rate under Mode I and II for bonded and hybrid lap joints to compare fatigue performance.

2.3 Fatigue Testing

Materials undergo fatigue loading when being repeatedly loaded over a period of time, with strength properties decreasing while potentially resulting in wearout.

The process of fatiguing a structural component leads to cases where failure occurs at stress levels considerably lower than that of the materials ultimate strength. The degree to which fatigue damages a component is dependent on several factors, firstly the magnitude of the maximum applied stress (tensile or compressive) and the amplitude ratio (R_d) or stress ratio denoted by R.

$$R = \sigma_{min}/\sigma_{max} \quad \text{Equation 2.12}$$

This provides the means for determining another important factor: the magnitude of the oscillation in the applied stress (referred to by the alternating stress, σ_a).

$$\sigma_a = (\sigma_{max} - \sigma_{min})/2 \quad \text{Equation 2.13}$$

The remaining major general factor is the number of cycles at which the component is repeatedly loaded at, N. Other factors have been shown to affect a materials fatigue damage behaviour such as temperature and moisture content [25]. When considering composites, the fibre type and the layup (geometric arrangement) of the plies are other notable factors with have influence over fatigue characteristics [26].

2.3.1 Constant Amplitude

Typically, constant amplitude fatigue tests are performed experimentally as they are relatively quick and enable reasonable estimates to be made about a materials fatigue properties. These tests involve loading a specimen at a repeating stress cycle such that the values of σ_{max} and R are constant for the duration of testing (under load control). An example of which is displayed in Figure 2.6 which depicts a cyclic ($R = -1$) stress cycle with a maximum stress of σ_{max}.

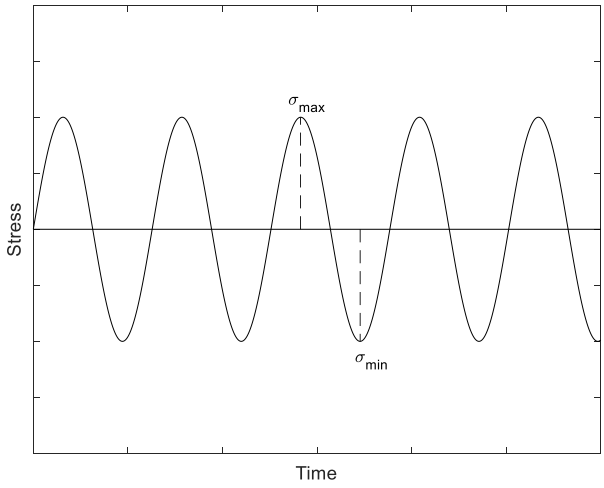

Figure 2-6 Plot of constant amplitude loading sinusoid (cyclic)

From acquired fatigue data consisting of the loading parameters and the number of repeated cycles at which testing was conducted at until failure occurred, models can be utilized to

predict/represent the fatigue life of materials. The fatigue life is the number of cycles of oscillating stress required to induce failure for a given set of loading parameters (σ_{max} and R).

Stress-Life Curves (S-N)

Stress life curves (S-N) relate the maximum load stress and the amplitude ratio to the fatigue life. Commonly the number of cycles until failure occurs is plotted against the maximum stress with individual curves being generated for each amplitude ratio. In the case of some metallic materials the S-N curve plateaus and becomes horizontal as the number of cycles is increased (i.e. for $N > x$, $\sigma_{max}(N)$ is constant), this is referred to as the endurance limit. If the material is loaded at σ_{max} such that it is below the endurance limit then theoretically an infinite number of repetitions of the loading cycle can be endured without failure occurring.

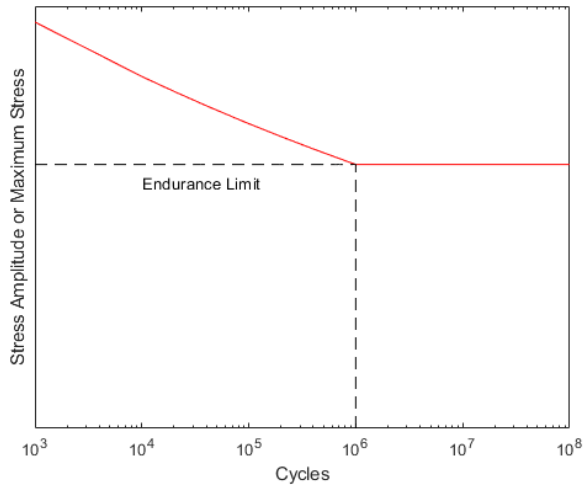

Figure 2-7 S-N curve with indication of endurance limit

However, this is an idealised case as these curves are created from experimental data and as such a cut-off point will exist such that testing doesn't continue indefinitely, this is known as runout. For example 10^6 cycles is considered as a large number of cycles for metals and is typically used

to define the runout, while excess of 10^7 cycles is expected for the life of some wind turbine blades [27]. Furthermore previously mentioned factors which influence a materials performance under fatigue will further reduce the endurance limit. While the idealised curve in Figure 2.7 shows a distinct endurance limit, this isn't the case for many non-ferrous alloys [28]. Similarly, some composites can be considered to possess a endurance limit while others not so, unidirectional composites for example have been observed to have a endurance limit for their matrix, while the fracture strain will be dependent on the fibre stiffness [29]. Mandell demonstrated that for short fibre composites, if the specimens were fibre dominated there was no apparent fatigue limit in tensile fatigue [30]. Further noting that the behaviour of this class of materials was dependant on the fatigue properties of the matrices, component strands and interfaces but that changes to composition showed significant trends [30].

A power law model was formulated by Basquin , requiring both a point on the material curve and a fatigue strength exponent (slope of the material curve) [31], and is commonly written as:

$$N_f = N_e \left(\frac{S}{S_e}\right)^{\frac{1}{b}} \qquad \text{Equation 2.14}$$

Where N_f is the number of cycles to failure, S is the applied stress range ($\sigma_{max} - \sigma_{min}$), N_e & S_e correspond to the single point on the material curve representing the endurance limit and b is the fatigue strength exponent. As mentioned before though, the flat plateau behaviour isn't exhibited by all materials.

Equation 2.14 is a representative for a completely reversed loading, hence for non-zero mean stress cases an equation which details the relationship between the stress amplitude, the mean and alternating stresses is required. Goodman's relationship is well known and incorporates the ultimate tensile strength (σ_u, UTS), it initially saw implementation by J.O. Smith [32, 33].

$$\sigma_{ar} = \frac{\sigma_a}{1-\sigma_m/\sigma_u} \qquad \text{Equation 2.15}$$

However, this model like the Morrow [34] or Smith-Watson-Topper (SWT) [35] models was still based on fitting test data exclusively from completely reversed loading. The Walker equation

conversely enables for the numerical fitting of fatigue data with a variety of mean stress values through a fitting parameter, γ_w [36].

$$\sigma_{ar} = A_w N_f^{b_w} = \sigma_{max}\left(\frac{1-R}{2}\right)^{\gamma_w} \qquad \text{Equation 2.16}$$

Where σ_{ar} can be considered the *equivalent completely reversed stress amplitude* in terms of Equation 2.16 [37]. Dowling et al found the Walker equation (Equation 2.16) to give superior results over the Goodman relationship when studying the mean stress effects on steel and aluminium alloys and a single titanium alloy [37]. Further noting both Morrow and SWT achieved reasonable levels of accuracy but Morrow's limitation of requiring the true fracture strength for fitting aluminium. While the SWT method which corresponded to a $\gamma_w \approx 0.5$ case was unable to demonstrate the discovered trend of decreasing γ_w with increasing strength, hence a sensitivity to the mean stress.

When considering composites, the effects of the mean stress have been found to be significant for a range of materials including chopped strand mat [38], fiberglass [39] and short fibre reinforced polymer composites [40]. The Walker equation has seen use with composites, Zongjin et al found that for $\gamma_w = 0.4$ it showed the best correlation for short glass fibre reinforced polymer composites when compared against Goodman, Gerber, Soderberg and SWT [41].

Constant Life Diagrams

While S-N data can be represented by a plot consisting of N and σ_{max} data, when examining the fatigue life of a material constant life diagrams are commonly utilised as they consist of curves which each have a set estimated fatigue life. The horizontal and vertical axis are the mean stress and alternating stress/stress amplitude respectively. Lines with constant R values initiate from the origin (zero mean and alternating stress) and continue with a constant gradient, the fully reversed cyclic case ($R = -1$) for example is a vertical line which coincides with the vertical axis. Figure

2.8 illustrates several constant life curves with estimated fatigue lives of 10, 1000, 10 000 and 1 000 000, the *R* ratio lines demonstrate the positions on these curves at which data points from S-N curves are added.

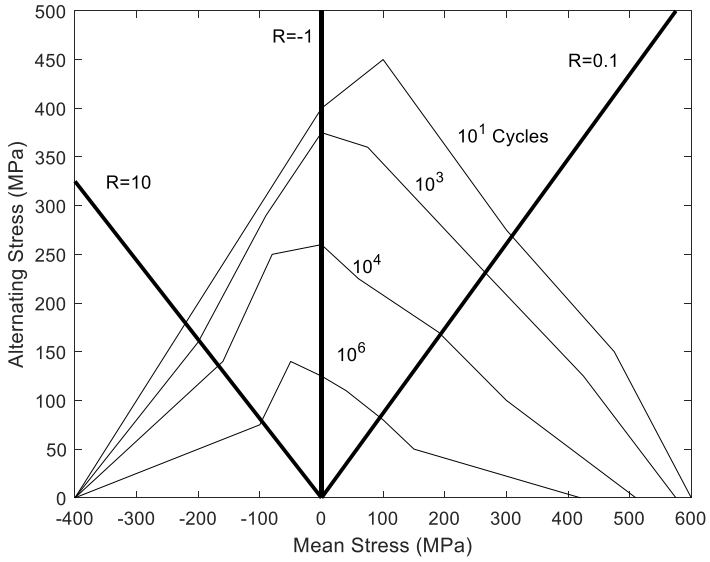

Figure 2-8 Goodman diagram with four constant life curves

Each constant life curve can be thought of as a projection of the constant amplitude fatigue data across several *R* values at one specific life value [42]. As each individual S-N curve represents loading at a constant *R* value, each curve only contributes a single data point to each constant life curve.

As the failure mode which the constant life diagram portrays isn't restricted by design, simple modes such as tensile loading and more complicated loadings such as three point bending can both be represented. Symmetry about the alternating stress axis again depends on the failure mode being examined. For the case of tensile testing, in metals if the static strength is equal in both tension and compression then symmetry is expected, while in composites symmetry isn't typical as these two strengths are likely not equal due to the different failure mechanisms associated with tension and compression [42].

Several types of constant life diagram exist, including a linear Goodman diagram, a shifted Goodman diagram and a constant life diagram based on multiple R values. The linear Goodman diagram is simple and as a result most well-known, using Equation 2.15 the equivalent alternating stress is calculated from fully reversed cyclic loading conditions. Hence besides conducting experimental testing at $R = -1$ only the UTS is required to construct the constant life curves.

A shifted version of the Goodman diagram was implemented to address the asymmetry in experimental results while still continuing to be simple, which translated the linear Goodman diagram in the direction of the positive mean stress and has a maximum stress amplitude equal to the average of the magnitudes of the UTS and ultimate compressive strength (UCS).

Both the linear and shifted Goodman diagrams are comprised of solely $R = -1$ S-N data and static data. However, if experimental data is available for a variety of amplitude ratios then it can be amalgamated into the constant life diagrams. As a result the model cannot be based on Equation 2.15 and loses the simplicity of the linear model. Experimental data points are projected onto the mean stress – alternating stress plane at each tested R value, while untested ratios are interpolated (conventionally by a straight line between points of equal life). A parabolic model using this multiple R value approach was proposed by Harris et al in order to produce a constant life diagram for carbon fibre composites [43].

While a useful representation of S-N data, constant life diagrams do have notable disadvantages. The projected data points from the S-N curves are essentially mean values of the fatigue life, hence the statistical information (scatter) relating to each S-N curve and the goodness of each fit is lost upon construction of the diagram. This can be remedied by plotting additional lines corresponding to a standard deviation or percentile bound the fatigue life, tolerance bounds have been implemented by [44] for a fibreglass composite using experimental data consisting of 13 R values. Secondly, while the constant life diagram depicts fatigue life, the diagram includes regions which represent static failure as well as creep. The horizontal line representing $R = 1$ ceases at the static failure points (UTS and UCS), as this is a constant creep load the assumption that all

constant life curves will converge to these points is the result of limited data. Mandell et al developed a detailed constant life diagram to improve spectrum loading predictions, the diagram didn't show convergence to the UTS as constant load tension tests were conducted at a constant 10 cycles per second, the time to failure was then related to the number of cycles to failure, thereby including creep failure data [45].

2.3.2 Variable Amplitude

Constant amplitude fatigue testing is typically relatively simple to conduct, however it isn't representative of the loading which is experienced by aircrafts. Conversely, variable amplitude loading more accurately characterizes the realistic loading experienced by varying both the alternating stress and the maximum stress (not necessarily both at once). Loading spectra collected from in service aircrafts can be used to conduct experimental tests at a significantly faster rate than what the aircraft experienced in the field (such as Figure 2.9). These spectra will be unique to the aircraft they were obtained from and as such the loading conditions which the tested material experiences will also be unique to that aircraft.

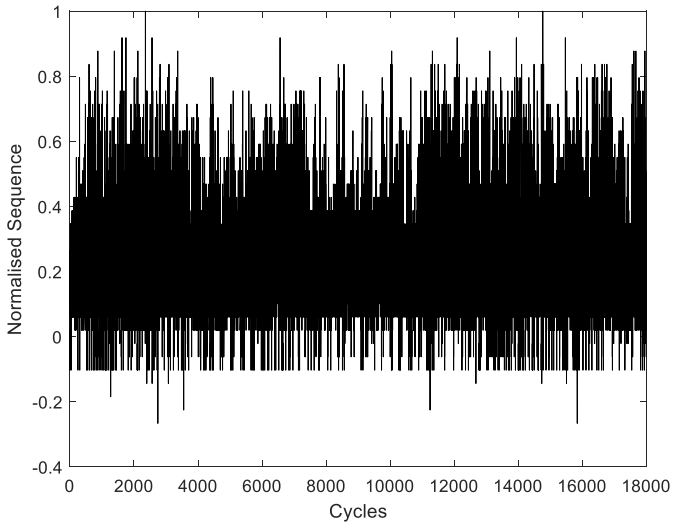

Figure 2-9 Variable amplitude loading sequence (FALSTAFF)

Block Loading

Due to the added complexity of testing full variable amplitude fatigue spectra, sections of a spectrum are sometimes converted to equivalent blocks of constant amplitude loading. The resultant loading histories which are created are referred to as block loading sequences. Block loading overcomes limitations associated with variable amplitude testing, such as the inability for fatigue testing machines to reach the specified limits at elevated speeds. Due to high level of variation in the load sequences, servo-hydraulic fatigue machines will tend to overshoot and undershoot the desired levels hence the frequency at which testing is conducted at will be correspondingly decreased thereby increasing the test time. Over/undershoots can be reduced through tuning of the servo-hydraulic machine with appropriate compensators. Also, by implementing a block loading scheme, the variation in loading conditions will be drastically decreased allowing for higher frequency testing due to a reduction/omission of under/over shooting.

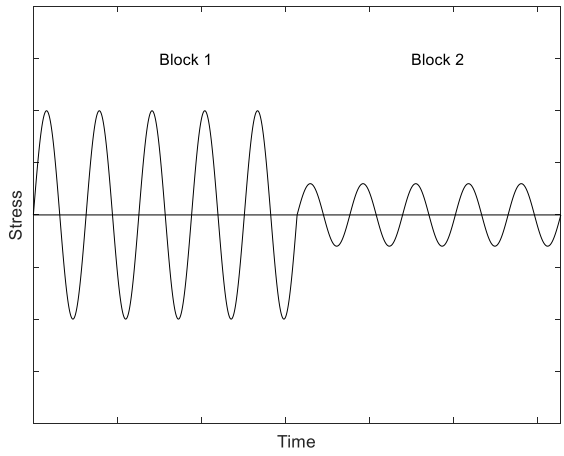

Figure 2-10 Block loading sequence

A block loading spectrum is displayed in Figure 2.10, when compared to the variable amplitude spectrum in Figure 2.9 the relative simplicity of the block method is illustrated.

Determination of equivalent constant amplitude blocks is commonly performed through the Palmgren-Miner rule (Miner's sum) which is a linear damage model which summates the damage contribution of each cycle within a sequence as a fraction of the number of occurrence over the expected fatigue life under constant amplitude testing at the given loading condition [46].

$$D = \sum_{i}^{k} \left(\frac{n_i}{N_i}\right) \qquad \text{Equation 2.17}$$

Where D is the total damage contributed by all cycles within a given sequence (fatigue damage), n_i is the number of times that unique cycle i occurs within the sequence, and N_i is the fatigue life of the specimen under constant loading i.

The Miner's sum was originally proposed for applications with metallic materials and has seen widespread use including in the construction of block loading tests for composite materials [47, 48]. However, this linear damage model is also regarded as often being non-conservative [49] and in cases overly-conservative, this has led to the development of numerous cumulative damage models with a range of applications and limitations. Van Paepegem and Degrieck [50] developed and applied a fatigue damage model which simulated the three stages of stiffness degradation (limited to delamination free $R = 0$ cases) for fiber-reinforced polymer composites using block loading. Their aim was to determine whether high-low or low-high amplitude loading was more damaging as literature is currently divided on the matter, their findings indicated that the number of transitions from a low-high and high-low as well as the present damage of the specimen determined whether one transition was more damaging then the other [50]. Adam et al. found the Miner sum to be sufficient for analysis of T800/5245 carbon fibre composites in tension-tension blocks, but for compression-compression and mixed cases it drastically over predicted the fatigue life [49]. Adam proceeded to represent fractional damage by means of a power law with predictions falling within 2% on a log(cycles) basis. Block loading has seen particular use in studying the presence and behaviour of sequence effects [50-52].

Specific damage models will be further discussed in Section 2.3.3.

Flight Spectra

When developing an aircraft, fatigue testing using complete flight spectra enables not only the service life to be determined but also can be useful for identification of critical details which were previously unidentified [53]. The flight loading spectrum is designed from data acquired under flight conditions when a variety of manoeuvers are performed, as well as taxiing, climbing, cruising, descent, flight times and other conditions of the vehicle mission profile [54]. The spectrum should also accurately reflect the amount of time the aircraft is experiencing each loading regime. The combination of the vehicles loads and the frequencies results in a load profile which is referred to as the design loads spectrum [54]. Stress spectra are commonly developed for each critical stress area through the translation of the aircraft load to coupons, element, and subcomponent stress, this is shown in Figure 2.11.

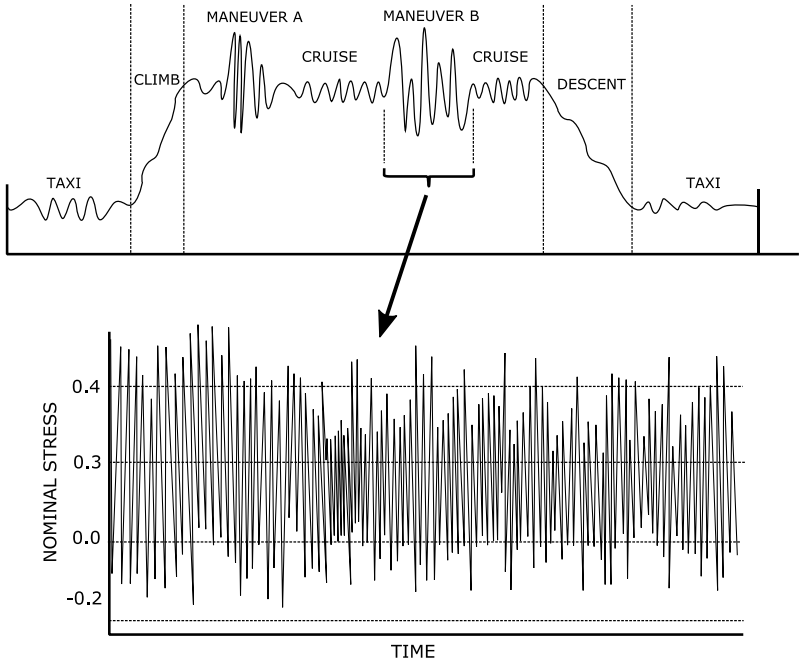

Figure 2-11 Mission profile broken up into the component stress spectrum [54]

When designing fatigue spectra for modern fixed wing aircrafts it is not unusual for hundreds of thousands of cycles to be present to characterise the vehicle over its entire design life. Due to the size of these spectra and the significant test times required to conduct full scale tests, accelerated testing and modelling is often used as an alternative [55]. The process of truncating these design loading spectra depends on the type of aircraft and its design service usage. Metallic structures for example can have high amplitude loads clipped as they induce plastic zones at the crack tip which causes crack growth retardation (a slowing of crack growth). When considering composites due to their high sensitivity to such loads, to avoid producing a non-conservative spectra clipping isn't used without development tests [54]. The methods implemented to reduce the size of the spectrum are heavily dependent on the materials to which the spectrum concerns (including hybrid designs), though for safe-life design a conservative spectrum is sought.

2.3.3 Damage Modelling

In order to reduce a fatigue spectrum in a conservative manner (conserve the damage attributed to the original sequence), it is necessary to have a means for quantifying the damage each individual cycle deals for both a relative and absolute comparison. Damage models are tools for predictions regarding initiation, propagation and fracture of a material, as such depending on the material being examined the models which are applicable can change. Particularly when considering composite materials, characteristics such as the reinforcing agent leads to drastically different models making a highly accurate general damage model not practical. Commonly implemented damage models for both metals and composites will be examined along with more specific models which address particular fracture mechanisms.

Miner Summation (Variations)

The Miner's summation is the earliest model which still sees wide usage for damage attribution in variable amplitude sequences [46, 56-58]. Represented by Equation 2.17, the linear damage accumulation rule predicts failure once $D = 1$ and only requires data from an S-N curve for a given R ratio (multiple R values for improved accuracy). Due to its simplicity, Miner's sum has several shortcomings that are well known, most notable is it being load order independent (same damage sum regardless of cycle order) and inaccurate for block loading cases for not only composites but homogenous materials as well [59]. The inaccurate predictions are commonly non-conservative, at times by orders of magnitude [60].

Various alterations have been made to Miner's sum to improve the predictive accuracy for composite materials. Owen and Howe [61] adjusted the linear model based on crack development in glass reinforced polymer composites introducing two fitting parameters and a constant power term:

$$D = \sum_i \left[A\left(\frac{n_i}{N_i}\right) + B\left(\frac{n_i}{N_i}\right)^2 \right] \qquad \text{Equation 2.18}$$

They highlighted the importance of the stress ratio, determining that an increase in stress ratio led to a decrease in the fatigue strength of the composite. The model was further generalised by Bond and Farrow who parameterised the power term in Equation 2.18 for their work with quasi-isotropic graphite composite plates with metallic fasteners. These parameters were determined from tensile and compression testing under the FALSTAFF loadings, with stiffness properties and initial strength values being incorporated into the parameters [62]. For matrix dominated angle ply laminates the model performed well, though for fibre dominated quasi-isotropic laminates it was overly conservative. Further highlighting how the added complexities in composite damage mechanisms restrict the applicability of devised damage accumulation models.

Residual Strength models

Residual strength models assume that the residual strength is a monotonically decreasing function of the applied load (cycles), while incorporating the initial and end conditions [63]. The initial residual strength is equal to the static/virgin strength:

$$\sigma_r(0) = \sigma_0 \qquad \text{Equation 2.19}$$

Under constant amplitude fatigue at fatigue failure ($n = N$) the residual strength is equal to the applied load:

$$\sigma_r(N) = \sigma_{max} \qquad \text{Equation 2.20}$$

When compared to the damage accumulation models, under variable amplitude loading residual strength models have the benefit of having failure criteria described by both the residual strength and the applied maximum stress. Meaning that the life predictions are reliant on both the current load and the current damage the specimen has undergone [63].

$$\sigma_r(n) \leq \sigma_{max}(n) \rightarrow Failure \qquad \text{Equation 2.21}$$

By determining the damage from the specimen's strength, the models can be experimentally verified throughout the fatigue life of the specimens through intermediary measurements.

Numerous models have been devised with the intent on representing either the residual strength or the fatigue life distribution. Derivations of these models will tend to involve integration of a residual strength rate equation to produce a statistical distribution of both the virgin strength and fatigue life. As such the assumption that the probability rank of the virgin strength and the rank of the fatigue life have a one-one relationship is characteristic of probability models [63].

$$F_{\sigma_0}(\sigma_k) = F_N(n_k) \qquad \text{Equation 2.22}$$

Chou and Croman [64] first coined the term strength life equal rank assumption (SLERA) to describe this relation. Where in Equation 2.19, both F_{σ_0} and F_N are cumulative distributions of

the initial strength and life respectively and the k denotes the kth percentile specimen with its corresponding strength and life. SLERA is unable to be proven strictly with experimental testing due to the in-ability to measure any one specimen's initial strength and fatigue life, as both tests are destructive in nature.

Post [65] detailed an in-depth review of established residual strength models, providing reasoning behind each model and the associated benefit/shortcomings.

It was noted by Sarkani et al [66] that several proposed residual strength models could all be expressed as a solution to the following rate equation:

$$\frac{d\sigma_r(n)}{dn} = -B\frac{Cn^{C-1}}{A\sigma_r(n)^{A-1}} \qquad \text{Equation 2.23}$$

Where A,B and C are parameters based on the material which can be a function of R and σ_{max}. By taking into account the failure condition (Equation 2.21) and the initial condition (Equation 2.19) results in:

$$\sigma_r(n,\sigma_{max})^A = \sigma_{0i}^A - \left(\sigma_0^A - \sigma_{max}^A\right)\left(\frac{n}{N}\right)^C \qquad \text{Equation 2.24}$$

Where σ_{0i} is the residual strength of the specimen before being loaded at σ_{max}. Further accounting for the failure condition enables the damage due to n cycles to be defined as:

$$D(n,S) = \frac{\sigma_0 - \sigma_r(n,S)}{\sigma_0 - \sigma_{max}} \qquad \text{Equation 2.25}$$

By using Equation 2.25, under a random variable amplitude loading the fatigue life of the specimen can be calculated through an iterative process.

Residual strength models were first considered for composite materials by Broutman and Sahu [67], who put forth a linear model to depict the decrease in residual strength (which corresponds to Equation 2.21 for A=C=1) for cross-plied E glass fiber/epoxy laminates.

$$\sigma_r = \sigma_{0,i-1} - \sum_i(\sigma_0 - \sigma_{max,i})\frac{n_i}{N_i} \qquad \text{Equation 2.26}$$

Where i is used to reference which load cycle is being referred to (i.e. $i-1$ refers to the previous loading cycle, while i is the current one). Equation 2.23 was found to produce more accurate predictions of the fatigue life under a two block loading case than Miner's sum, while requiring the same amount of information as the Miner's sum as no additional parameters were implemented.

A particular form of Equation 2.24 (for C=1) has been utilised by Hahn and Kim [68], who incorporated a damage parameter dependent on the applied stress, the fatigue life and A. Hahn and Kim detailed the form of the damage parameter such that Equation 2.27 is equivalent to their devised relation, which they utilised when proof testing unidirectional glass/epoxy composites.

$$\sigma_r^A = \sigma_0^A - (\sigma_0^A - \sigma_{max}^A)(\frac{n}{N}) \qquad \text{Equation 2.27}$$

They further noted that a Weibull distribution could represent the static strength distribution and the life distribution, though the level of significance was low so a recommendation was made to study the relationship between static strength and fatigue life from a probabilistic view.

Reifsnider and Jamison identified three regions of damage development experienced by composite materials during fatigue [69]: rapid degradation due to matrix cracking, followed by a slow linear decline due to delamination and fibre failure, and a sharp decline in properties near the end of the specimen's life. With the exception of Equation 2.24, the models previously discussed are capable of only modelling either the first or last two stages. Consequently, models have been constructed to achieve representation of the three regions, Yao and Himmel [70] conceived Equation 2.28 and applied it to a two block variable amplitude loading case.

$$\sigma_r(n) = \sigma_0 - (\sigma_0 - \sigma_{max})\frac{\sin\left(A\frac{n}{N}\right)\cos(B-A)}{\sin(B)\cos\left(B\frac{n}{N}-A\right)} \qquad \text{Equation 2.28}$$

Probabilistic approaches to residual strength models have seen exploration since Yang and Liu [71] constructed Equation 2.26 from the integration of the generalised rate equation along with applying boundary conditions and holding frequency constant:

$$\sigma_r(n)^C = \sigma_r(0)^C - f(\sigma_{max})n \qquad \text{Equation 2.29}$$

Where f is a general function of the applied stress, frequency and stress ratio (frequency is held constant in Equation 2.29). Yang and Liu made the assumption that the initial strength could be represented by a two parameter Weibull distribution with scale and shape parameters β and α respectively.

$$P(X \leq x) = 1 - \exp\left(-\left(\frac{x}{\beta}\right)^{\alpha}\right) \qquad \text{Equation 2.30}$$

This assumption has been consistently made in literature and found to be acceptable when considering the statistical representation of the virgin strength [64, 68, 72-74]. Through substitution of residual strength degradation equations such as Equation 2.29 into Equation 2.30 along with the failure boundary condition of Equation 2.21, a predicted distribution of fatigue life can be formulated.

Recently, D'Amore et al. [75] detailed a modified two parameter wear-out model based on strength degradation verified through the use of three different material data sets. Using this model Califano et al. [76] has highlighted the limitations of the Palmgren-Miner rule in particular its inability to distinguish between the sequence of loading potentially resulting in highly un-conservative damage predictions. Califano et al. has suggested using residual strength life data to predict high to low and low to high sequences. From the experimental data set D'Amore et al utilised, progressing from a high to low sequence was found to be more damaging than progressing from low to high.

The model of strength evolution with cycles detailed by D'Amore is as follows [74, 76] :

$$\frac{\sigma i_n - \sigma_{max}}{\sigma i_{ON} - \sigma_{max}} = \exp\left\{-\left[\frac{\sigma_{max}[1+\alpha(n^{\beta}-1)(1-R)]}{\gamma_i(\sigma i_{ON})}\right]^{\delta}\right\} \qquad \text{Equation 2.31}$$

Where α and β are obtained from fitting static strength and constant amplitude fatigue data to Equation 2.32

$$\sigma_{max} = \sigma_o\left[\alpha\left(N^{\beta} - 1\right)(1 - R) + 1\right]^{-1} \qquad \text{Equation 2.32}$$

A cumulative distribution function is then generated using a two parameter Weibull fit (δ and γ) which is dependent on the number of cycles.

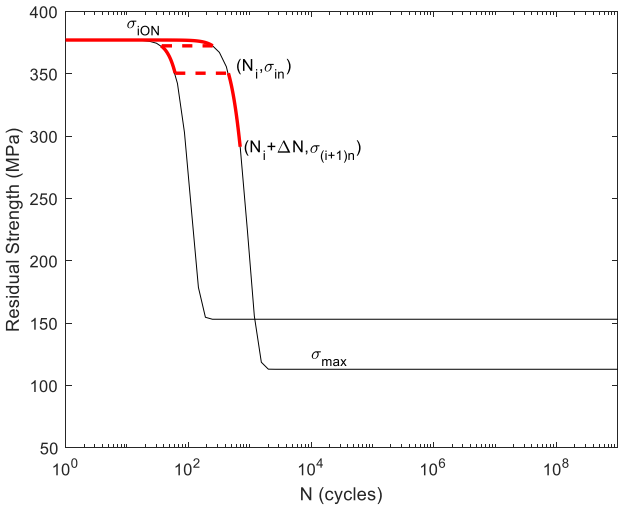

Figure 2-12 Residual strength curves for two loading cycles, where the solid red line traversing from (N_i, σ_{in}) to $(N_i + \Delta N, \sigma_{(i+1)n})$ represents the loading of a specimen under a cycle with loading parameters σ_{max} and R (implemented through the shape and scale of the curve) for ΔN cycles

Figure 2.12 illustrates how Equation 2.31 is implemented with σ_{ioN} being the virgin strength (before fatigue testing), σ_{in} being the residual strength before beginning the ith step of loading for which σ_{max} is the maximum applied stress of said loading cycle.

The damage accumulation rule detailed by Califano [76] is:

$$D = \sum_i \left(\frac{\sigma_{in} - \sigma_{(i+1)n}}{\sigma_o - \sigma_{max_i}} \right)$$ Equation 2.33

This can be observed as the sum of all decreases in the residual strength due to loading with the static strength and the current maximum stress being the upper and lower limits of the residual strength.

Furthermore the failure points which correspond to the maximum loading stress (lower plateaus) are equivalent to points on S-N curves. Hence for block loadings consisting of purely one R value (as shown in Figure 2.13) a single S-N curve will pass through all of the failure points.

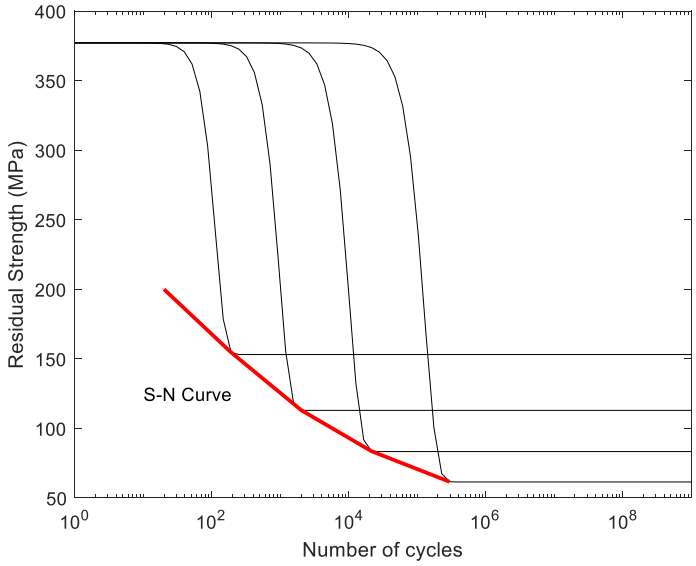

Figure 2-13 Residual strength curves: a family of curves with the same R ratio, hence the failure points lie on the S-N curve for said R ratio.

Sequence Effects

Sequence effects refer to the discrepancy between the fatigue lives of a specimen under a given loading history versus the same type of specimen under the reversed form of said load history [77]. Testing for the presence of this effect has been typically performed through conducting block loading fatigue tests [49, 52, 78, 79]. The transition from high to low amplitude cycles and the

converse are referred to as High-Low (H-L) and Low-High (L-H) sequences respectively. The Miner's sum (Equation 2.17) is commonly used to predict the expected fatigue life under the block loading cases as it treats each cycle within a sequence as independent. Hence experimental testing showing considerable difference between sequences of primarily differing order (i.e. mostly H-L or mostly L-H, but the same Miner's sum) are seen to exhibit sequence effects.

Both through the application of a cumulative damage model and a degrading strength model, the transition from one amplitude block to another is considered to have a damage state which is instantaneous and constant (a horizontal translation). Therefore when traversing either cumulative damage curves or residual strength curves, switching between loading conditions doesn't damage the specimen (as shown in Figure 2.12).

Testing of these block loading sequences has shown H-L sequences to lead to shorter fatigue lives and hence be more damaging than that of L-H sequences for carbon fiber/epoxy cross-ply laminates [78]. While for GFRP-hybrid composites [52] found the opposite trend, further noting that other investigations have found evidence of both cases being more damaging, as well cases of there being no load sequence effects.

Even when restricting the scope of literature to carbon fibre composites there is not a definite rule when regarding sequence effects. Koch et.al. [80] for example found for cross-ply laminates that tension-compression (T-C) and compression-tension (C-T) block loading experiments didn't display significant differences. Similarly Plumtree et.al [81] observed no significant difference when applying two step block sequences to a $[\pm 45]_{2S}$ carbon fibre laminate with both low to high amplitude (L-H) and high to low amplitude (H-L) tests resulting in longer fatigue lives than constant amplitude stress tests under TC cycling. While Gamstedt et.al [78] implemented one sequence comprised of two blocks which was conducted from L-H and H-L under tension-tension (T-T) fatigue, finding H-L sequences to be more damaging for carbon fibre/epoxy cross-ply laminates.

One case of block loading under mode I fatigue was performed by Yao et.al [82] who found loading under L-H blocks resulted in significantly faster crack growth than high to high amplitude (H-H) blocks for unidirectional M30SC/DT120 specimens, stating that fibre bridging can be generated in fatigue delamination of a high stress ratio. To the authors knowledge no block loading test regime has been conducted for mode II delamination with the purpose of investigating load sequence effects despite delamination being a prominent failure mode.

Therefore, the presence and characteristics of sequence effects for different composites and failure modes needs to be investigated due to there being no overarching rule (e.g. H-L is always more damaging than L-H). Furthermore, very little block loading fatigue testing is performed for through thickness loading with most focussing on in-plane loading. This work provides a general and methodical block loading approach to conclusively determine the presence of these effects for two specimen types under mode II delamination.

2.3.4 Crack Propagation Modelling

Metals

Fatigue crack propagation laws are fracture mechanics based models which are utilised to access the fatigue behaviour of structures. In 1963 Paris et al. [83] introduced the stress intensity factor range (ΔK) to be correlated to the crack growth rate, da/dN, suggesting that this range may characterise sub-critical crack growth just as K characterised critical growth. This proposed relation which went onto be referred to as Paris' law, used the stress intensity factor (K) from Irwin's [84] analysis concerning the stress field around a crack tip. The stress intensity factor is defined as:

$$K = Y\sigma\sqrt{\pi a} \qquad \text{Equation 2.34}$$

Where Y is a geometry factor, σ is the applied stress and a is the crack length. Paris et al. depicted the crack growth rate as a function of the stress intensity factor range by plotting the two on a log-log scale demonstrating a linear relation between the two terms, hence it followed that:

$$\log\left(\frac{da}{dN}\right) = m * log(\Delta K) + \log(C_p) \qquad \text{Equation 2.35}$$

By taking the exponential of both sides of Equation 35:

$$\frac{da}{dN} = C_p(\Delta K)^{m_p} \qquad \text{Equation 2.36}$$

Where C_p and m_p are experimentally determined material constants. Equation 2.36 was implemented to represent crack growth of several alloys and as a power law saw much use in characterising crack growth at mid-range growth rates (Region 2 of Figure 2.14).

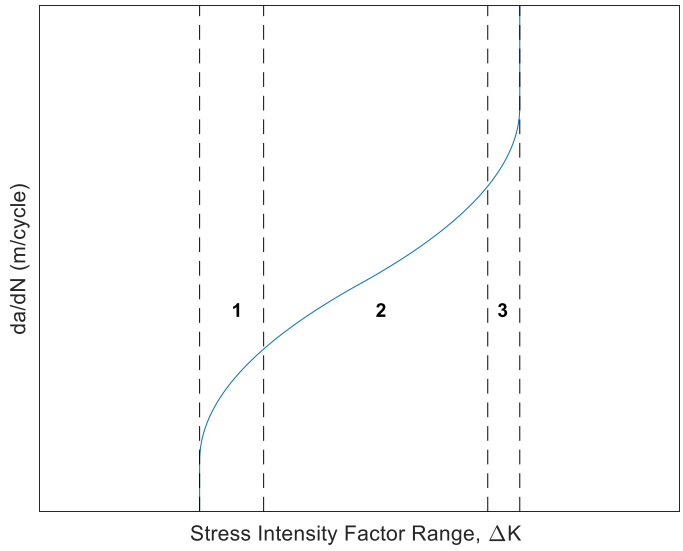

Figure 2-14 Representation of the crack growth rate as a function of the stress intensity factor range with three distinct regions.

The curved behaviour at the lower end of the plot represents the low growth rates where crack propagation is sensitive to variation in the microstructure, environmental factors and the mean stress (Region 1 of Figure 2.14), similar behaviour is displayed at the higher end (Region 3 of Figure 2.14), though crack propagation is influenced less by environmental effects.

While used when regarding metals, the stress intensity factor is commonly replaced with the strain energy release rate when considering crack propagation in composites. The two are related by the following:

$$G = \frac{dU}{da} = \frac{K^2}{E'} \qquad \text{Equation 2.37}$$

Where E' equal the Young's modulus (E) for plane stress, and E' equals $E/(1-\nu^2)$ for plane strain, and U is the strain energy.

Due to the motivations for Paris' law and other crack growth equations being to represent crack propagation in metals, the stress intensity factor rather than the strain energy release rate is present in many equations which sought to improve on Paris' law.

Walker noted that Paris's model didn't account for the stress ratio and to address this limitation, included the effects of the stress ratio through modifying ΔK [36]. The relationship proposed is expressed as

$$\frac{da}{dN} = C_W \left[\frac{\Delta K}{(1-R)^{1-\gamma_W}}\right]^{m_W} \qquad \text{Equation 2.38}$$

Where for the case of $R = 0$, the equation is equivalent to Paris' law, furthermore for $\gamma_W = 1$ the stress ratio is seen to have no effect on the crack growth data. The benefit of the fitting parameter γ_W is that it enables a log-log plot of da/dN against ΔK to collapse onto a single straight line independent of the stress ratio, as such it is determined through an iterative process of testing which value best clusters the experimental data into a line.

Hence the Walker model improves on Paris' model by accounting for the effects of the stress ratio, at the cost of introducing another fitting parameter.

By examining the effects of the environment and load frequency on fatigue crack growth in clad 2024 and 7075 sheet material, Hartman and Schijve [85] presented a model to represent all three regimes of crack propagation through the implementation of a threshold level (ΔK_{th}).

$$\frac{da}{dN} = \frac{C*(\Delta K - \Delta K_{th})^m}{(1-R)K_c - \Delta K} \qquad \text{Equation 2.39}$$

Where K_c is the critical stress intensity factor which is to be determined through static testing. Hartman and Schijve believed that there may be a threshold level of the stress intensity factor in order to induce crack propagation. Their testing indicated that this term would be dependent on both the environment and alloy.

Composites

For composite materials, crack growth models tend to take the form of Equation 36 with ΔK replaced by some function dependant on G. Predictions of crack propagation are conducted by integrating these models to obtain $a(f(G_{max}), N)$, thus enabling for the total number of cycle required to grow a crack a certain length to be determined. It is also common for $f(G_{max})$ to actually take the form $f(G_{max}, R)$.

There is an abundant amount of literature that investigates the manners in which crack growth data under mode II loading can be fit to variations of Paris' law using different forms of the SERR such as; G_{max} [86, 87], ΔG[88-90], $\Delta\sqrt{G}$ and G_{eq} [91-94].

To maintain consistency with Equation 2.37, the equivalent term to ΔK for composite materials wouldn't be ΔG, but rather:

$$\Delta G_q = \frac{(\Delta K)^2}{E'} = \left(\sqrt{G_{max}} - \sqrt{G_{min}}\right)^2 = G_{max}(1-R)^2 \qquad \text{Equation 2.40}$$

Hence $\Delta\sqrt{G_q}$ can replace ΔK in Equation 2.36 to produce an analogous model, this form has seen recent use [95-97].

Jones et al. [96] proposed a model based on a variant of the Hartman-Schijve equation in order to access the 'retardation free' upper bound fatigue crack growth curve for polymer matrix fibre composites. As previously noted the equivalent form of the SERR to ΔK is $\Delta\sqrt{G}$, hence the model is of the form

$$\frac{da}{dN} = D\left[\frac{\Delta\sqrt{G}-\Delta\sqrt{G_{thr}}}{\sqrt{[1-\sqrt{G_{max}}/\sqrt{A}]}}\right]^n \quad \text{Equation 2.41}$$

Where $\Delta\sqrt{G_{thr}}$ is that value of $\Delta\sqrt{G}$ at threshold, meaning that below said value no significant fatigue crack growth occurs. A is a constant which is observed to be analogous to the initial critical value of the fracture energy (G_c).

This model not only provides a means for calculating the worst case crack growth but like the Hartman-Schijve equation, enables for experimental data to be fit such that n is not relatively large. Typically the power term in crack growth models for metals varies from 2-4, while for polymer composites it is generally higher between 10 and 15 [94]. Jones et al. provide a comparison of the fitting parameters when modelling using G_{max} as well as the argument of the brackets in Equation 2.41, finding n values of ~ 9-13 under G_{max} while achieving values of 2-3 for the proposed model. Having a low value of n is important for predicting crack growth as the higher the value of n the more small errors are magnified leading to excessively non-conservative predictions.

Very rarely though are these fitted curves (produced by the modelling discussed) utilised for life predictions, nor is effort directed towards investigating the effect of load history when establishing these curves. Anilchandra et. al. [94] did proceed to predict the failure of IMA/M21 carbon fibre composites that were loaded under a mini FALSTAFF spectrum using a reversible three point bending fixture for mode II delamination, but didn't investigate the influence of load history.

2.3.5 Displacement Controlled Fatigue Testing

Displacement controlled fatigue testing involves loading a specimen through regulation of the achieved displacement levels. For constant amplitude fatigue testing this would mean that the maximum and minimum displacement values will be constant throughout the test. However, the

force (or load) maximum and minimum will change as the crack propagates (resulting in a decrease in material strength, hence requiring less force to reach the same displacement level), unlike with load control which has varying displacement limits throughout constant amplitude testing.

Fatigue loading is typically applied in load control or displacement control, these often closely represent real load conditions. However, literature scarcely examines fatigue under displacement control for mode II delamination and to the authors knowledge there are no established damage prediction models using experimental data for composites fatigued under displacement control. Due to the stability of conducting tests under displacement control and the limitations of the utilised test machines ability to perform at relatively low loads, this research was conducted under displacement control. As a result adjustments to any damage model intended for implementation became a necessity to ensure that the differences in the control choices were represented.

2.4 Fatigue Spectrum Compression/ Reduction Techniques

Modern aircrafts experience hundreds of thousands of loading cycles over the course of their design lives. Meaning that these design load spectrums will require truncation to lessen the extensive test times. To achieve conservative reductions it is necessary to omit stress cycles which fall below the fatigue threshold and don't contribute to damage growth. The methods for doing so vary for metallic and composite materials. This section will detail several methods provided by literature.

2.4.1 Metals

Truncation

Truncation or elimination of cycles in a fatigue spectra is performed by omitting cycles which have minimal impact to the durability of the tested specimens. While truncation does provide the benefit of reducing the length of the test sequence and therefore reducing the time taken to perform a test, the trade-off is that the damage of each pass of the spectrum is decreased. Ideally the removal process will condense the spectrum down to a small fraction of its original size while only minutely changing the damage dealt by the spectrum.

A variety of different criteria are used to remove low damage cycles including; the construction of a stress sequence proceeded by removal of the lowest load level followed by sequence reconstruction, gating/filtering which maintains sequence effects by removal centred on; stress, strain or load range [98]. Specific gating methods can implement indexed rainflow cycle counting to improve the accuracy of the damage attribution with peak/valley pairs. Again, these techniques are restricted by the amount of damage loss that is tolerated, as damage is lost in all cases.

The process of truncation is guided by the knowledge of the damage each cycle within a sequence contributes. Meaning that while cycles can simply be ranked by damage and then removed based on contribution, cycles can also be omitted based on their size (peak-peak) and the intentionally deleted damage can be reintroduced into the sequence by scaling the load.

It is common for turning points to be removed by the selection of an omission level usually a percentage of the endurance limit [99], maximum load [100] or the load level range [101, 102]. Meaning truncation can be performed without any knowledge of the materials damage mechanisms (however this should be avoided), though in the case of the endurance limit, stress-life data curves are required.

Bao and Zhang [101, 102] found good agreement between observations and predictions after truncating at load ranges levels of 9.82%, 11.72% and 13.98% for AA 2324-T39 and AA 7050-T7451 middle-crack tension specimens, which corresponds to an elimination of 26.56%, 46.87% and 62.95% cycles. However, under spectra with truncation load range levels of 17.11% and 21.36% the measured crack growth lives significantly exceeded predictions based on the

Willenborg model. These differences were attributed to crack meandering and branching which notably slows the lead crack growth rate, with Bao and Zhang [101] noting that this branching appears when small cycles are eliminated to higher levels.

Wallbrink and Krieg [98] implemented said small cycle omission and scaling procedure along with a low damage omission method. Predicting that a 90% spectrum reduction through truncation would require at least a 58% damage forfeiture, however through damage restoration using the appropriate model this loss was mitigated, enabling test acceleration by a factor of 10. Highlighting that implementation of pure truncation is restricted, but through the introduction of damage models this limit can be circumvented.

Clipping

The action of clipping doesn't remove any cycles from a load sequence but instead reduces the magnitude of any cycle higher than the clipping level. In metals, the high amplitude loads are typically clipped to obtain conservative results in full scale testing as they can result in crack closure due to the creation of a plastic zone which can delay crack growth and thereby slow said rates [103]. The choice of clipping peak loads is one made to avoid the beneficial influence of crack retardation, i.e. non-conservative fatigue life predictions. However, the clipping level chosen is controversial as depending on the specimen being tested the overall influence of the clipping level may vary. In the case of thin-gauge damage tolerant materials careful consideration should be taken, conversely for thicknesses exceeding 5mm for materials with higher crack growth rates (and yield strength) this is much less (or not at all) of a concern [104]. This difference is mainly attributed to the fact that higher growth rates imply that retardation after a severe flight will be significantly less, while between flights crack growth is likely to progress well beyond the plastic zone associated with the preceding severe flight [104]. To reduce the effects of crack retardation stress levels two of many guidelines were proposed by R.J.H. Wanhill:

- For long-life crack growth testing, peak loads expected to occur fewer than 10 times in the target life should be clipped
- Tests conducted in the in-service inspectable crack growth regime the peak loads should be clipped to approximately 10 occurrences per estimated inspection interval

Schijve suggested that load cycles that occur less than ten times through-out one thousand flights (or over an aircraft's lifetime) should be clipped as these high loads may not be experienced by all aircrafts due to the low occurrence [105].

Testing has been conducted into the effects peak load clipping has on fatigue crack growth, Kujawski et al. modified a spectrum in several ways including reducing the magnitude of the highest peak loads (95%, 85% and 65% peak loads clipped) [106]. Without clipping, the fatigue life of the positive spectrum was found to be six times that of the same spectrum clipped at 65% of the peak load. While negative loads less than 50% of the peak load reduced the amount of crack growth retardation such that the specimens failed three times faster, indicating that compressive loading was as important in overloading.

Merging

Also known as cycle substitution, cycle merging uses the crack growth analysis performed on an original sequence to construct a new sequence with equivalent damage. A fatigue spectrum is split into peak-valley pairs and then a crack growth model is implemented to switch a segment of peak-valley pairs with a single pair which results in the same crack growth.

Cycle merging requires crack growth data to utilise the selected crack growth model. Unlike the previously mentioned techniques an understanding of the materials fatigue mechanisms is essential to successful implementation as equivalent damage demands accuracy across a range of loading parameters.

This method was put forth by Wallbrink and Krieg [98] who tested the algorithm with the FASTRAN spectrum using edge crack stop drill specimens and found a high correlation between the original sequence and the compressed version. Crack growth rates were noted to be slightly quicker in the nucleation phase of growth, which was ascribed to the larger load cycles, known for accelerating a single cracks nucleation.

2.4.2 Composites

While in the case of metallic structures a significant amount of research is focused on clipping the overloads to prevent non-conservative fatigue life estimations, composite materials perform significantly differently. As the failure mechanisms of composites are dissimilar to that of metals the loading components which cause abnormal behaviour could also be different, further leading to the possibility that any unique design and verification requirement would also differ [107].

Effects of Adjustments to Fighter Jet Spectrum on Fatigue Life

The behaviour of composite laminates under fatigue loading is notably distinct from that of metallic materials. For metals, considerable effort has been spent on investigating clipping the overloads. Such an effect is not present for composites, the largest load cycles are considered to in fact be the most damaging. Inherently this means that the process of clipping is unnecessary when performing fatigue spectra simplification as clipping the highest load in a sequence would notably increase the fatigue life of the specimen being tested [107].

The effects of numerous changes to a fighter attack spectrum on composite fatigue life were investigated by Badaliance et al. [107] in the early 1980's. These changes included: Clipping to 90% test limit stress, addition of 115% and 125% test limit stress overloads (separately), addition of low loads, truncation to 70% test limit stress, clipping of tension loads, increased severity and number of air-air loads. The tested spectrum was derived from the stress history from the upper

wing skin of the F-15, which was chosen as composite structures are susceptible to compression fatigue degradation. Both fibre dominated and matrix dominated layups were selected for testing. Clipping to 90% the test limit stress resulted in an increased fatigue life, which was not desirable for the acceleration of fatigue testing. While the addition of the overloads decreased the fatigue life. Upon truncating to 70% the test limit stress, the fatigue life was found to decrease, this was associated with data discrepancy, the specimen manufacturing and the testing process. Similarly, the clipping of tension loads resulted in a lower fatigue life (more notably for matrix dominated layup), in fact load reversals are the most damaging loading mode so removal of said reversals should increases the fatigue life. Further investigation was noted to be necessary to address these results.

The most significant effects in fatigue resistance were found in spectra which increased the magnitude of frequency of high loads. The spectra variations generated from this investigation [107] limit recommendations for spectra formulation to applications pertaining to loads applied to the upper wing skin of fighter aircrafts.

Effects of Truncation/Elimination

When employing composite materials in structural design an objective is for the design service of the structure to be at least met if not exceeded when comprised of a different material. It is also necessary to ensure that the maintenance burden isn't increased [56].

Despite the added complexities of composite laminates, the relative simplicity of truncation and the lack of material knowledge required for conventional implementation has led to successful sequence reductions. Though as is the case with all fatigue spectrum reduction techniques when considering composites, there has been limited published research when compared to metallic materials.

Clark et al. [108] accelerated a FALSTAFF sequence by reducing the number of turning points from 35, 766 to 9,456 through truncation by load level range (8-17 as shown in Figure 2.15) when

fatiguing specimens manufactured from XAS/914C prepreg. Many of the tested coupons contained damage which measured 30mm in diameter. They chose load level range as the select criteria as it enabled the retention of all large compressive and tensile loads, while also removing a large proportion of low compressive loads. The FALSTAFF sequence as displayed in Figure 2.15 is comprised of load levels ranging from 0 to 32, where 32 is the maximum compressive load and 0 is a tensile load, the zero load condition which is indicated by a horizontal line corresponds to level 7.53.

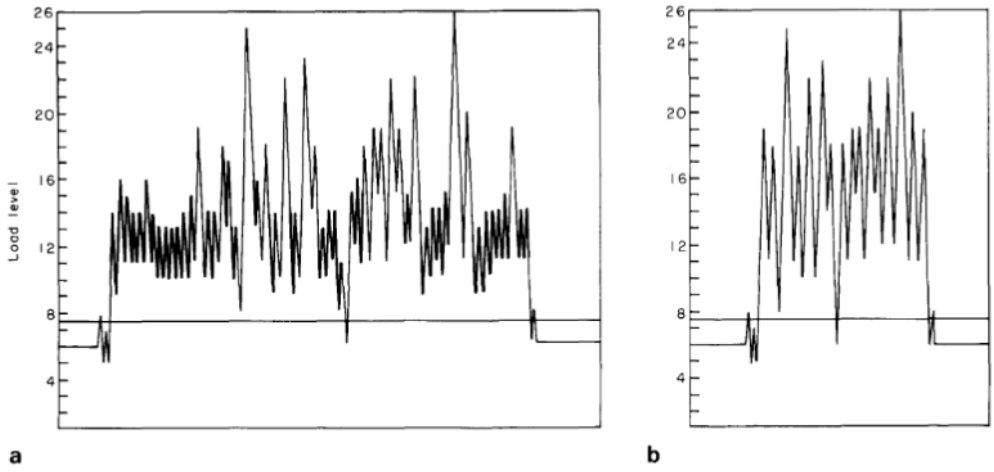

Figure 2-15 (a) Full FALSTAFF load sequence, the zero stress is marked (b) Modified load sequence after truncation [108]

This was found to be an acceptable modification for accelerating fatigue testing as damage growth was seen to be insensitive to the removal of the low load cycles.

Using a baseline spectrum from a vertical tail of a SAAB JAS39 Gripen, Schön et al. [57] performed low cycle elimination to different degrees. Elimination levels of 30% and 50% of the maximum range were found to be acceptable (with sequences named BFKB30 and BFKB50 respectively), enabling 80-90% of load states to be omitted (see Figure 2.16). The fatigue life was noted to be significantly influenced by the removal of high load ranges especially for $R = -1$.

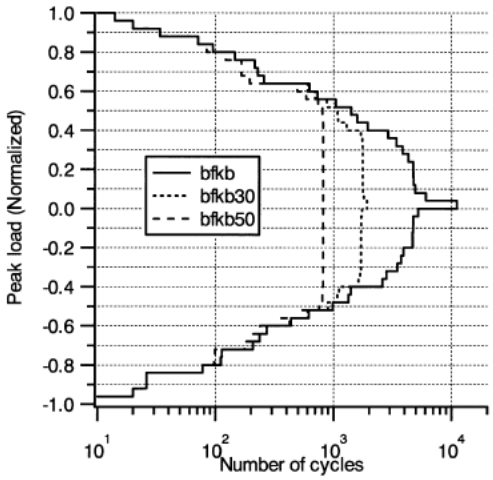

Figure 2-16 Peak load distribution in flight spectrum [57]

Specimens tested under the original spectrum were found to have slightly higher fatigue lives, though the difference was well within the scatter range, meaning that a 50% omission had a negligible effect on durability. Further work by Schön et al. [109] detailed the testing of devised load sequences derived from a flight spectrum, the small amplitude loads in said sequences had ranges of 50%, 30% and 25%. For fatigue spectrums of bolted composite lap joints it was determined that low-amplitude load cycles with a range less than 30% could be eliminated as they don't reduce the fatigue life. While slight reductions to the fatigue life were noted for load cycles with a 50% range, leading to the suggestion that if there are a few load cycles for each large load cycles all cycles with arrange less than 50% may be removable.

While developing a rule for fatigue damage accumulation of longitudinal elements of a composite wing (specifically polymer composite materials (PCMs)) experiencing quasi-random loading, V. Strizhius truncated the TWIST program to different degrees [110]. Load levels from 0.22 to 1.6 times the average stress were omitted, with different combinations of levels being removed forming five truncated iterations of the basic spectrum. The fatigue life estimates and experimental findings at the different truncation levels confirmed that PCMs are more sensitive to the truncation of higher loads than lower ones, and that truncating lower loads enables considerable test time reduction with insignificant changes to the test results. Strizhius noted that

these results agreed with the earlier findings of Edward P. Phillips [111] who performed spectrum truncation while fatiguing notched, graphite/epoxy (T300/5208) laminates.

2.5 Chapter Summary

Over the last few decades carbon and glass fibre reinforced polymer composites have seen an increase in both commercial and defence use. Their prevalence in aircraft structures has increased to the point where by weight, composites comprise the vast majority of the structure. As a result of this increase in popularity, it has become more crucial to have robust methods for testing the failure methods of these composites. Aircraft certification requires that variable amplitude fatigue testing be conducted, this takes a considerable amount of time and money.

Therefore, it would be beneficial to reduce these test times while still maintaining the accuracy and stringency of the currently implemented tests. To do so it is necessary to understand the manner in which damage grows so that equivalent damage growth can be associated with loading cycles in a fatigue spectra, allowing for spectrum reduction.

End of Chapter 2

Chapter 3

Experimental Techniques

3.1 Introduction

The following chapter details the composite specimens tested throughout this research as well as the experimental techniques performed during testing in Chapters 4, 5 and 6.

3.2 Specimens

Layup and Dimensions

Two types of 177.8mm (7 inch) end notch flexure (ENF) specimens were manufactured for the experimental testing performed in this research, one unidirectional and one woven. All specimens were manufactured in accordance with the ASTM standard D 5687/D 5687M [8]. Both types of specimen contained a 76.2mm (3 inch) long and 0.0127mm thick polytetrafluroethylene

(PTFE/Teflon) insert with a straight edge cut located mid-plane of the laminate to initiate crack propagation through the samples.

The unidirectional specimen was comprised of IM7/977-3 carbon fibre prepreg with a 5 Harness Satin arrangement. All specimens were 30 plies thick with uniform thickness at each step with a stacking sequence of $[0]_{30}$. It was cured at ~177 °C (350 °F) for 6 hours after being heated up at a rate between 0.56-2.78 °C (1-5°F) per minute, it was then cooled down at 2.78 °C per minute (max) [112]. The material properties of the IM7/977-3 prepreg are displayed in Table 3.1.

Table 3-1 Material properties for unidirectional IM7/977-3 carbon fibre prepreg [113]

E_{11} (GPa)	E_{22} (GPa)	G_{12} (GPa)	G_{13} (GPa)	ν_{12}	Tensile Strength			Compressive Strength	
					σ_{11} (MPa)	σ_{22} (MPa)	σ_{12} (MPa)	σ_{11} (MPa)	σ_{22} (MPa)
161	8.3	5.3	5.3	0.24	2630	84	82	1680	281

The woven specimen consisted of M18/1/G939 carbon fibre prepreg with a Satin weave with a fibre volume fraction of 57%. All specimens were 16 plies thick with uniform thickness at each step with a cross ply stacking sequence of $[(0/90)/(+45/-45)]_{4S}$. Specimens were ramped at a rate of 2 °C per min and then cured for 2 hours at 120 °C before being ramp again at 2 °C per min and further cured for 2 hours at 180 °C, after which they were cooled at 2 °C per min [114].

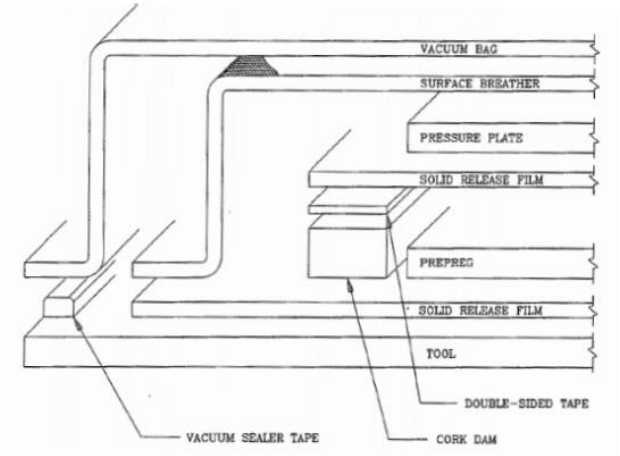

Figure 3-1 Recommended lay-up for CYCOM® 977-3[112]

The material properties of the M18/1/G939 prepreg are displayed in Table 3.2.

Table 3-2 Material properties for HexPly M18/1/G939 carbon fibre prepreg [115]

E_{11} (GPa)	E_{22} (GPa)	G_{12} (GPa)	G_{13} (GPa)	ν_{12}	Tensile Strength			Compressive Strength	
					σ_{11} (MPa)	σ_{22} (MPa)	σ_{12} (MPa)	σ_{11} (MPa)	σ_{22} (MPa)
65	67	4	4	0.04	800	800	100	800	800

Printed Ruler

When performing fatigue tests under Mode II loading, the sliding planes result in a relative movement along the length of the delamination crack which can be seen upon visual inspection. The ability to determine the position of the crack tip is significantly dependent on the degree to which the specimens are being loaded, as small constant amplitude fatigue tests result in minute

relative movement. The contrast between the crack and the remainder of the specimen also significantly influences the accuracy of measuring the crack as it propagates.

To allow for incremental measurements to be taken throughout fatigue tests an inkjet printed label was placed along the length of the specimens. Solid black vertical lines were positioned 0.4mm from each other with every 2mm marking being slightly thicker (i.e. 2, 4, 6, etc) to more easily identify the relative position of the crack tip (Figure 3.2).

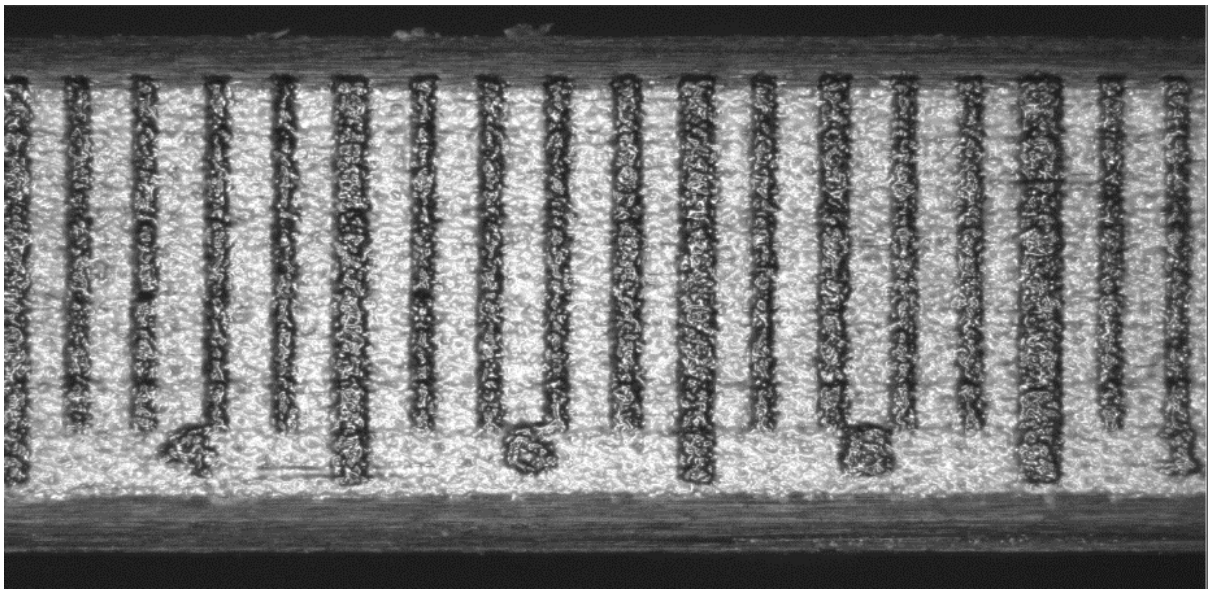

Figure 3-2 Camera image displaying the printed label along the specimen length

A bright background was implemented to provide a stark contrast between the vertical lines and the rest of the specimen, enabling for the sliding motion to be visible at each marking as the crack tip reaches it.

Batch Comparison

Static tests were conducted according to the ASTM D7905 [3] for each specimen batch to check the specimen quality, ensuring that there was consistency between batches.

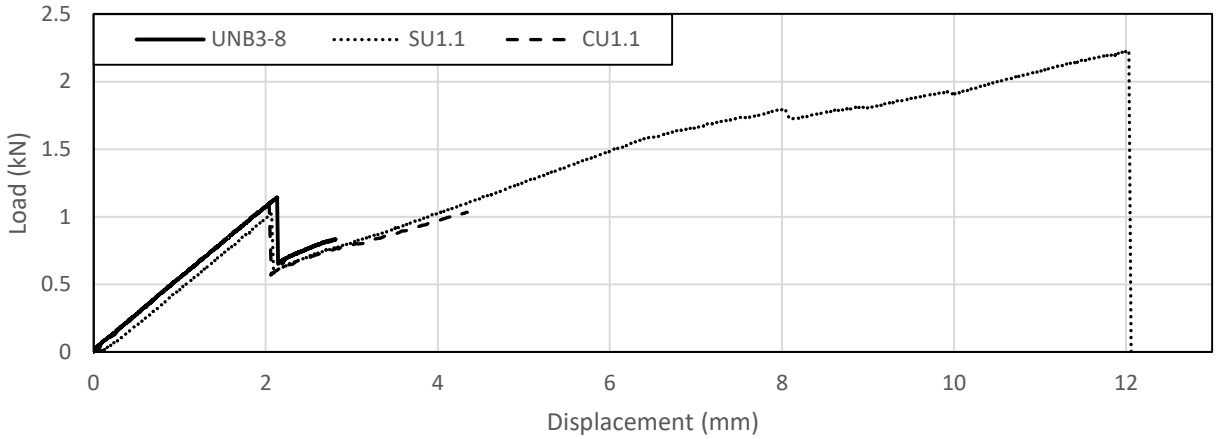

Figure 3-3 Load displacement curves for unidirectional specimens under static loading. Specimens UNB3-8 is from the third batch of manufacturing while SU1.1 and CU1.1 are from the first and second batches respectively

Figure 3.3 shows a high level of consistency between the unidirectional batches with static failure occurring at approximately 2mm displacement, 1kN of loading. A digital calliper was used to measure the dimensions of the specimens from each batch with the mean and standard deviations of each batch provided in Table 3.3 below.

Table 3-3 Statistics of IM7/977-3 specimens measured dimensions

Batch #	Specimen Type	Width Mean (mm)	Width STD (mm)	Thickness Mean (mm)	Thickness STD (mm)
1	Unidirectional	25.5168	0.0988	3.8542	0.0619
	Woven	25.4255	0.0762	3.9550	0.0495
2	Unidirectional	25.5340	0.0438	4.0155	0.1129
	Woven	25.5471	0.0263	4.1838	0.0578
3	Unidirectional	25.5588	0.0389	3.9667	0.0463

The same technician created each batch of both types of specimen and a high level of consistency was observed.

3.3 Static and Fatigue Testing

Test Machine

All static and fatigue testing was conducted using a servo-hydraulic INSTRON 1342 machine with a 100kN load cell (Figure 3.4).

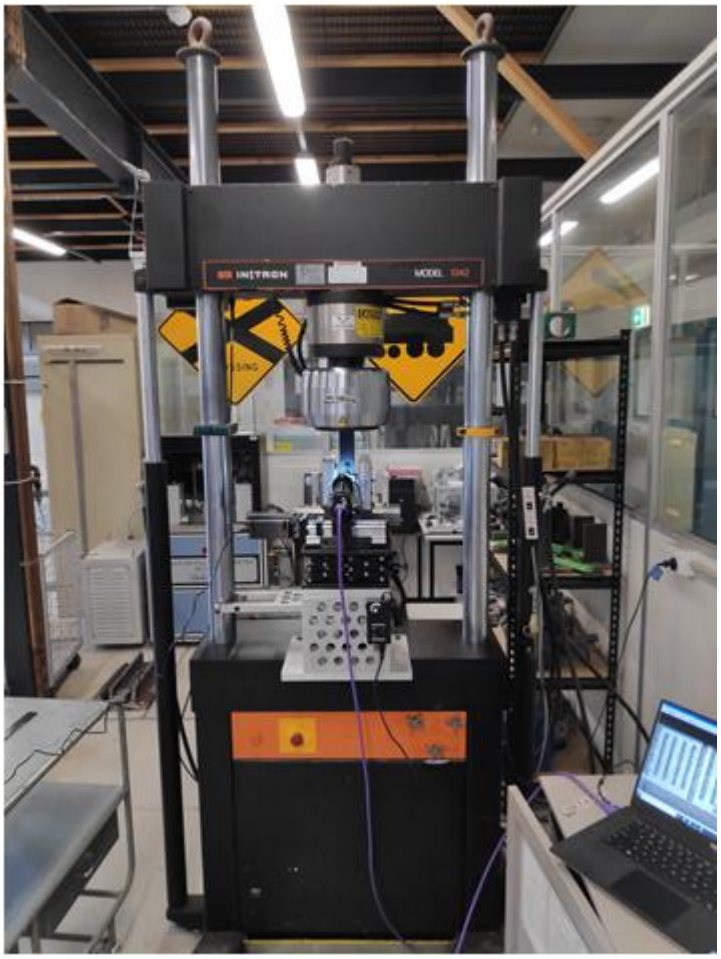

Figure 3-4 100 kN INSTRON machine with the reversible three point bending test fixture and camera setup

The position of the crosshead was manually adjusted before testing by rotating the release valves located on the front panel of the machine. Specimens and test fixtures can be clamped at both the crosshead and actuator, after adjusting the clamp pressure (dependant on the maximum load being applied). As the specimens being tested had static failure loads of ~1kN the clamp pressure was relatively low.

The test machine was connected to a terminal which through a MTS FlexTest 40 Controller and MTS software, controlled the INSTRON actuator. Through the MTS software static and constant amplitude tests were capable of being conducted, with test parameter input via the user interface.

A static test and constant amplitude test were conducted using an Al specimen to verify the machines ability to reach set test limits without overshoot or undershoot (Figure 3.5).

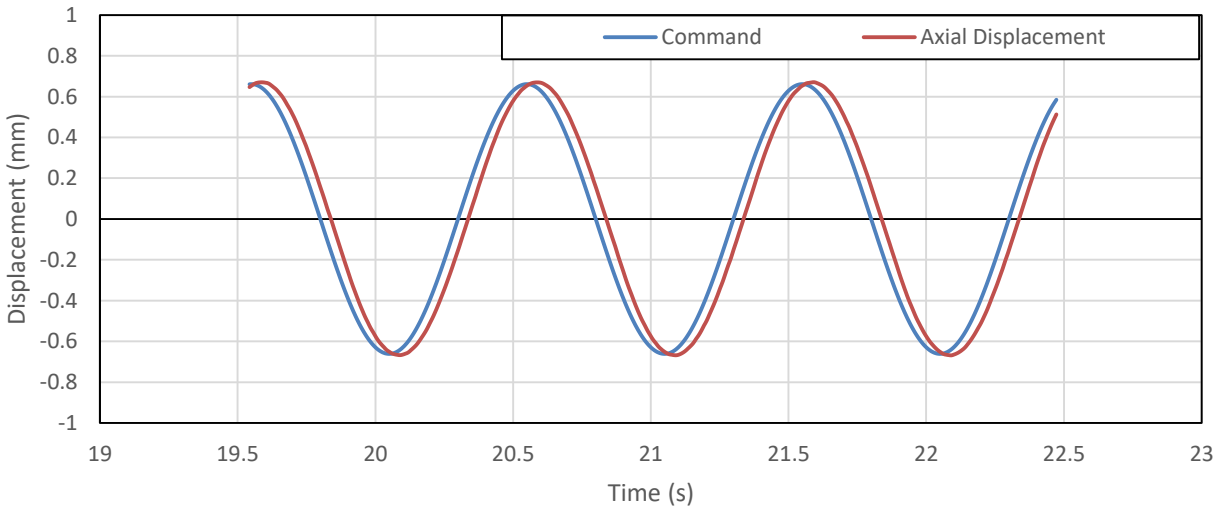

Figure 3-5 Constant amplitude test plots of the input and output signals using MTS software

The machine was capable of reaching the relatively low displacement levels that were required for the fatigue testing of the two composite ENF specimens. The command and feedback curves show that a smooth sinusoidal displacement curve was achieved while reaching the desired limits. For a more complicated loading sequence the MPE software was utilised and again plots were produced of the input and output signals (Figure 3.6).

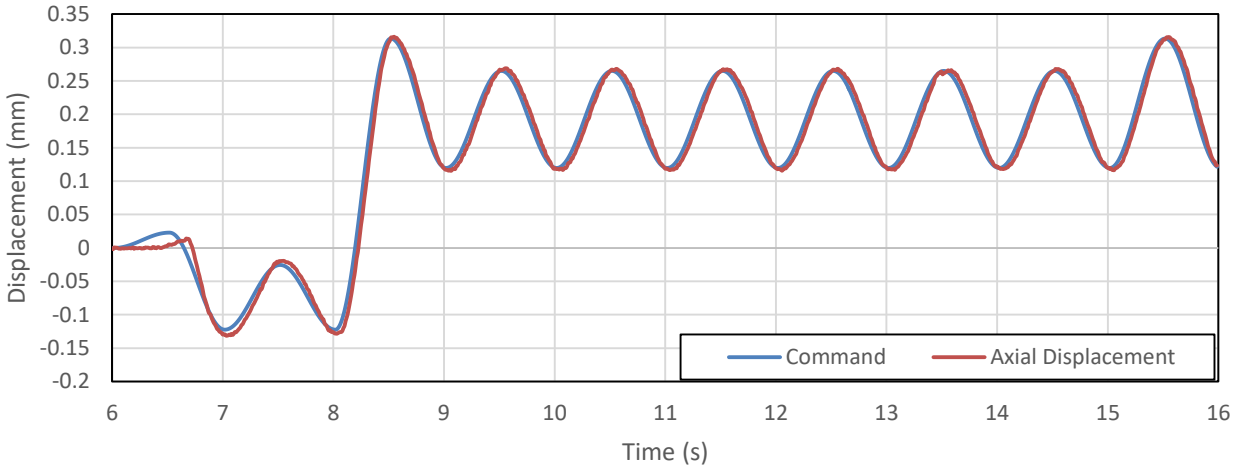

Figure 3-6 Variable amplitude test plots of the input and output signals using MPE software at 1Hz

At the start of testing there are inaccuracy of <5% when reaching the set levels, however this becomes negligible after running the test for a few seconds as the machine reaches the turning points at a testing frequency of 1Hz.

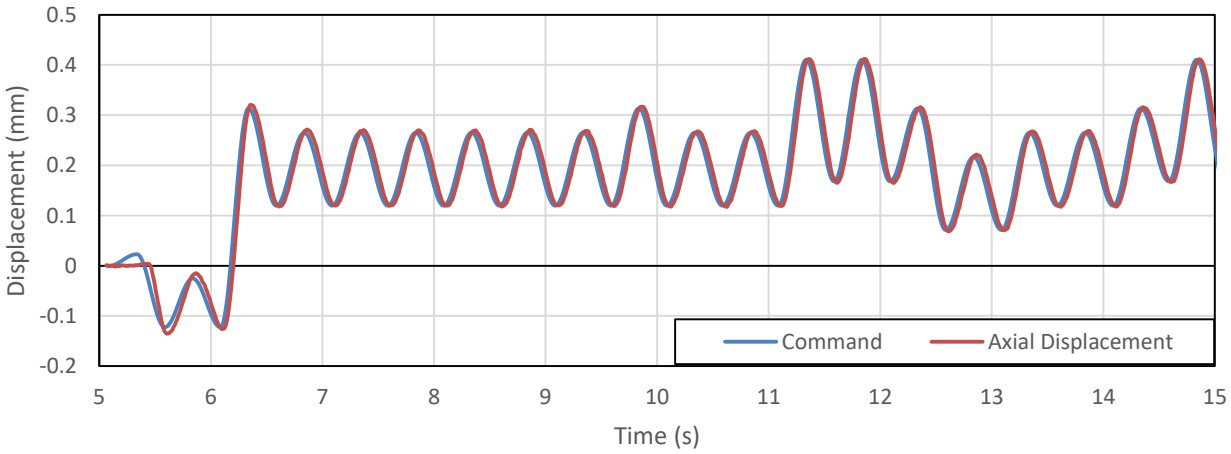

Figure 3-7 Variable amplitude test plots of the input and output signals using MPE software at 2Hz

Similarly for an elevated tested frequency of 2Hz the INSTRON is still capable of reaching the input peak/valley pairs as displayed in Figure 3.7. However, due to visual limitations when measuring, most tests were conducted at 1Hz.

Test fixtures

Initially a conventional three point bend testing fixture was utilised for conducting static testing under the ASTM 7905. Fatigue testing using this setup is limited to positive amplitude ratios (R_d ratios) as specimens can only be loaded in a single direction (C-C) as displayed in Figure 3.8.

Figure 3-8 Three point bend test setup for a unidirectional specimen undergoing static loading

In some cases, only positive or negative R_d-ratio's may be tested for a spectrum, however making such an assumption alters the damage growth behaviour as a result of the changed loading conditions. An alternative may be to mirror cycles/blocks in a spectrum to see whether or not it affects the Mode II test specimens.

Thus a reversible three point bend test fixture was designed and fabricated (Figure 3.9) so comparisons can be made to a conventional three point bend test fixture [77]. The end supports in the reversible rig are pivoting components to allow the specimen to bend freely without inducing undesired stress concentrations. Teflon strips were placed on the contact surfaces of all loading and support rollers to ensure that friction was minimised between the specimens and the fixture, permitting a smooth sinusoidal loading curve. Conventional three point bend tests conducted show a great degree of similarity between the two setups [88, 116, 117].

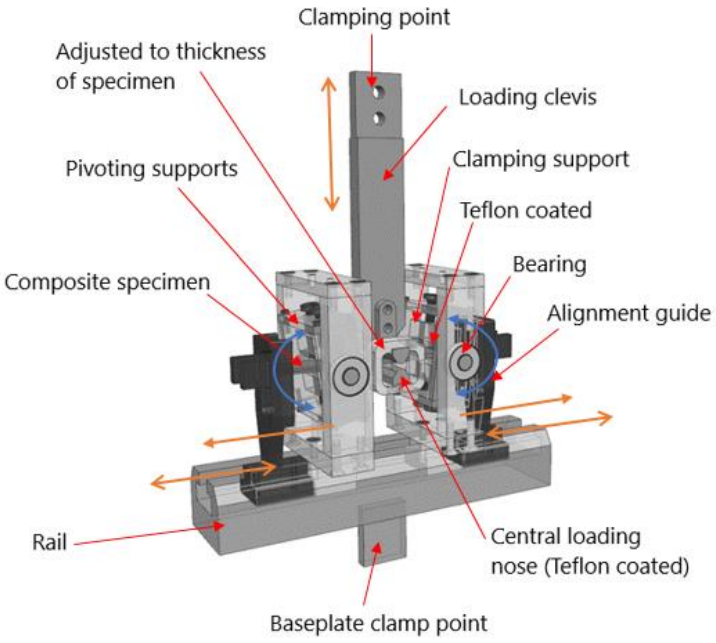

Figure 3-9 Custom reversible three point bend test fixture for Mode II testing

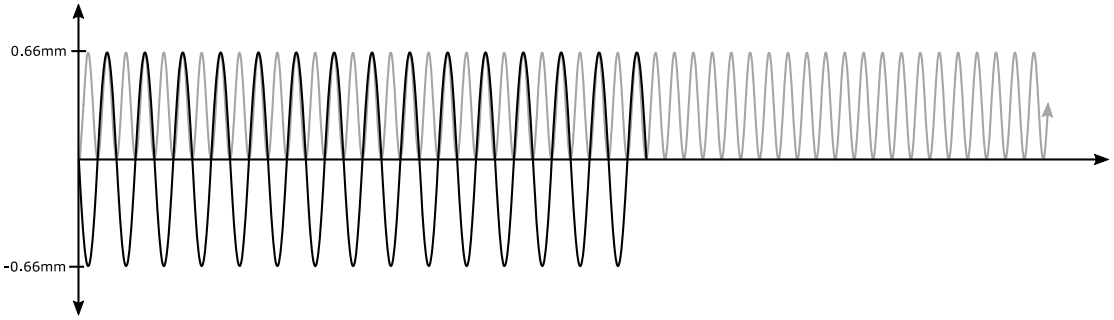

Figure 3-10 Mirrored (grey line) and fully reversed (black line) constant amplitude spectra; amplitude of 0.66mm; composite IM7-977-3 specimen tested

Table 3-4 Reversible three point bend test and mirrored three point bend test comparison

	Reversible Three Point Bend Test	Mirrored Three Point Bend Test
Fatigue Life (N)	22,832	1,700,324

Using the reversible three point bend test rig to test a completely reversed spectrum with an amplitude of 0.66mm resulted in failure after ~22,800 cycles; Figure 3.10 (black line). Mirroring the negative spectrums about the zero line results in the grey lines shown in Figure 3.10. Failure in this instant occurred after ~1.7 million cycles. These results show that these two tests are not equivalent in terms of damage accumulation and the significance of the zero mean stress line is highlighted (Table 3.4). Therefore, a reversible three-point bend test fixture (see Figure 3.9) is required to test variable amplitude spectrums. The testing fixture was designed such that it can be clamped into the INSTRON.

When setting up the test fixture for a static or fatigue test, the load roller was clamped by the crosshead grip and the fixture was clamped by the bottom grip. Both components were marked with a black pen to allow for easily achievable consistent positioning, though after setting up the camera either/both could be shifted to achieve alignment using the iDS software.

The specimen to be tested was inserted between the two sets of support rollers with the printed ruler facing the camera, one end support was fixed in place (by screw) to ensure reliable placement. The screws located on the top set of support rollers were then tightened by hand after ensuring the specimen was positioned correctly. The grub screws located at the top of the rotating support roller box were then tightened while holding the corresponding screw in place. These grub screws held the rollers at a fixed position relative to the rotating box by preventing the screws from loosening.

The second load roller which was in contact with the underside of the test specimens was then attached to the clamped load roller by screw, a torque wrench was utilised to achieve consistent bracing at the centre of the specimen.

Recording Setup

A uEye (UI-388x Series) camera was implemented to track the position of the crack tip visually throughout testing. Tests were conducted on two specimens which had been previously A-scanned with an initial crack length of 3 inches. These specimens contained some fibre damage at the edge of the specimen and hence were utilised for trialling the camera (Figure 3.11).

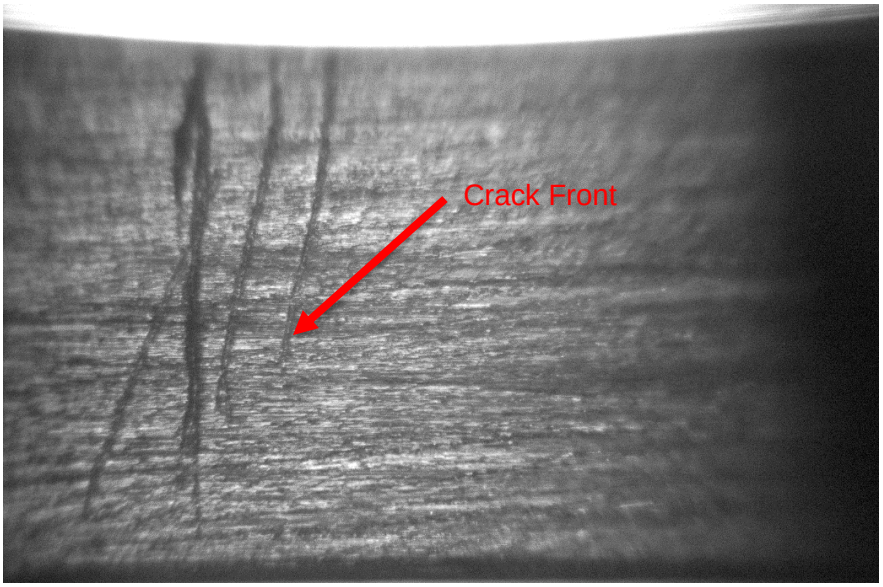

Figure 3-11 Image from the uEye camera displaying the crack tip location

The camera was able to display the crack as it grew, with the top and bottom pieces sliding against each other while under fatigue.

To ensure that the examined region of the specimen maintained consistent lighting conditions throughout the whole duration of testing an attachable ring light was used. A Navitar adapter tube was also attached to the camera to enable magnification such that a field of view of 6mm could be comfortably achieved, though as shown in Figure 3.12 a smaller field of view was also possible.

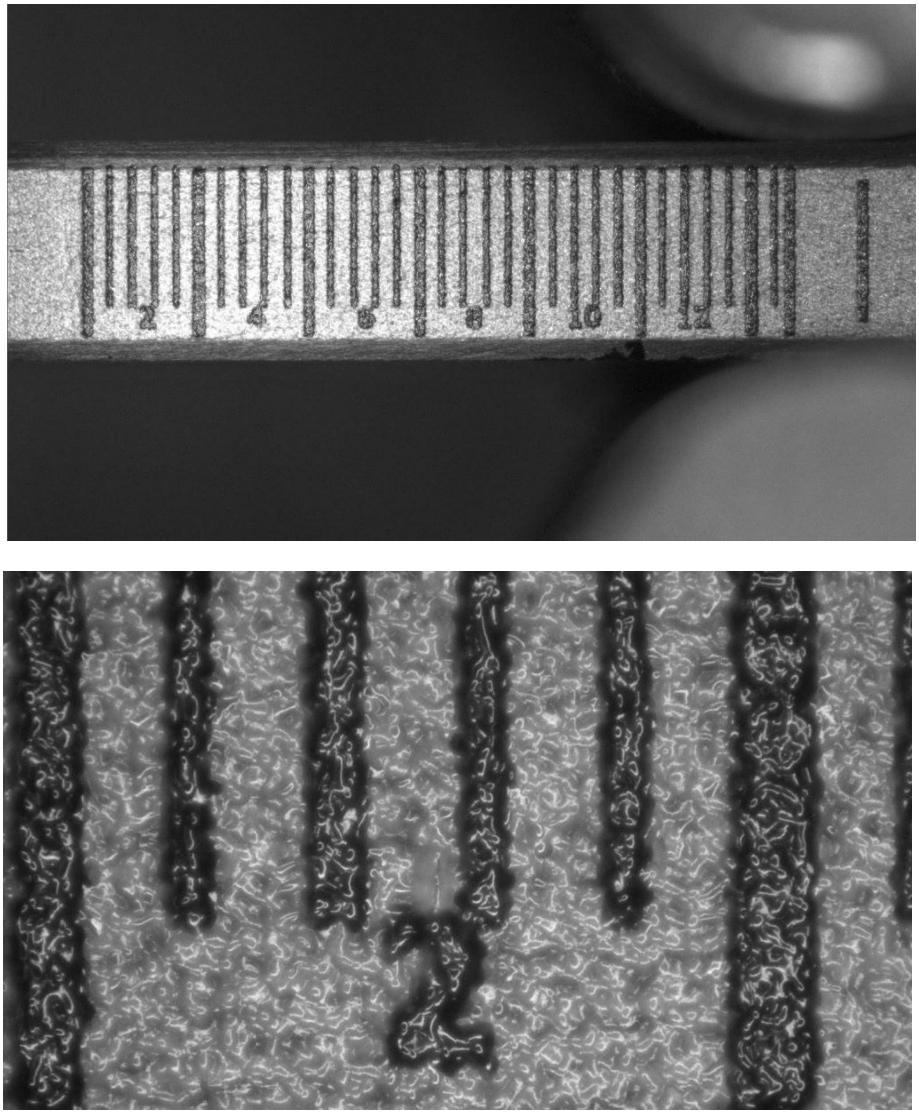

Figure 3-12 Zoomed out and zoomed in view from the uEye camera of a specimen with the printed label

As the duration of fatigue tests can vary from minutes to hours to days it was necessary to ensure that a test could be left running without supervision. A PDV scissor lift stage was attached to a manufactured aluminium support to enable the camera to be fixed to the INSTRON directly rather than using a tripod which required height and angle adjustments.

A manual stage was used for translating the camera towards and away from the INSTRON, while a motorised stage was used for translation along the length of the specimen through the use of an Arduino (Figure 3.13).

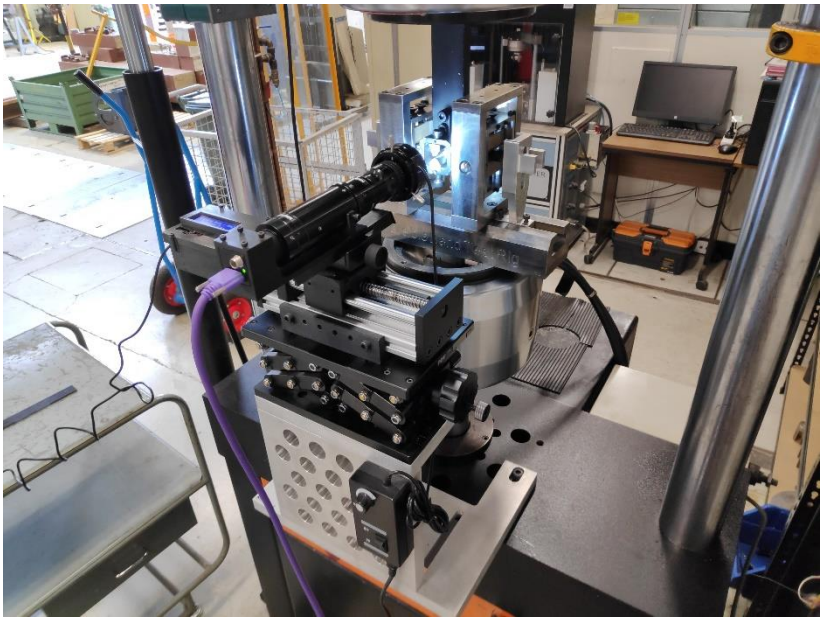

Figure 3-13 View of the automatic stage, Al support, Arduino and camera

The Arduino was coded to enable a button control panel to adjust the position of the camera either by manually holding a button or by clicking a button once to activate a command which periodically translates the camera back and forth (if left unattended).

The camera was connected directly to a laptop which ran both the iDS software; which displayed the camera view, but also OBS screen capture software.

Software

The basic control software used with the INSTRON machine is Material Testing System (MTS) Flex Test Version 5.9B 6027. Both static loading and constant amplitude fatigue loading can be performed using MTS with data directly exportable to Microsoft Excel for processing. Testing

can be controlled by either load or displacement, with load control requiring the machine to be tuned each time a new material is being tested to prevent overshooting, undershooting, etc.

In the vast majority of cases, displacement control was utilised for testing due to its stability and due to load control requiring an additional load cell to enable accurate control at loads ~1kN.

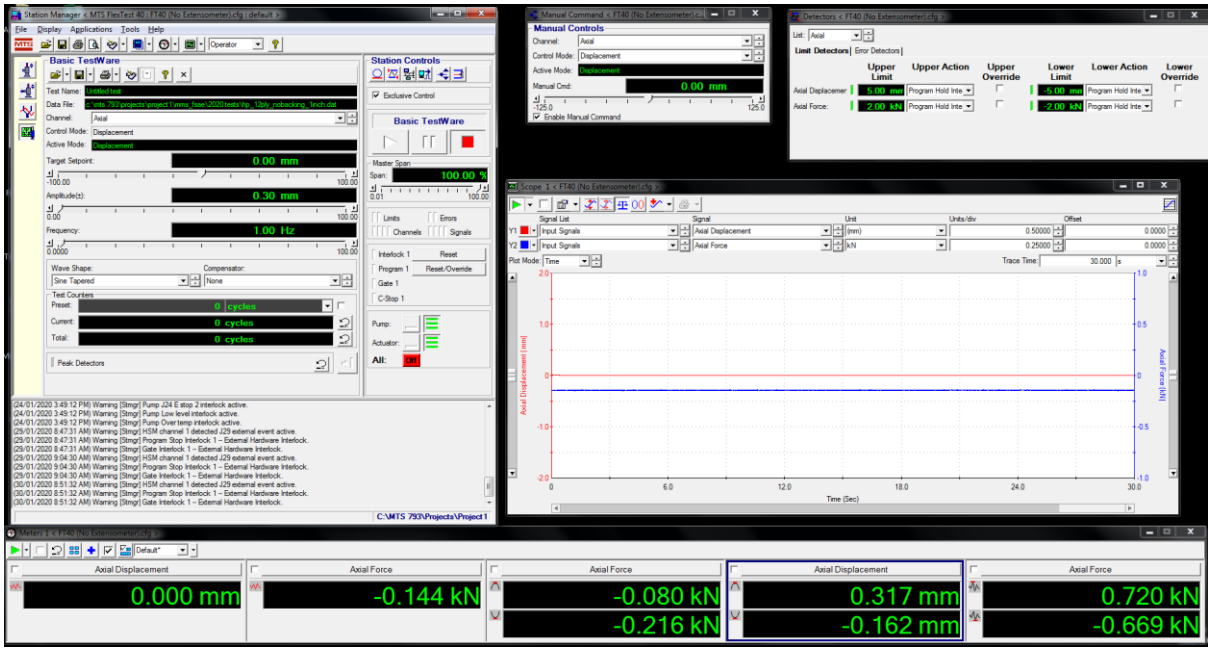

Figure 3-14 MTS software user interface (UI)

Regarding the layout of the user interface, the Scope window provides real time plots of input and output signals, displacement and force displaying the smoothness of the sinusoidal shape (chosen input signal) observable upon commencing fatigue testing. Station Manager (Figure 3.14 top left) is where test parameters, setup, tuning and many other settings are adjusted. The view on display in Figure 3.14 is setup for a constant amplitude test where the mean displacement is 0mm, the amplitude is 0.3mm and the frequency is 1Hz. The two green boxes on the right of Station Manager are the on/off buttons for the stations pumps and actuator. The max/min and running values of both load and displacement are viewable on the Meters (Figure 3.14 bottom), with the max/min values most useful for constant amplitude testing and the running values most useful for

static testing. The Detector window (Figure 3.14 top right) is a safety feature which was enabled before commencing testing, by setting both force and displacement limits the INSTRON machine is prevented from exceeding these chosen values and the test will be halted should they be reached. Finally, the Manual Control (Figure 3.14 top middle) window allows the control to be switched between the user and the MTS software (for running a test), the load and displacement can be incremented when under user control allowing for positioning of the actuator.

In order to conduct more complicated test procedures such as variable amplitude fatigue testing it was necessary to use MTS TestSuite TW Elite software. Through a variety of adjustable test options a procedure can be constructed to perform variable amplitude loading using an input file. More simple variable amplitude loading was also conducted (block loading) by creating a series of constant amplitude blocks inside a loop which controlled how many times an action is performed.

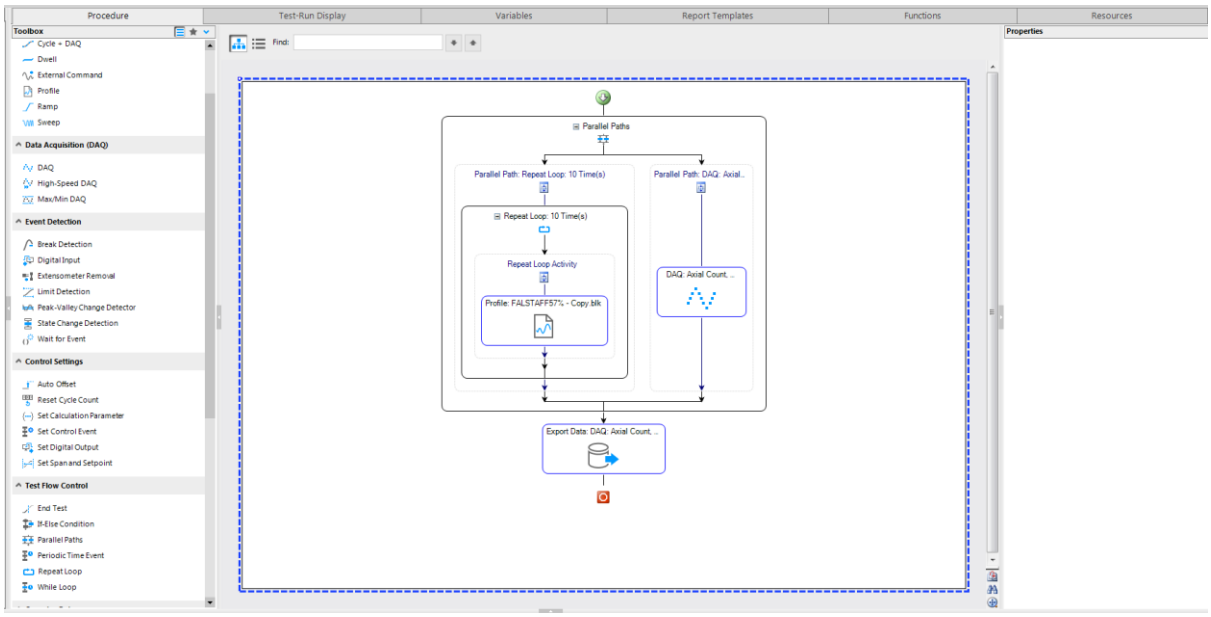

Figure 3-15 MPE software test layout

The Toolbox (Figure 3.15 column on left) provides a vast number of options for both setting up a test procedure but also in collecting data and reacting under given test conditions. As the crack growth data utilised during this study was obtained through visual detection only basic data acquisition settings were utilised. The tested variable amplitude sequences were input through the Profile option which enabled an input file to be used for defining the loading. This input file is sensitive to spaces quotation marks hence great care needs to be taken when creating said file as reselecting input files can result in the actuator shutting off. Thus the author recommends that the input files be created and tested without any test fixture or specimens in the test machine to avoid undesirable damages.

The telescopic camera was used in tandem with iDS software which displayed the camera output as well as allowing for lighting, framerate, and other visual options to be altered. This software was windowed and captured/recording using OBS for post processing of the video files to obtain the crack length and cycle count data.

MATLAB script was written for all generating, predictions and modelling described in this study (with the exception of the FE modelling). The filtering, compression and any adjustments of the FALSTAFF sequence were also performed through MATLAB script.

End of Chapter 3

Chapter 4

Development of Fatigue Life Prediction Models

4.1 Introduction

In order to reduce/compress a fatigue spectrum while conserving its damage content it is necessary to have a means for measuring the damage contribution of each cycle within the sequence. Through calculating the damage, cycles can be omitted, substituted, scaled or retained dependant on whether they are relatively low damaging or highly damaging.

A flexible damage model is capable of predicting failure under a range of loading parameters, and therefore would require a series of experimental fatigue tests for construction. However, to conduct relatively complex variable amplitude fatigue tests it is necessary to accurately determine the specimen's behaviour under constant amplitude fatigue and before that; under static loading. This is to ensure that when scaling/developing a test sequence, the specimens aren't over or under loaded.

Firstly, static tests were performed using both a conventional three point bend test fixture and a fully reversible fixture. These tests provided load-displacement data which enabled the calculation of the mode II interlaminar fracture toughness (G_{IIc}) using the ASTM D7905 [3]. Constant amplitude fatigue tests were designed by taking fractions of G_{IIc} and calculating the required test parameters to achieve $G_{II,max}$.

A variety of constant amplitude tests were completed, with R_d values consisting of -1, -0.1, 0.1 and 0.5. Test parameters were adjusted to ensure that individual fatigue tests wouldn't last more than a week (at 1Hz) as the INSTRON machine is regularly booked by a variety of researchers. Furthermore the ability to measure the crack growth diminished as the stress amplitude decreased (see Section 3.3) making longer tests unattractive when considering accuracy.

Modelling of the constant amplitude data was performed using the Walker equation (Equation 2.16), and when paired with Miner's sum (Equation 2.17) block loading sequences could be developed with intended failure points. As the presence of load sequence effects would greatly impact the spectra reduction process it was necessary to determine whether they were present. Block loading sequences were designed such that when tested forwards and in reverse a comparison of experimental growth data would illustrate any sequence dependence.

Through modifications of both a residual strength model and a crack growth model, conservative predictions of the block loading sequences were made. These analytical formula therefore could be utilised in predicting failure under the selected variable fatigue spectra which would undergo reduction.

4.2 Experimental Procedure

Both static and fatigue tests were conducted using the setup and execution procedure detailed in Section 3.3 Fatigue Testing.

4.3 Results and Observations

4.3.1 Static Testing

ASTM D7905

Mode II fracture testing was carried out as detailed in the ASTM D7905 [3], where the crack length (a_0) was 37.3mm and the specimen was arranged as shown in Figure 2.2.

Both the IM7/977-3 and M18/1/G939 specimens were loaded at a rate of 1mm/min until static failure occurred. Both the displacement and load data were recorded at a sampling frequency above 50Hz. The resulting load-displacement curves are shown in Figures 4.1 and 4.2.

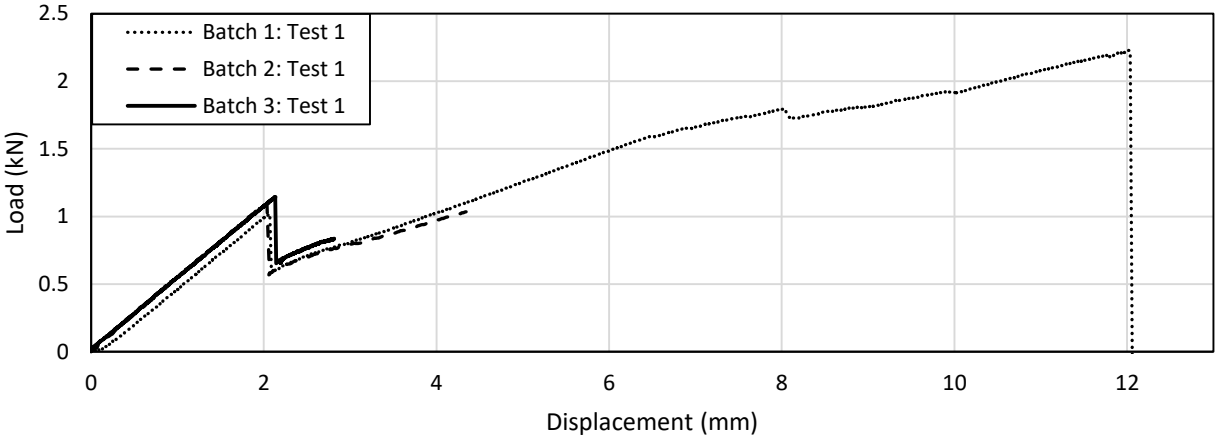

Figure 4-1 Load-displacement curves for static testing of IM7/977-3 specimens

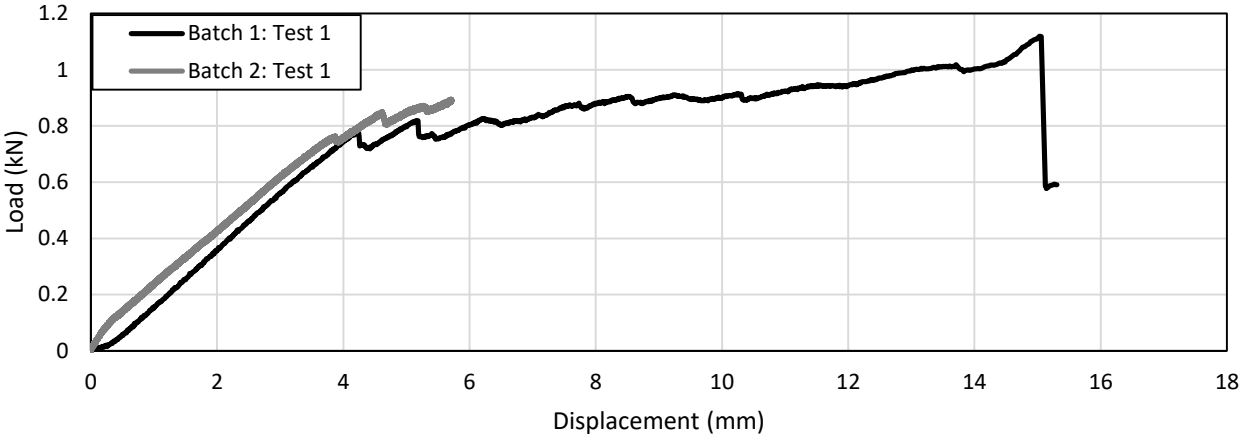

Figure 4-2 Load-displacement curves for static testing of M18/1/G939 specimens

The first peak of each of the curves in Figures 4.1 represents growth of the crack to the centre load nose (confirmed visually with telescopic camera) which results in a drop in the strength of the specimen, hence subsequent loading produces a shallower gradient. As the focus of these tests was the point at which the crack propagates to the load nose, not all tests were continued until catastrophic failure.

To determine G_{IIc} for unidirectional composite specimens the ASTM D7905 requires that several static tests be performed on individual specimens at a variety of crack lengths. The gradient of the load-displacement curve (compliance) is measured as the crack length is changed, this allows for the calculation of a fitting parameter (m) which assists in finding G_{IIc}. This process is known as compliance calibration (CC).

The specimens are loaded to less than 50% of the displacement that induced static failure, ensuring that the compliance/strength of the material doesn't change. The crack length was varied by shifting the specimen horizontally in the loading fixture, values of 20mm, 30mm, 37.3mm and 40mm were tested with the load-displacement curves shown in Figures 4.3 and 4.4. Testing was

also performed on the woven specimens for comparison, however the ASTM D7905 isn't designed for such specimens.

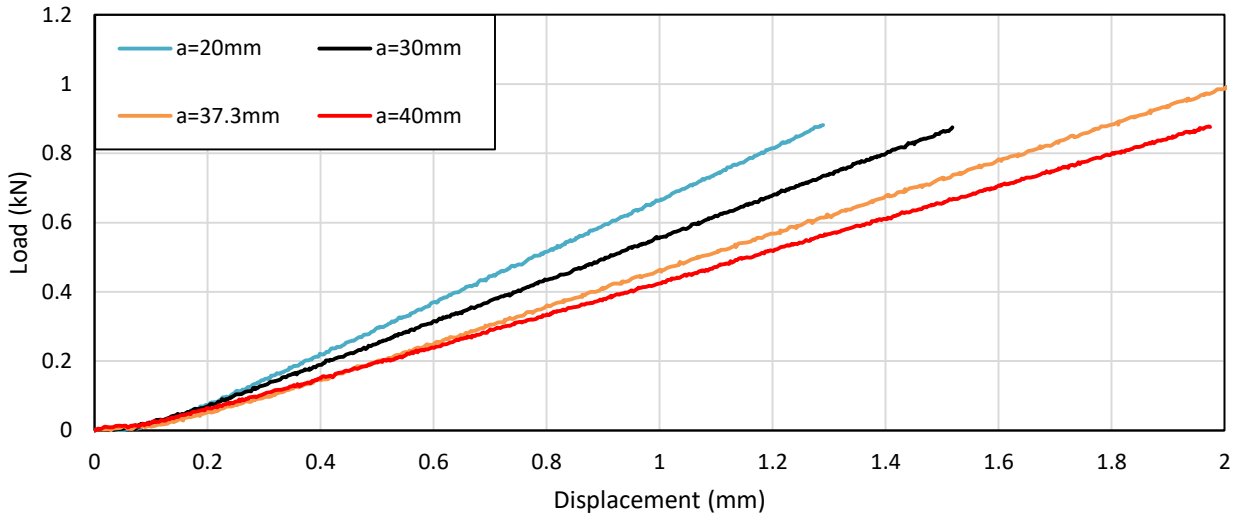

Figure 4-3 Load-displacement curves for IM7/977-3 for various crack length values

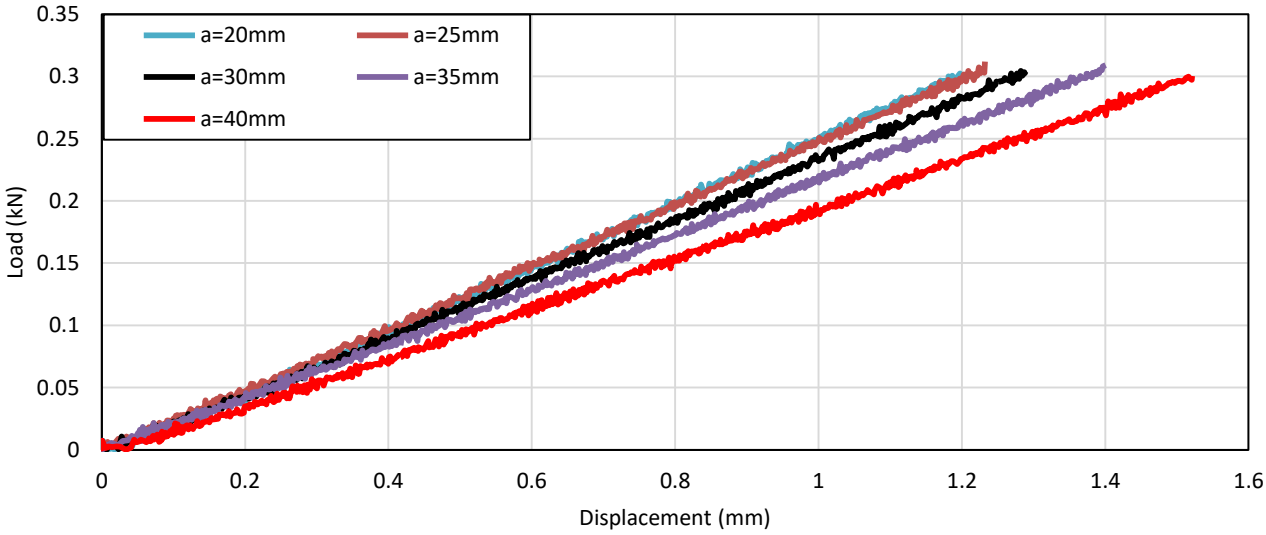

Figure 4-4 Load-displacement curves for M18/1/G939 for various crack length values

Compliance curves were then generated by plotting the gradient of the load-displacement curves against the crack length, each test at a single crack length yields one data point on these curves.

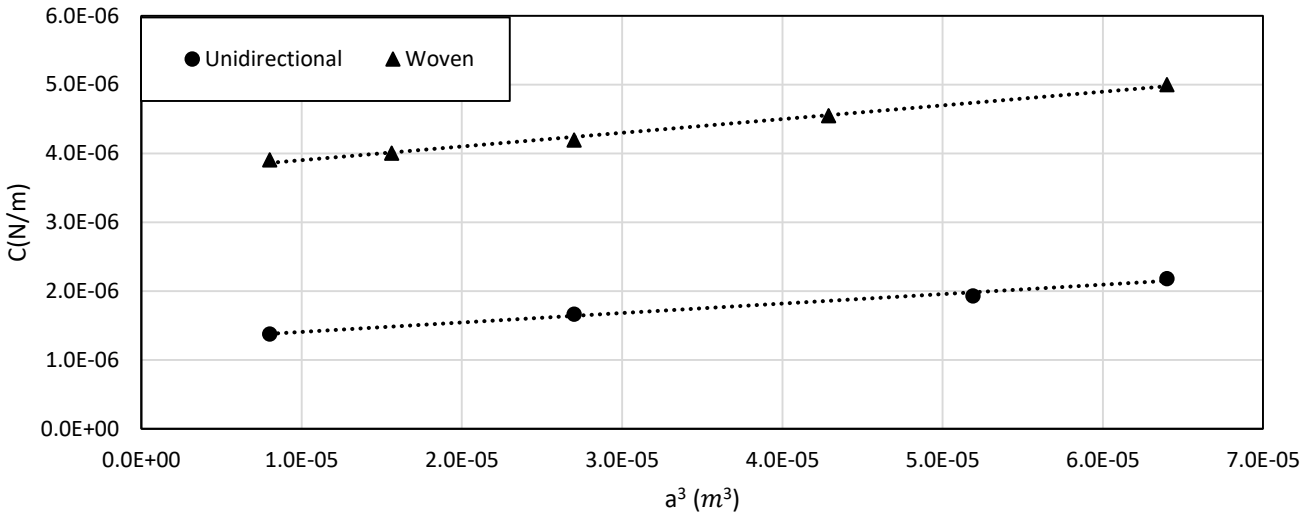

Figure 4-5 Compliance curves for IM7/977-3 and M18/1/G939

The compliance curve was then statistically fit to Equation 4.1

$$C = ma^3 + A \qquad \text{Equation 4.1}$$

Where a is the crack length, C is the compliance and m and A are fitting parameters. Determination of m is the primary purpose of the previous static tests, with the value being utilised to calculate G_{IIc} along with the peak load which initiated static failure as well as other geometric parameters. The values of the parameters were as follows:

Table 4-1 Values of fitting parameters for compliance calibration for both unidirectional and woven specimens

Specimen	***m***	***A***
IM7/977-3	1.373981E-02	1.26866E-06
M18/1/G939	1.989013E-02	3.70307E-06

Utilising Equation 4.1 the G_{IIc} values for IM7/977-3 and M18/1/G939 were determined to be 1175 J/m^2 and 995 J/m^2 respectively. However, as the ASTM D7905 was designed for unidirectional ENF specimens, the woven specimen requires separate analytical formulae. Several

analytical methods were implemented to determine G_{IIc}; Paulo N.B. Reis et al utilised a modified crack length measure which was calculated from the specimen compliance [18], Toshio Ogasawara et al used the more common conjugate beam analysis which takes the peak load and displacement into account [22], A.B. Pereira fit the compliance calibration data to a third order equation and using the resulting parameters calculated G_{IIc} [23], and the ASTM D7905 standard which was intended for unidirectional ENF specimens [118]. These equations are summarised in Table 4.2.

Table 4-2 Alternative analytical equations utilised to calculate G_{IIc}

Reference	Formula	Compliance Parameters	Equation
Paulo N.B Reis et al	$G_{IIc} = \frac{9P^2a_e^2}{16b^2E_1h^3}$	a_e	4.2
Toshio Ogasawara et al	$G_{IIc} = \frac{9P^2Ca_0^2}{2B(2L^3 + 3a_0^3)}$	C	4.3
A.B. Pereira et al	$G_{IIc} = \frac{P^2}{2b}(C_1 + 3C_3a^2)$	C_1, C_3	4.4
ASTM D7905	$G_{IIc} = \frac{3mP_{max}^2a^2}{2B}$	m	4.5

FEA Analysis

An ABAQUS model of the specimen was created to perform a numerical comparison with experimental results, with the intent of validating the numerical determination of G_{IIc} [118]. The model was constructed by defining four separate parts. A specimen part with a section missing above the mid-plane to enable interactions to be applied to different sections of the mid-plane

along the specimens length, which had a 30 ply layup (unidirectional) which was a solid extrude with composite layups. The removed section of the specimen had the same constituents as the remaining section.

Rollers were also modelled as solid half cylinders using the known dimensions of the experimental system with material properties of hardened steel. The friction coefficient between the rollers and the surface of the specimens used was 0.01 [119], to prevent sliding of the specimen.

The crack was modelled by a crack seam, located 3 inches away from the left edge (crack front). The purpose of this was to create a gap between the seam and surface interface allowing for a PTFE interface (Normal Hard Contact) to be enforced between the two specimen mid-planes. A two-dimensional model was initially created to guide testing of the three-dimensional model, results were collected for both for comparison.

The area around the crack tip (~10mm) is seeded with a fine mesh using biased seeding with a sweep control to properly capture the localised stress and displacement as a result of displacement controlled loading [120]. A pinned boundary condition was applied to the two supporting rollers preventing translational movement, while a displacement boundary condition was enforced on the centre of the specimen to prevent sliding. The unique meshing to each method will be discussed in their respective sections.

Simulations were performed for the fracture testing, J-Integral and displacement field. When carrying out numerical analysis, two-dimensional trials were initially conducted as a timely method for assessing the accuracy of the techniques. Analysis was first performed on the relatively simpler unidirectional specimen before extending to the woven specimen.

Displacement Field

To consistently implement the displacement field technique the mesh along which the crack would propagate needs to be uniform. Edges were seeded from the end of the refined region enclosing the crack tip using a single bias from $5 * 10^{-4}$m to $5 * 10^{-3}$m, with hex controlled mesh control. Elements inside the refined region were consistently of size $2 * 10^{-4}$m with a hex sweep mesh control. The element type was C3D8R for the entirety of the specimen model.

Measurements were taken by probing nodes before and after applying a load to the specimen via the load roller. As the path the crack propagates along is certain due to the Teflon insert, the angle θ is consistently 180˚. The mode II strain energy release rate is analogous to the mode II stress intensity factor which can be determined through,

$$G_{II} = K_{II}^2 \left(\frac{1-\nu^2}{E}\right) \qquad \text{Equation 4.6}$$

Which requires both ν Poisson's ratio, and E the Young's modulus. The resulting G_{IIc} estimates at each node were plotted against the corresponding distance from the crack tip. A linear extrapolation was then performed to find the y intercept which corresponds to the G_{IIc} approximation.

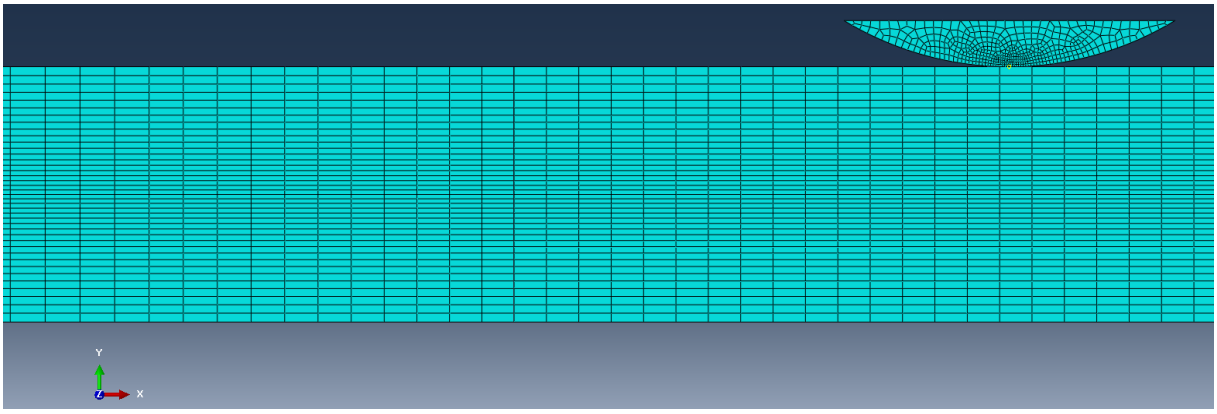

Figure 4-6 A view of the mesh pattern close to the crack tip used when implementing the displacement field technique

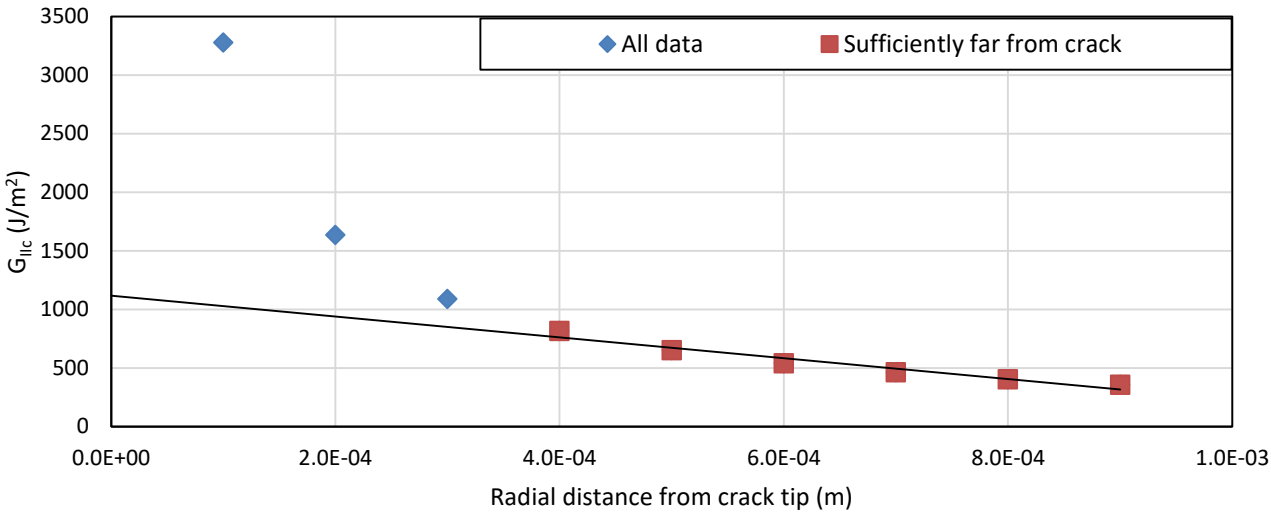

Figure 4-7 Linear extrapolation of G_{IIc} from implementing displacement field for IM7/977-3 3D model

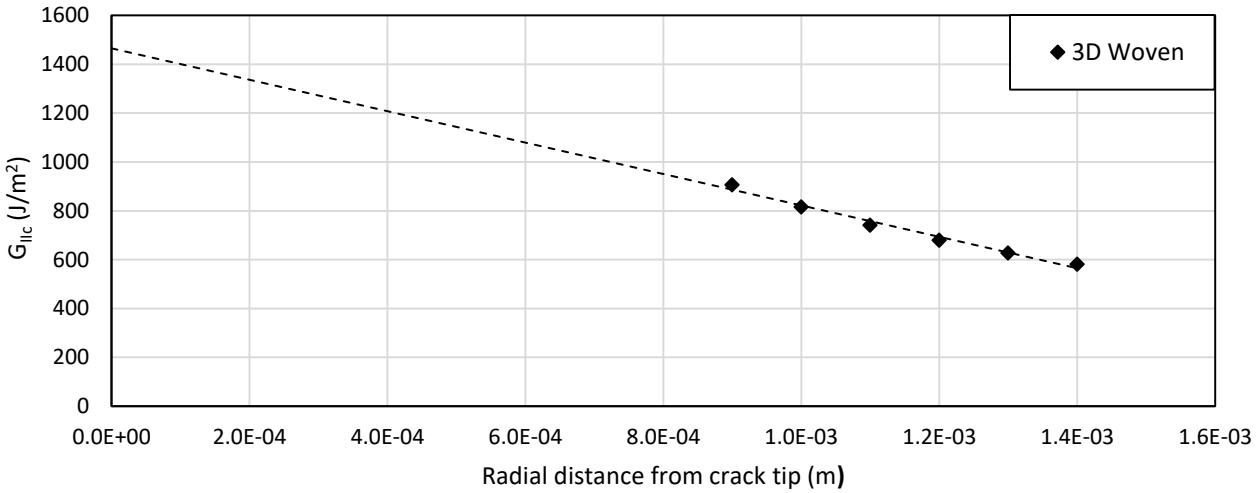

Figure 4-8 Linear extrapolation of G_{IIc} from implementing displacement field for M18/1/G939 3D model

As the radial distance decreases the calculated value of G_{IIc} approached a singularity [121] hence values far enough from the crack tip (such that no exponential behaviour was present) were chosen for the linear fit (similarity of 95%). The resulting G_{IIc} value was determined to be ~1116.83 J/m^2 for the three-dimensional unidirectional model and ~1465.3 J/m^2 for the woven model.

J Integral

A region on either side of the crack tip had its mesh refined to ensure that there were no significant discontinuities in the mesh sizing [122], a biasing factor of 1.2 was applied along the radius of a circle of radius 0.005 m with the mesh concentrated towards the crack tip comprised of 9 elements, with C3D6 elements. The circle was split into 4 quarters each with 13 elements (no bias), and a smaller circle surrounding the crack tip (radius of $4 * 10^{-5}$m) just as the larger circle had a wedge sweep mesh control. All circles surrounding the crack were enclosed by a square which restricted element size to $1 * 10^{-4}$m. The remainder of the model was comprised of C3D8R structured elements that were at largest $5 * 10^{-3}$m and at smallest $5 * 10^{-4}$m, with single bias applied from the crack tip region outwards.

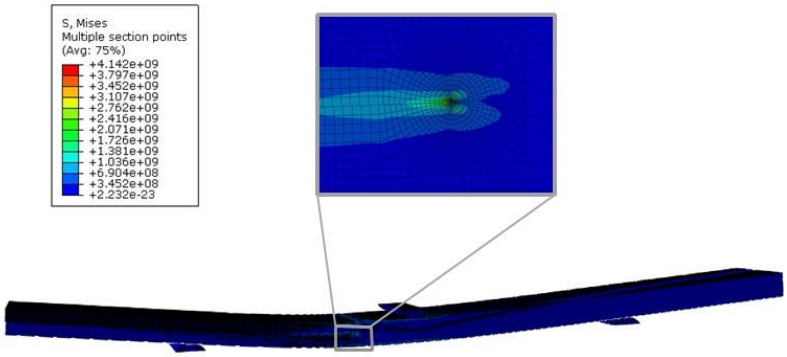

Figure 4-9 A view of the FEA three point bending model with the crack tip highlighted

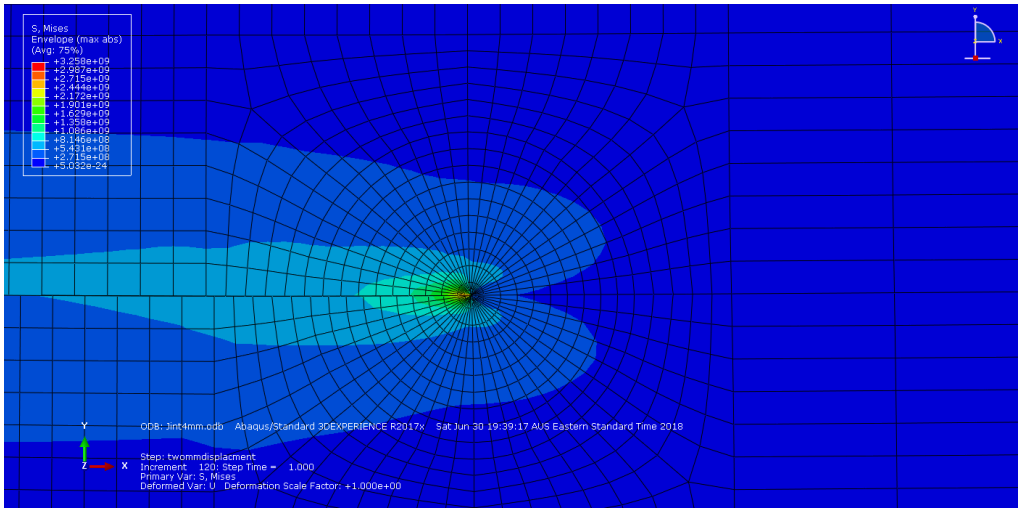

Figure 4-10 A zoomed in view of the mesh pattern close to the crack tip used when performing the J integral in ABAQUS

Due to the J integral functionality in ABAQUS, a sweeping mesh was implemented around the crack tip rather than a structured mesh as shown in Figure 4.10. This was beneficial because contour integrals are calculated as layers of elements surrounding a crack front. Five contours were constructed to produce five G_{IIc} (J integral) values, each had a circular/curved shape.

The J-integral displayed high accuracy through the width of the specimen (i.e. comparing Contour 'X' at different depths) with all contours having a standard deviation (σ^2) less than ~2.53, indicating the transition from two to three-dimensions didn't adversely reduce the J-integrals accuracy. However, the accuracy when comparing the contour to each other did return a more sizable σ^2 of 84.45 with an average G_{IIc} of ~1284 J/m^2.

The experimental static results demonstrated the behaviour described by the ASTM standard, with Figure 4.1 showing an initial linear relation between load and displacement followed by a steep drop corresponding to crack growth to the loading roller. Though the woven specimens do exhibit a shallower drop than the unidirectional, the followed change in gradient confirms the specimens experienced damage. Using the critical points of the fracture tests as a means for safely loading within the linear region, compliance calibration was performed with peak displacements of ~2mm

and ~3.8mm (unidirectional and woven respectively). The unidirectional specimen achieved a similarity of 98.8% with the linear fit on the compliance curve implying strong correlation, this validated retaining the CC results and using Equation 3.5 to calculate G_{IIc} (1174.9 J/m^2). The woven specimen displayed equally good linear behaviour with a 99.4% similarity, however the ASTM 7905 was designed for unidirectional FRPMC specimens not for woven FRPMC specimens hence Equations described by Reis et al [18] (amongst others) were utilised to calculate G_{IIc} to be 1408.1 J/m^2.

Table 4-3 Summary of unidirectional specimen G_{IIc} values (J/m^2) across both analytical and numerical methods.

	Analytical Method		**Numerical Methods (FEA)**		
	ASTM7905	Std	ABAQUS CC	J Integral	Displacement Field
G_{IIc} (J/m^2)	1175.85	115.63	1238.45	1283.99	1116.83

Table 4-4 Summary of woven specimen G_{IIc} values (J/m^2) across both analytical and numerical methods.

	Analytical Methods			**Numerical Methods (FEA)**		
	Paulo N.B. Reis	Toshio Ogasawara	A.B. Pereira	ASTM7905	J Integral	Displacement Field
G_{IIc} (J/m^2)	1408.11	1546.72	1422.9	995.07	1302.78	1465.3

The J integral prediction was within 10% of the experimental value, but indicated that the model was excessively stiff, signalling for implementation of a progressive damage model. The displacement field method on the other hand produced three-dimensional results which were within ~5% of the experimental results (1116.83J/m^2), with both two and three-dimensional models generating similar results (within 9%).

All analytical methods (except the ASTM D7905) fall within 10% of each other giving a reasonable range for the numerical results to reside in. The ASTM D7905 demonstrated a significant underestimation of G_{IIc} for the woven specimen with a value of $995.07\ J/m^2$. The J integral and displacement field elastic results both fell within the analytical range with values of $1302.78\ J/m^2$ and $1465.3\ J/m^2$ respectively.

The general agreement between experimental and numerical results for the unidirectional specimen justified extending the numerical modelling to the woven specimen. The resulting woven analysis demonstrated agreement between several analytical sources and the implemented numerical methods.

4.3.2 Constant Amplitude Fatigue Testing

In order to attribute damage to unique cycles within a sequence it is necessary to model constant amplitude fatigue experimental results to enable predictions of untested loading parameters. Using the experimentally determined G_{IIc} value from the static testing detailed in Section 4.3.1 a series of constant amplitude fatigue tests were designed.

Testing was conducted using the unidirectional specimens first due to their relative simplicity compared to the woven specimen, hence the methodology for spectrum reduction was first implemented to the unidirectional specimen (Chapters 4 and 5) [77].

By rearranging Equation 3.5 for P_{max} in terms of G_{IIc} tests sufficiently below the critical limit were performed based on Table 4.5, results from several static tests were averaged. The displacement limits were calculated using the compliance calibration results from Section 4.3.1 using the load limits.

Table 4-5 Average maximum load and displacement limits for constant amplitude fatigue test for IM7/977-3 specimens

	G_{II}	P (N)	$P/P_{load\ drop}$ (%)	Disp (mm)
10%	107.26	305.27	31.62	0.661
20%	214.52	431.72	44.72	0.935
30%	321.78	528.75	54.77	1.145
40%	429.04	610.54	63.25	1.322
50%	536.30	682.61	70.71	1.479
60%	643.57	747.76	77.46	1.620
70%	750.83	807.67	83.67	1.749
80%	858.09	863.44	89.44	1.870
90%	965.35	915.82	94.87	1.984
100%	1072.61	965.31	100	2.091

As the influence of the amplitude ratio (R_d) on the fatigue limit was largely unknown until several test were conducted, to avoid excessively long or abrupt failure a displacement limit corresponding to 50% G_{IIc} was commonly the first experiment of any unique R_d value. As fatigue spectra such as FALSTAFF include a large range of R_d values which are rarely integers, R_d values selected for testing were spread from -1 to 0.5 to reduce the need for extrapolation in Section 4.4. Several batches of IM7/977-3 were utilised for constant amplitude testing with repeat tests being performed for select displacement limits.

Specimens were considered to have failed upon crack propagation to the centre load nose which corresponds to 11.7mm of crack growth after 1mm of pre-cracking. Pre-cracking was performed to keep the shape of the crack tip a relatively consistent between tests.

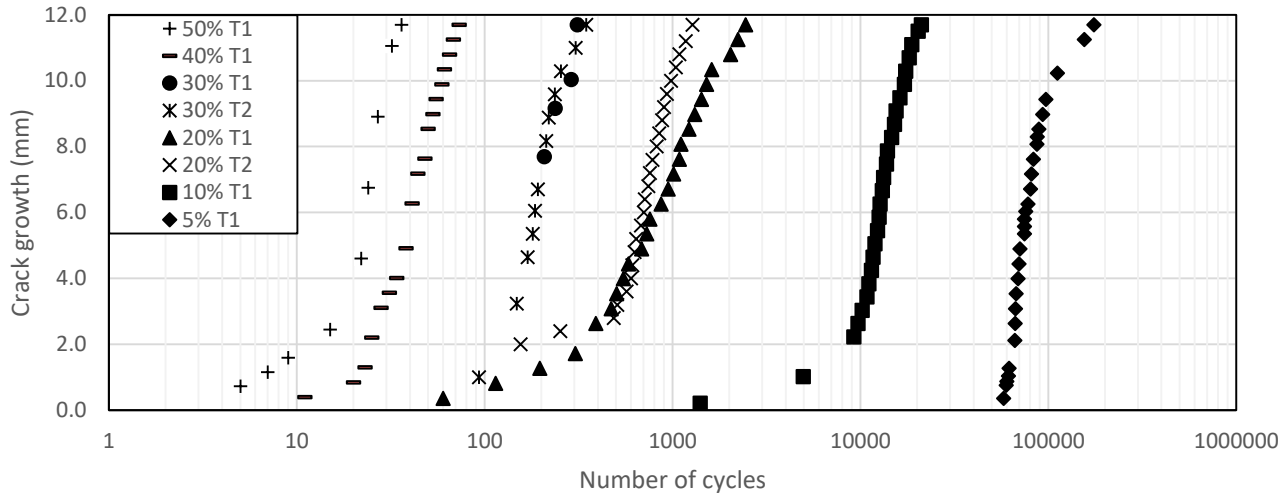

Figure 4-11 Crack growth data for IM7/977-3 loaded with R_d=-1 constant amplitude displacement controlled fatigue tests

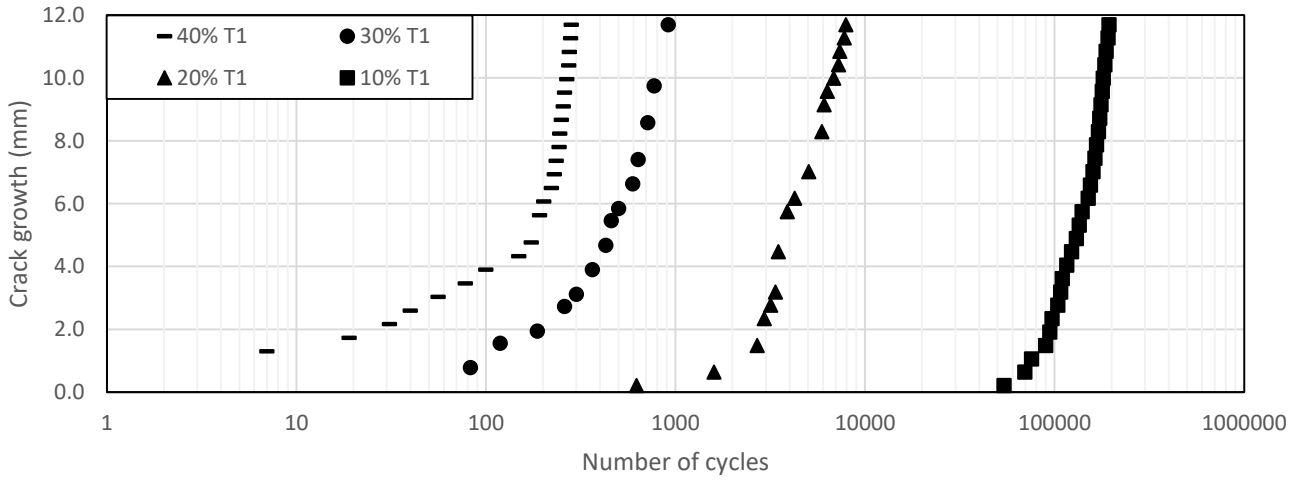

Figure 4-12 Crack growth data for IM7/977-3 loaded with R_d=-0.1 constant amplitude displacement controlled fatigue tests

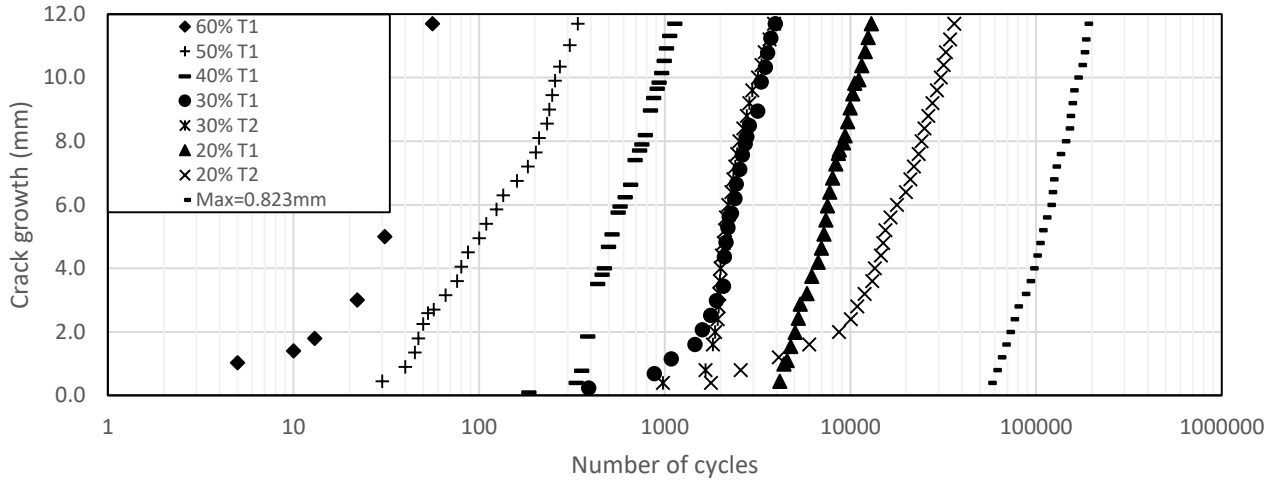

Figure 4-13 Crack growth data for IM7/977-3 loaded with R_d=0.1 constant amplitude displacement controlled fatigue tests

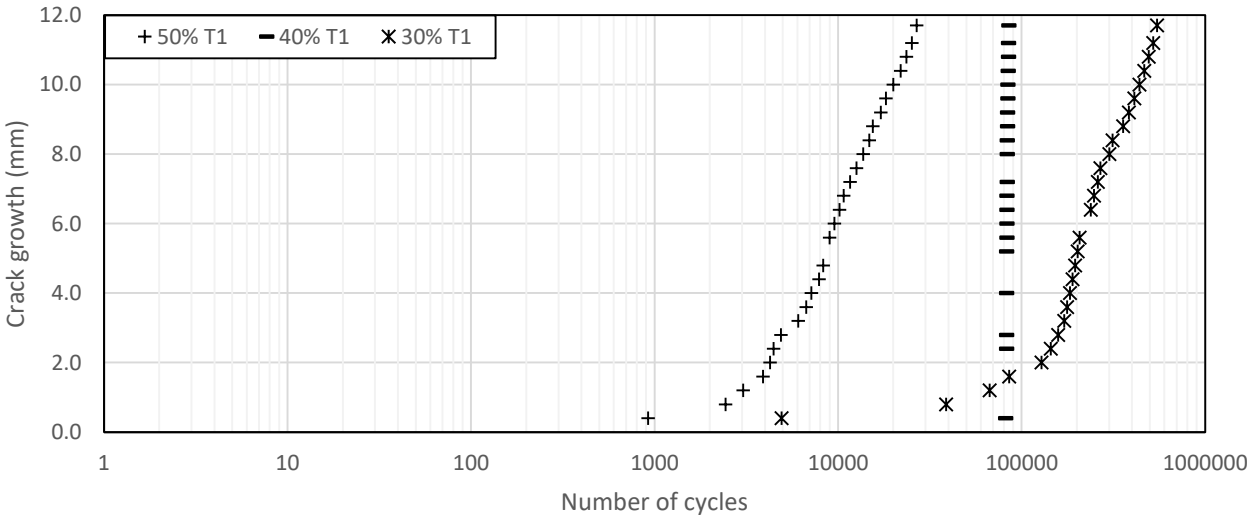

Figure 4-14 Crack growth data for IM7/977-3 loaded with R_d=0.5 constant amplitude displacement controlled fatigue tests

By comparing the crack growth curves displayed in Figures 4.11 – 4.14 it is apparent that as the R_d increased the smoothness of the curves declines. This is due to the manner in which the crack length is measured. As the higher the R_d value is, the lower the stress amplitude becomes hence

the relative movement between the shearing surfaces also lessens. Being visually measured, identification of the crack tip becomes significantly more difficult with only subtle shearing motion. As such lower displacement limits and higher R_d values were avoided to reduce measurement error.

From the defined failure point of 11.7mm of crack growth each curve in Figures 4.11 – 4.14 produces a single data point on an S-N curve. However, as testing was performed under displacement control the maximum stress experienced by the specimen cannot be assumed to be constant throughout the fatiguing process. As the maximum stress is proportional to load, load controlled tests will theoretically have constant maximum stress limits as when the crack grows and the specimens strength degrades the displacement limits will increase. But under displacement control the load limits will decrease as less force is required to achieve specified displacement limits for a weaker specimen. To enable comparison with load controlled tests the displacement level ($\delta_{max}/\delta_{static}$) was utilised instead of maximum stress for the r_d-N curves.

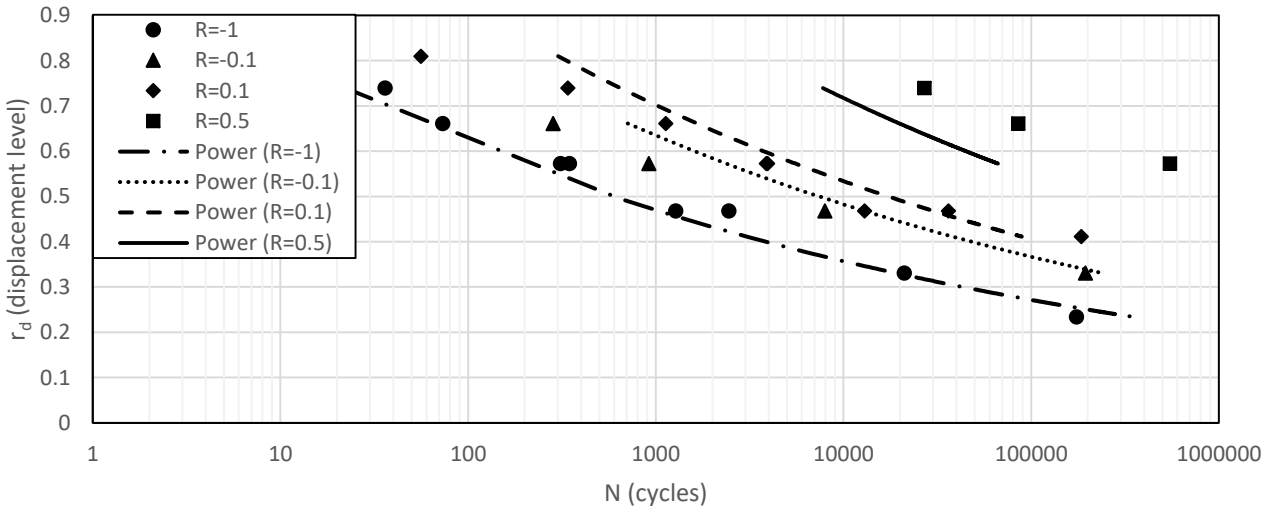

Figure 4-15 r_d-N curves for IM7/977-3 for R_d=-1, -0.1, 0.1 and 0.5 under displacement control with predictions based on the Walker Equation

It can be observed in Figure 4.15 that the r_d-N curves somewhat plateau as N increases, however no endurance limit was experimentally detected as longer tests involve the not insignificant risk of power outages, maintenance and more likely other researchers desiring use of the INSTRON machine (also the limitations of visual measurements).

As previously mentioned testing for high R_d values (beyond ~R_d=0.5) posed restrictions on the accuracy of crack tip measurements. To attempt to address this issue a test procedure involving low damaging R_d=-1 cycles was introduced for the purpose of crack tip measuring. Fatigue tests loaded under a R_d value of 0.7 were conducted with a measuring block occurring after a certain number of "test cycles" as depicted in Figure 4.16.

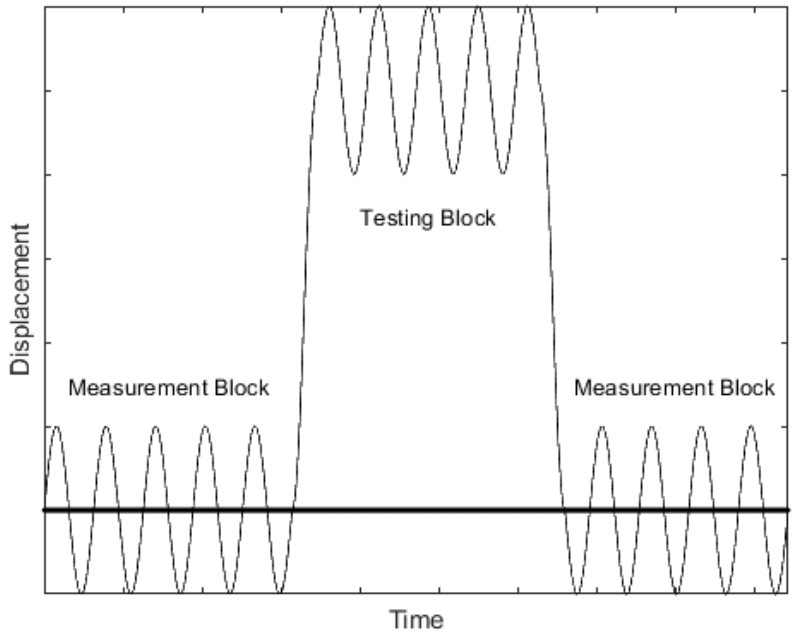

Figure 4-16 The general procedure implemented for R_d=0.7 constant amplitude fatigue tests

The number of cycles per testing block were varied from test to test based on the expected failure point (this was judged using the S-N curves from Figure 4.15). Only the "test cycles" were considered when measuring the cycle count resulting in the following crack growth curves.

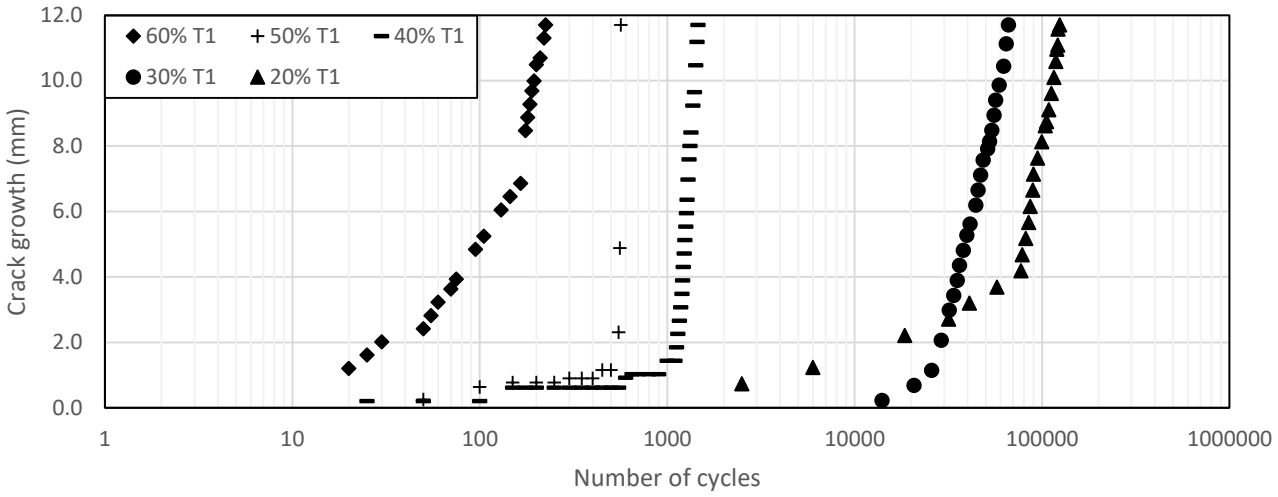

Figure 4-17 Crack growth curves for IM7/977-3 loaded with R_d=0.7 displacement controlled fatigue tests with both measurement and test blocks

While the R_d=-1 cycles were sufficiently low damaging for measuring purposes, the ramping from the "measurement cycles" to the "test cycles" (and vice versa) constitutes a highly damaging half cycle at R_d=0. As this transition occurred regularly due to the desire to accurately track the crack tip from each marked increment the half cycles were highly prevalent in each test.

Using the R_d=0.5 for comparison it is reasonable to infer that the R_d=0 half cycles were the main cause of crack propagation. However, due to the possible sequence interactions this data wasn't utilised for modelling of constant amplitude growth behaviour.

4.3.3 Block Loading Fatigue Testing

Whether the sequence of cycles affects the fatigue behaviour of composites requires experimental assessment as this has been an area with mixed views. Hence several block loading fatigue tests were conducted for this investigation [77]. To extend a model to fatigue life predictions of variable amplitude spectrums, a series of block loading cases were developed and experimentally

tested. These block loading cases (variable amplitude) consist of different amplitude ratios and displacement amplitudes and are repeated from high to low amplitude cycles as well as low to high amplitude cycles.

The following four low amplitude to high amplitude block load cases were created to experimentally determine final failure of the IM7-977-3 composite specimen subjected to Mode II testing using the reversible three point bend test setup (see Figure 3.9). Each block loading case was tested from low amplitude to high amplitude and continuously cycled until final failure was reached (crack growth of 11.7 mm). Four additional high amplitude to low amplitude cycles were also tested; these were the reverse cases of the sequences shown in Figure 4.18 and termed Block Sequence A - high amplitude to low amplitude (A-HL), Block Sequence B - high amplitude to low amplitude (B-HL), Block Sequence C - high amplitude to low amplitude (C-HL) and Block Sequence D - high amplitude to low amplitude (D-HL) respectively.

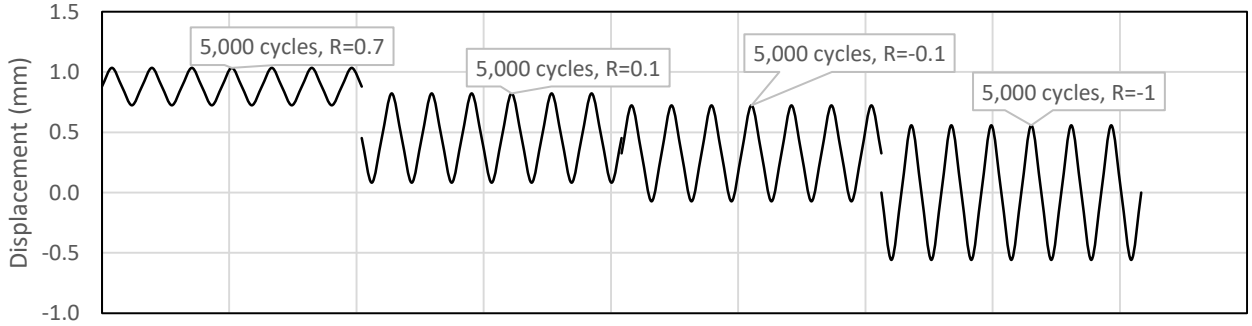

(a)

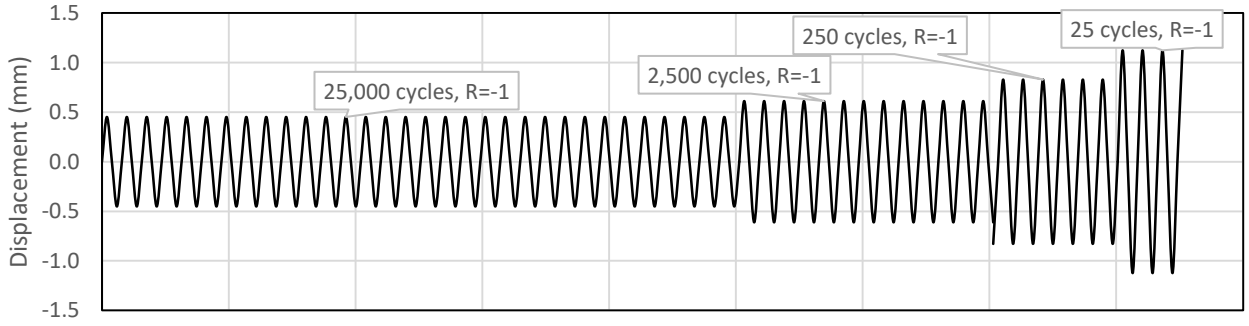

(b)

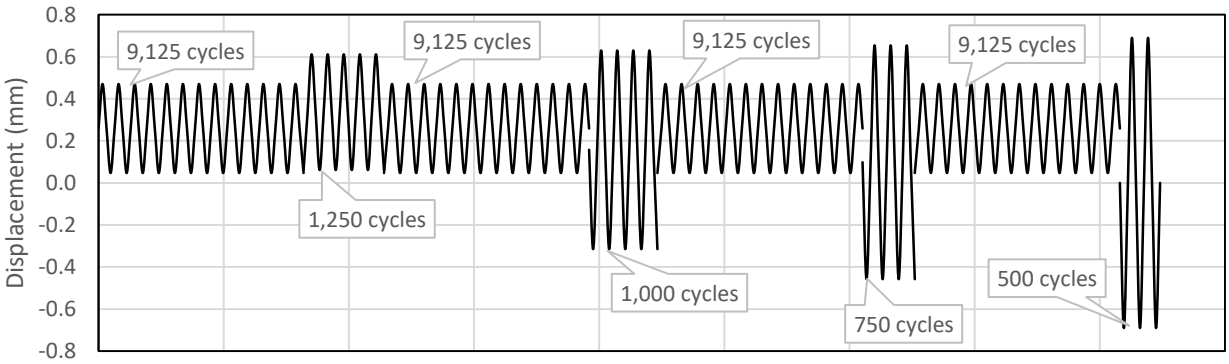

(c)

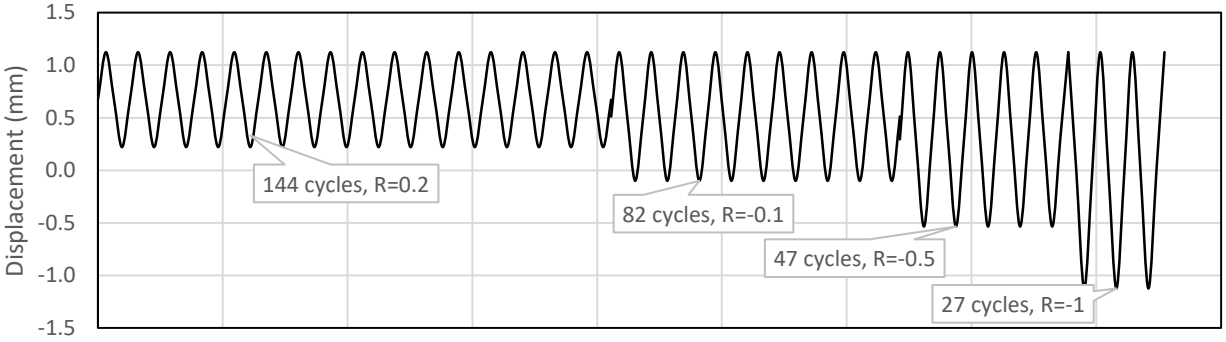

(d)

Figure 4-18 (a) Block Sequence A - low amplitude to high amplitude (A-LH); (b) Block Sequence B - low amplitude to high amplitude (B-LH); (c) Block Sequence C - low amplitude to high amplitude (C-LH); (d) Block Sequence D - low amplitude to high amplitude (D-LH)

The number of cycles in each block of all sequences was based on having a damage fraction of 0.05 (based on Walker's equation and Miner's rule). Thus this method assumes final failure occurs after five passes through the entire spectrum. This method intuitively defines no means of keeping track of cycle sequence effects. However, this design was conducted before all constant amplitude testing was completed (hence also modelling of said data), this results in the damage fraction of each block actually being different (in many cases significantly) from the original design. To avoid confusion between the original designs intentions (based on previous modelling) and the final model, the damage fractions will not be used for measuring and no assumptions of damage content will be made.

Fatigue tests were conducted under the block loading sequences displayed in Figure 4.18 both in forward and reverse cycle order. Similarly to the constant amplitude tests the position of the crack tip was tracked against the cycle count.

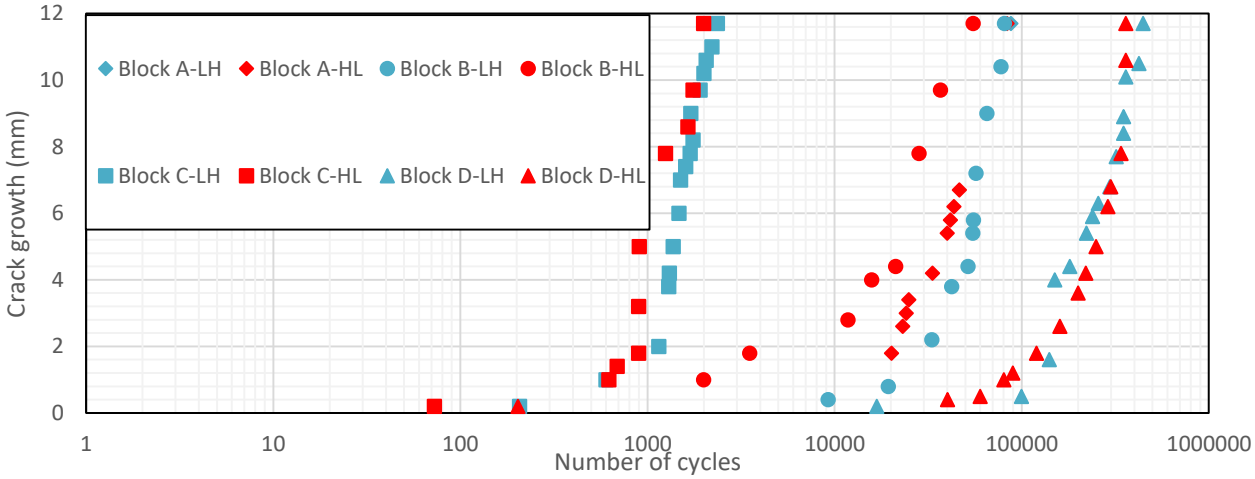

Figure 4-19 Crack growth curves for IM7/977-3 loaded with block loading displacement controlled sequences

The video recording of Block Sequence A L-H was lost hence only the end point is plotted as the test was manually stopped upon failure (Figure 4.19). Due to the unbalanced distribution of cycles in each loading block (particularly in Block Sequence B) the number of passes until failure was also measured to provide a more useful comparison between H-L and L-H loading.

Table 4-6 Experimental fatigue test data based on the low-high and high –low block sequence test for IM7/977-3. The numbers in the brackets are the pass counts, each block is considered to be 0.25 passes for Sequences A, B and C and 0.125 for Sequence D

	Block Sequence A		**Block Sequence B**		**Block Sequence C**		**Block Sequence D**	
	LH	**HL**	**LH**	**HL**	**LH**	**HL**	**LH**	**HL**
Experiment	87,492 (4.37)	83,366 (4.16)	80,787 (2.27)	54,997 (1.99)	2,362 (7.69)	1,993 (6.81)	445,329 (11.15)	360,112 (9.06)

Experimental testing of the block loading sequences showed notable distinctions between HL and LH sequences, with Block Sequence D producing a difference of greater than 20% between the two. In all cases failure occurred earlier in the HL sequences than that in LH sequences.

4.4 Analytical Modelling

Two types of model are developed in this section to enable predictions for loading under both constant amplitude fatigue and variable amplitude fatigue. Constant amplitude fatigue data collected in Section 4.3.2 will be fit to both a residual strength and crack growth rate model, with the more suitable model being utilised in future sections.

4.4.1 Residual Strength Model (RSM)

The two parameter wear-out model detailed by D'Amore et al. (Equation 2.31) utilises both static failure data and constant amplitude fatigue data to determine its fitting parameters. D'Amore et al. developed this model using load-controlled fatigue tests, thus, in this study modifications were required to enable its use under displacement control. Under load-control the maximum stress under constant amplitude fatigue is constant hence the plateau corresponding to the maximum loading stress is the representation of failure. For displacement controlled fatigue, the applied load decreases as the crack propagated due to matrix failure, as a result the maximum stress decreases. As the load changes a new residual strength curve very close to the previous loading (but with a slightly smaller maximum stress) will become the current loading curve. This process will repeat until failure, meaning many residual strength curves would be required to trace the loading of a single constant amplitude test. However, if this process is approximated to a single curve then only the lowest maximum stress would be required, along with adjustments to the parameters controlling the shape and scale of the curve.

To account for this, the maximum stress under constant amplitude fatigue was modified such that it corresponds to the maximum stress once the crack has grown until failure. By using the compliance calibration results obtained by following the ASTM D7905/D7905M the load at failure ($a = 50mm$) and therefore the maximum stress was deduced. Both the shape and scale parameters (δ and γ) were adjusted with factors, which were determined by ensuring the failure points of each curve under Block Sequence B were close to that of experimental tests, using the H-L/L-H failure points as a guide. Using the average virgin strength (σ_0) and the loading parameters (σ_{max}, R_d) paired with the results failure data (N) the fitting parameters α and β were determined (Table 4.7).

Table 4-7 Parameters of D'Amore's two parameter wear-out model determined for IM7/977-3 using Equation 2.29

Parameter	Value	95% CI
α	1.2619	[-0.03967,2.564]
β	0.0919	[0.02547, 0.1584]

After determining α and β a Weibull fit was performed on Equation 2.32 rearranged such that it was of the form $\sigma_0(\sigma_{max}, R_d, N)$. The *wblfit* function in MATLAB was utilised for the analytical fitting with the σ_0 data set being the only input. The resulting parameters are displayed in Table 4.8.

Table 4-8 Parameters of D'Amore's two parameter wear-out model determined for IM7/977-3 using a Weibull fit

Parameter	Value	95% CI
γ	399.3511	[384.3680, 414.9183]
δ	10.6545	[7.9928, 14.2025]

As discussed earlier adjustments were made to both γ and δ through the use of separate factors. Where γ was modified with a factor of 0.912, while δ was modified with a factor of 2 resulting in:

$$\gamma = 364.2082 \text{ and } \delta = 21.3090.$$

Following the calculation of the four fitting parameters the RSM was implemented for the block sequences with the residual strength tracked and plotted using MATLAB. The resulting traces are shown in Figures 4.20-4.23.

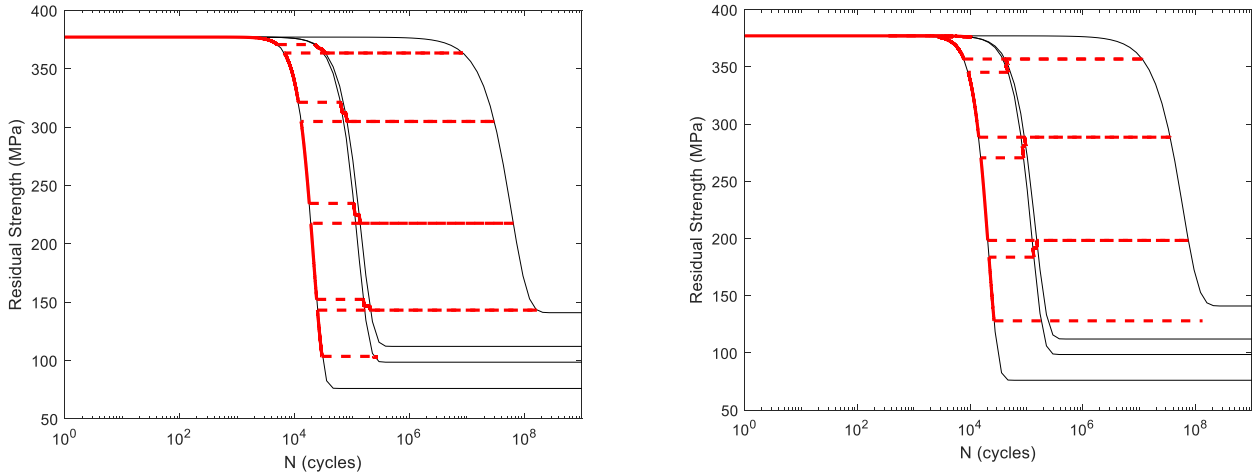

Figure 4-20 Residual Strength curve predictions of IM7/977-3 under Block Sequence A L-H (left) and H-L (right)

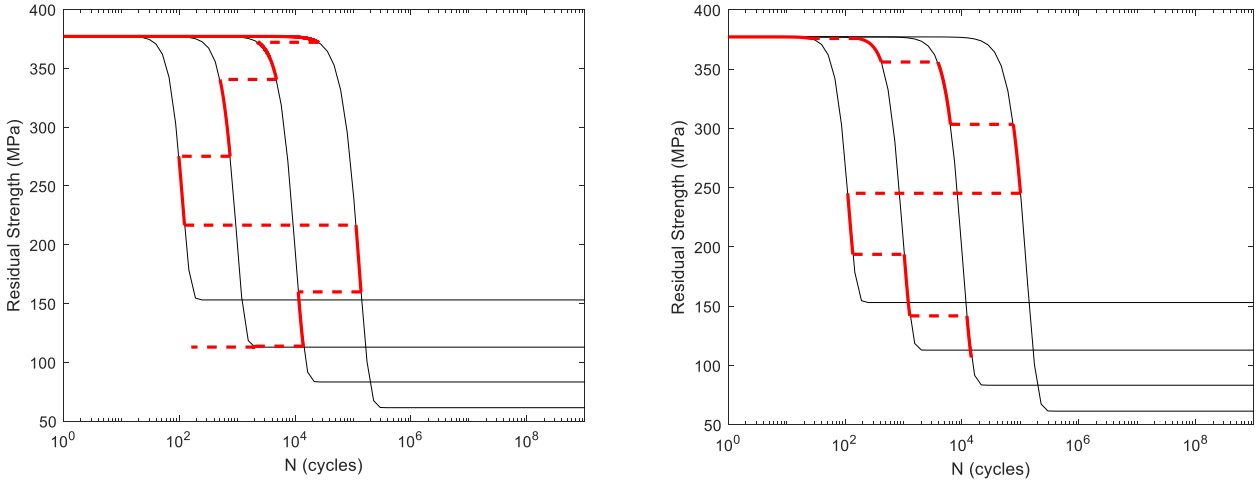

Figure 4-21 Residual Strength curve predictions of IM7/977-3 under Block Sequence B L-H (left) and H-L (right)

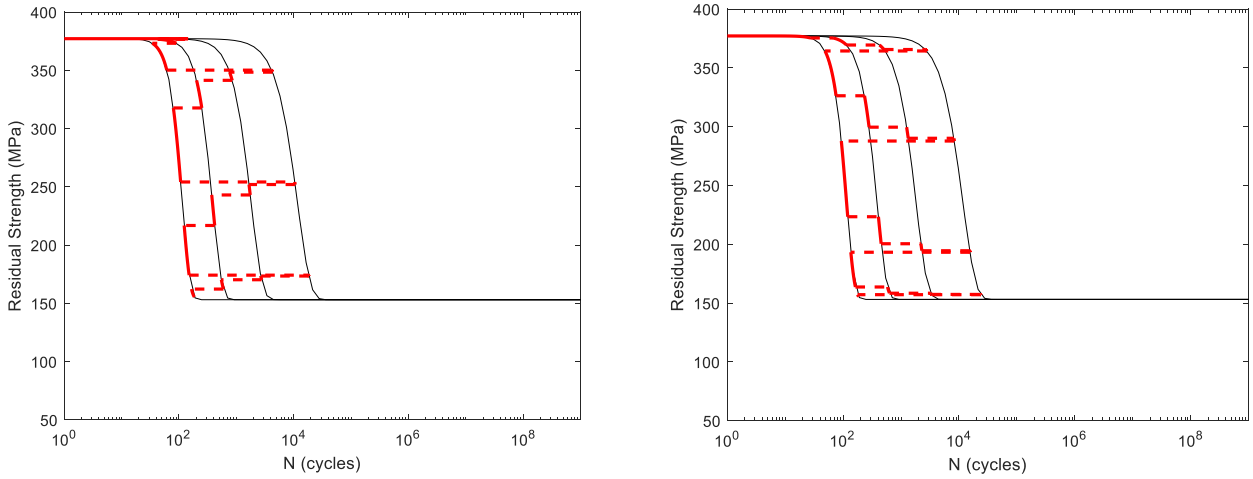

Figure 4-22 Residual Strength curve predictions of IM7/977-3 under Block Sequence C L-H (left) and H-L (right)

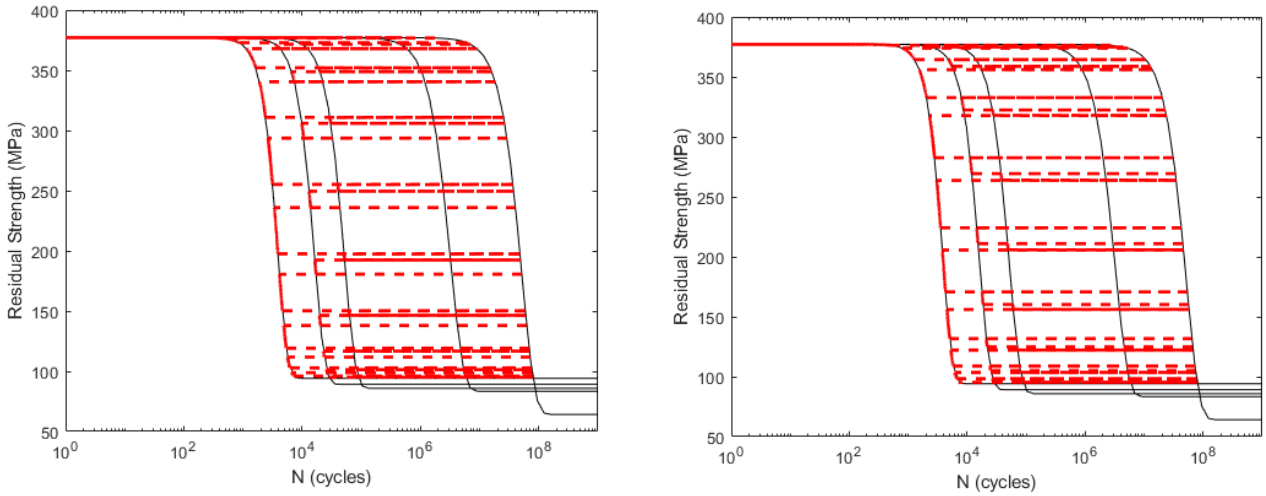

Figure 4-23 Residual Strength curve predictions of IM7/977-3 under Block Sequence D L-H (left) and H-L (right)

Tabulating these failure results and comparing the RSM to the linear damage model of Walker-Miner:

Table 4-9 Comparison of the cycle count at failure for experimental fatigue tests based on the low-high and high-low block sequence tests; Walker's equation with Miner's rule (W-M), Residual Strength Model (RSM). The numbers in the brackets are the pass counts, each block is considered to be 0.25 passes for Sequences A, B and C and 0.125 for Sequence D

	Block Sequence A		Block Sequence B		Block Sequence C		Block Sequence D	
	LH	**HL**	**LH**	**HL**	**LH**	**HL**	**LH**	**HL**
Experiment	87,492	83,366	80,787	54,997	2,362	1,993	445,329	360,112
	(4.37)	(4.16)	(2.27)	(1.99)	(7.69)	(6.81)	(11.15)	(9.06)
W-M	119,610	114,890	101,052	83,333	1,464	1,221	579,816	560,084
	(5.98)	(5.99)	(3.18)	(3.08)	(4.70)	(4.19)	(14.42)	(14.02)
RSM	80,000	90,000	55,525	30,326	1,193	1,208	389,720	360,230
	(4)	(4.5)	(1.75)	(1.73)	(3.94)	(4.07)	(9.64)	(9.06)

The residual strength method displayed notable accuracy for Block Sequences A, B and D (all within 25%), though the predictions for Block Sequence C showed significant difference but was still conservative. Block Sequence D exhibited the largest difference between H-L/L-H experimentally (~2 passes) and this was represented by the RSM which displayed the largest gap of ~0.6 passes. While the H-L/L-H behaviour exhibited for Block Sequence B and D both show L-H to be less damaging the other two cases show the opposite. For Block Sequence A this can be attributed to the significant difference between damage contribution of each block, leading to large amounts of damage accumulating under one of the four blocks making failure occur upon switching to a subsequent loading block, this behaviour is somewhat exhibited in the L-H case of Figure 4.20.

Overall, the RSM produced significantly more accurate and largely conservative predictions for the number of cycles/passes until failure than the Walker-Miner approach. Since the variable amplitude testing showed that the sequence of cycles indeed affects fatigue behaviour of Mode II delamination in these composites, this will be considered when attempting fatigue spectra simplification.

4.4.2 Crack Growth Rate Model (CGRM)

Crack growth data is commonly presented on crack growth rate curves typically as $f(G) = da/dN$, where $f(G)$ is determined using the maximum load values throughout the test. Compliance calibration (CC) modelling which followed the ASTM 7905 [3] (Section 4.3.1) was utilised to determine the corresponding maximum loads for constant amplitude fatigue tests using the crack length which was monitored during tests.

The Batch 1 specimen is the data from Figure 4.1 for the IM7/977-3 specimen, while one failed Batch 3 specimen was used for testing by shifting it in the test fixture to an uncracked region, whereas the other underwent a constant amplitude fatigue test. As the static and constant amplitude fatigue results displayed good agreement a four term compliance model was implemented to determine P_{max} given values for δ_{max} and a.

Using the crack growth rate data and compliance enabled determination of P_{max}, crack growth rate curves were generated for the constant amplitude fatigue tests.

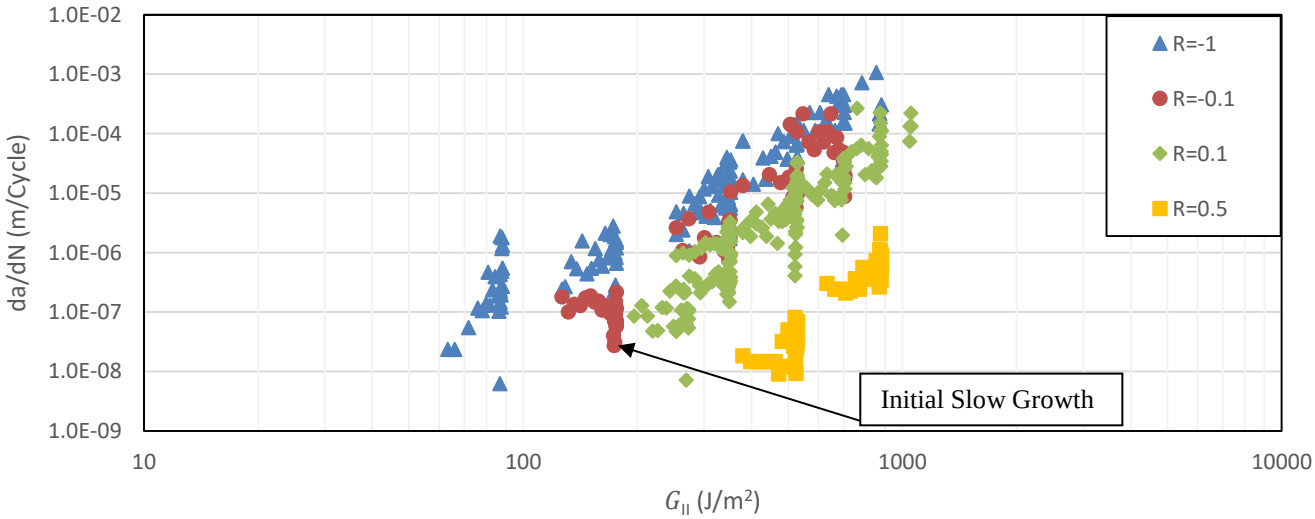

Figure 4-24 Crack growth rate data as a function of $G_{II,max}$ for IM7/977-3 specimens

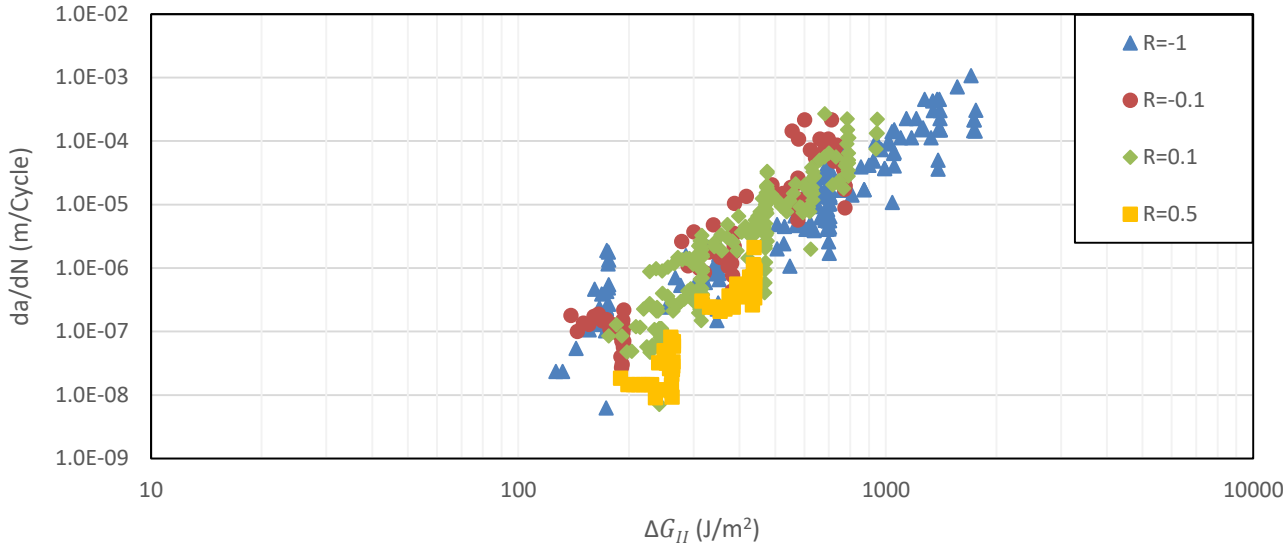

Figure 4-25 Crack growth rate data as a function of ΔG_{II} for IM7/977-3 specimens

While the majority of the data points collapse onto a single curve upon plotting $\frac{da}{dN}$ with ΔG_{II}, the general characteristics of the experimental test aren't being represented as initially the crack propagates slowly before reaching the maximum growth rate and then declining in the linear manner associated with Paris' law. As integrating the curve in Figure 4.25 to determine crack growth would ignore the initial behaviour which accounts for the first ~6.7mm of crack growth, predictions would be unrepresentative.

This initial slow growth behaviour has been attributed to short crack effects, methods for addressing this growth frequently involve threshold factors which influence the G measure (for which $\frac{da}{dN} = f(G)$) for small G values and quickly ceases adjusting once G increases notably in value. This behaviour was also observed by O'Brien [123] when testing specimens with Teflon inserts, hence after sufficient pre-cracking said growth should be witnessed. However, due to the limited amount of crack growth possible with the ENF specimens used in this study the growth characteristics due to the Teflon insert were incorporated into the crack growth rate modelling.

As the fatigue tests were performed by O'Brien under load control the G_{max} value will continue to increase as the specimen undergoes fatiguing. However, when considering displacement control, the G_{max} value will decrease as the crack propagates (as $G_{max} \sim P_{max}^2$), meaning that threshold values can't be implemented in the same manner as load controlled modelling.

With the intent being to create a single unified curve which can be integrated to determine the crack growth rate given arbitrary loading conditions at an arbitrary crack length (within a range of $a = 0.0383m$ to $a = 0.050m$), the piecewise expression, Equation 4.7 was developed.

$$G_{II,max,adj} = \begin{cases} G_{II,max} * \left(1 - E_{adj}(a_t - a)\right) & if\ a \leq a_t \\ G_{II,max} & if\ a > a_t \end{cases} \qquad \text{Equation 4.7}$$

Where $G_{II,max}$ is the maximum mode II strain energy release rate, $G_{II,max,adj}$ is the adjusted value of $G_{II,max}$ and $E_{adj} = 20$ is the adjustment factor which aligns crack growth rate data at crack lengths before $a = a_t$. The parameter a_t was set to 0.045m as the highest $G_{II,max}$ values calculated using CC throughout all constant amplitude experimental test was observed at $a \approx 0.045m$, hence the effects of the Teflon become negligible for larger crack lengths.

Similarly to using $\Delta\sqrt{G_{II}}$ to collapse the $\frac{da}{dN}$ curves for each R_d value, AR Anilchandra et al. [94] utilised Equation 4.8.

$$G_{eq} = \Delta G^{(1-\mu_f)} G_{max}^{\mu_f} = G_{max}(1 - R_d)^{2(1-\mu_f)} \qquad \text{Equation 4.8}$$

Where the only difference is the introduction of the parameter μ_f to allow for the best fit for the $\frac{da}{dN}$ versus G_{eq} curve, which enabled manual parameter fitting. Through trial and error μ_f was selected to be 0.4 (observing which value best collapsed the curves without leading to an overly steep curve). The curves before and after the implementation of Equation 4.8 are displayed below in Figures 4.26 and 4.28 respectively. Figure 4.27 demonstrates the use of ΔG rather than G_{eq} to collapse the crack growth data sets. While the data fitting depicted in Figures 4.27 & 4.28 is very similar, the ability to control the alignment of data sets for each R_d value as well as the consistency between ΔK from Paris' law, made the use of G_{eq} preferable.

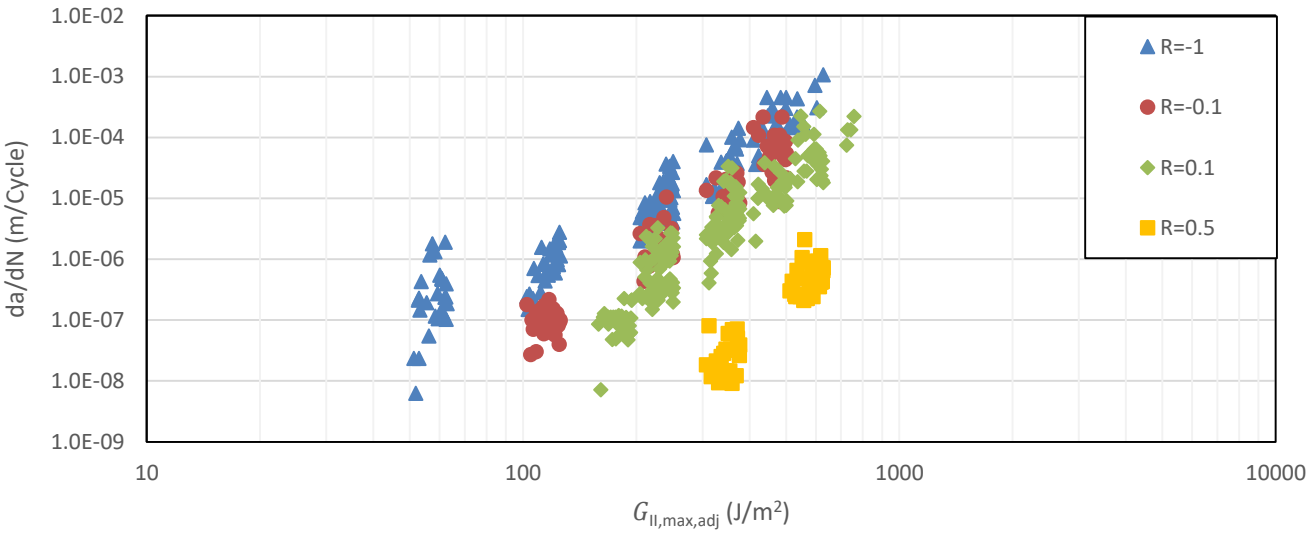

Figure 4-26 Crack growth rate data as a function of $G_{II,max,adj}$ for IM7/977-3 specimens using Equation 4.7

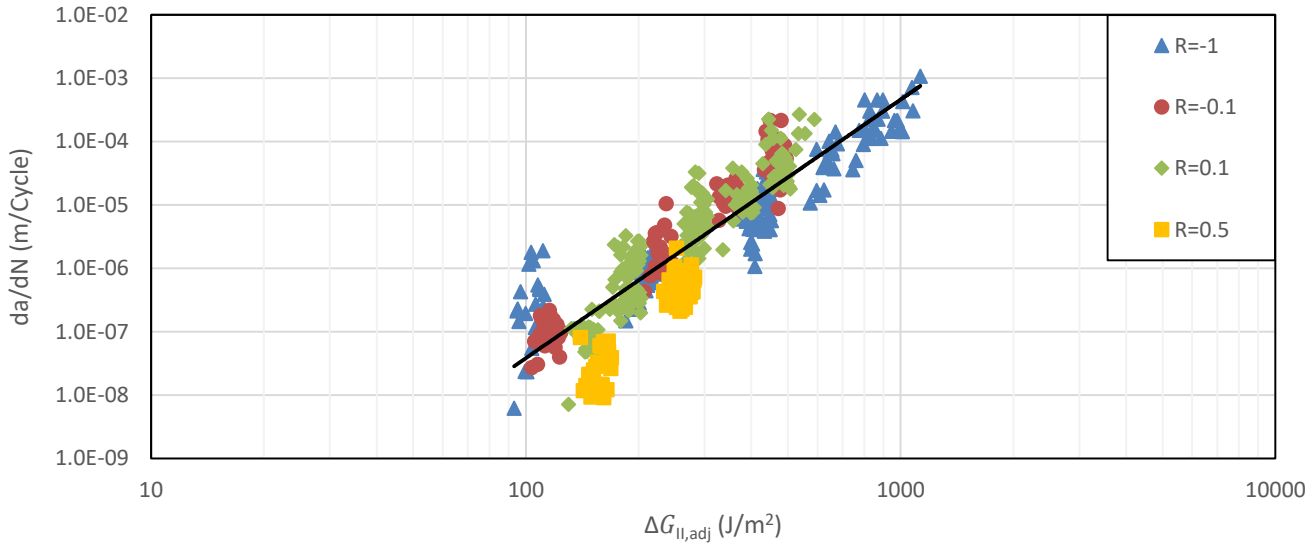

Figure 4-27 Crack growth rate data as a function of $\Delta G_{II,adj}$ for IM7/977-3 specimens using Equation 4.7

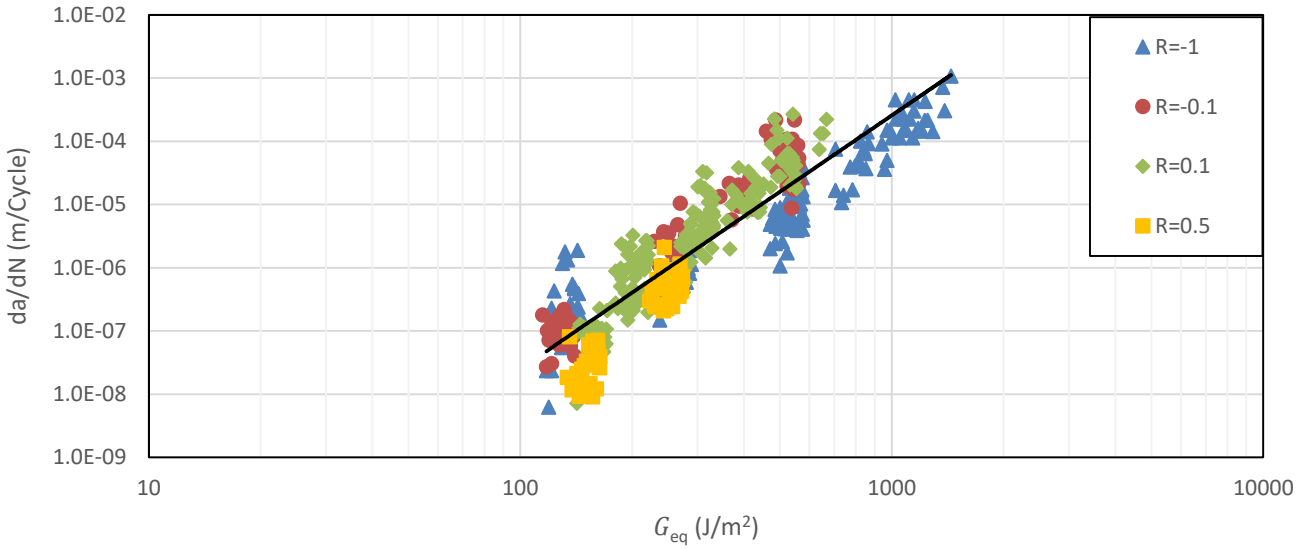

Figure 4-28 Crack growth rate data as a function of G_{eq} for IM7/977-3 specimens using Equations 4.7 and 4.8

Hence the fit crack growth rate equation can be written as

$$\frac{da}{dN} = D_p(G_{eq})^{n_p} \qquad \text{Equation 4.9}$$

Where D_p and n_p were determined to be $2.349 * 10^{-16}$ and 4.0129 respectively.

By integrating Equation 4.9 the constant amplitude fatigue experimental tests can be predicted for the purpose of comparison.

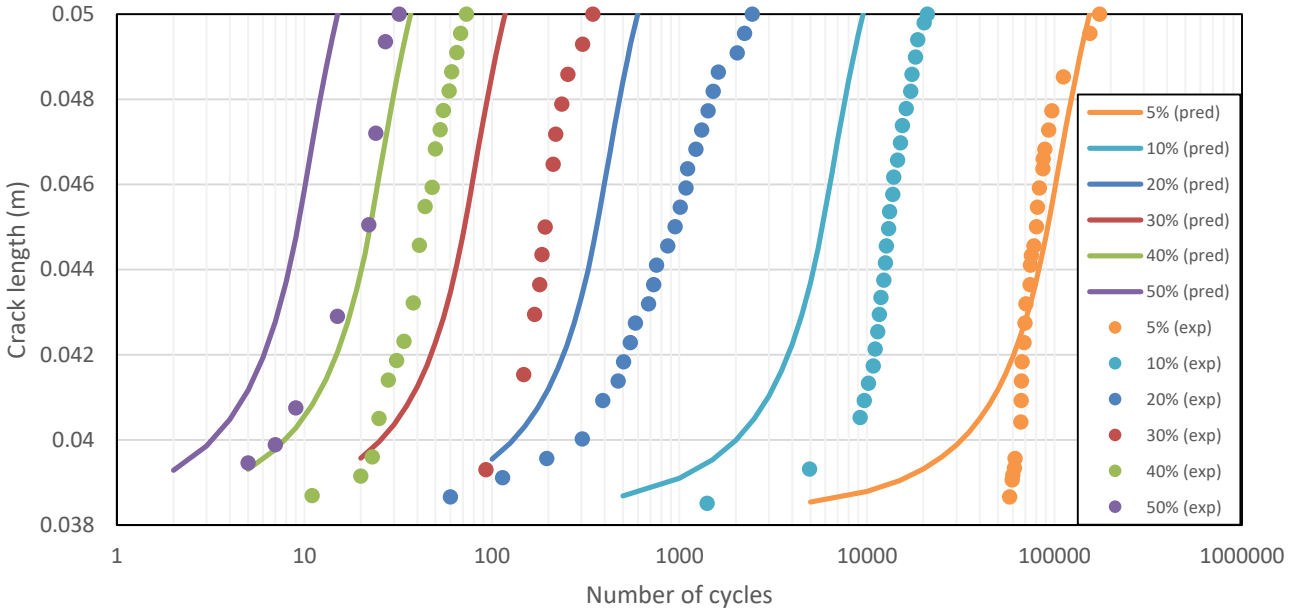

Figure 4-29 Crack growth curves for IM7/977-3 loaded at R_d=-1 under constant amplitude fatigue compared to predictions using Equation 4.9

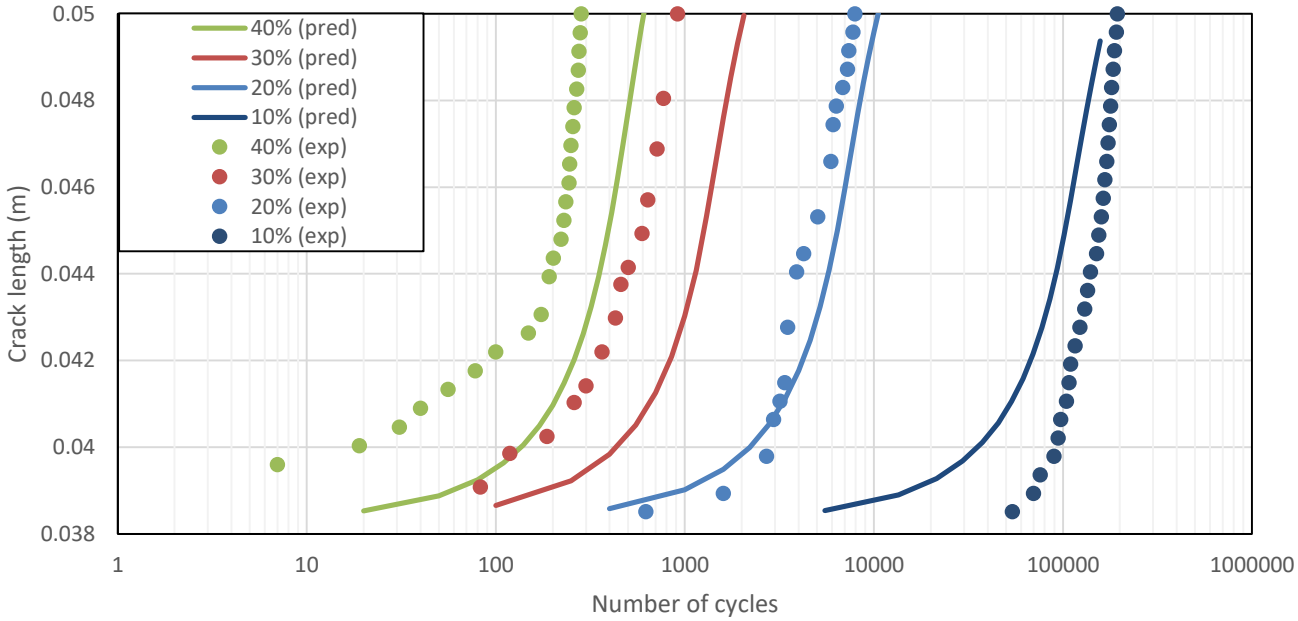

Figure 4-30 Crack growth curves for IM7/977-3 loaded at R_d=-0.1 under constant amplitude fatigue compared to predictions using Equation 4.9

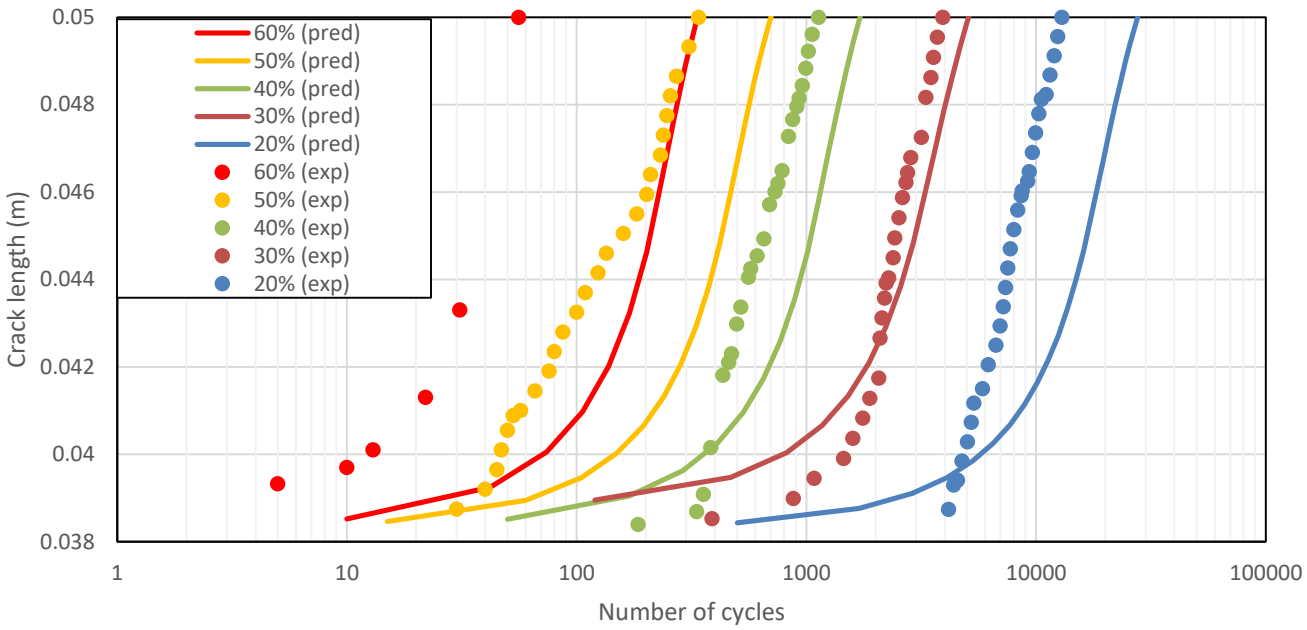

Figure 4-31 Crack growth curves for IM7/977-3 loaded at R_d=0.1 under constant amplitude fatigue compared to predictions using Equation 4.9

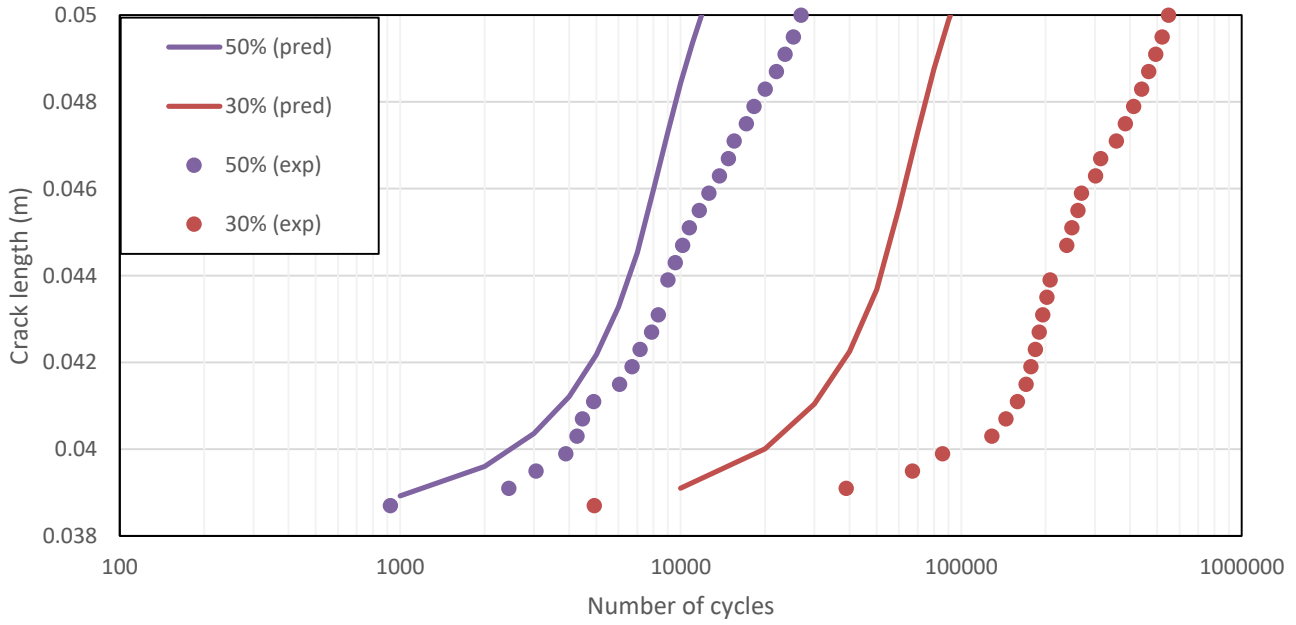

Figure 4-32 Crack growth curves for IM7/977-3 loaded at R_d=0.5 under constant amplitude fatigue compared to predictions using Equation 4.9

The prediction model shows consistently high inaccuracies for failures occurring $N \leq 3000$ cycles, as the tested fatigue spectra is intended to cause failure after many days (due to possessing many low damaging cycles) this isn't a regime where accuracy is crucial. Accuracy beyond $N = 3000$ cycles is reasonable with predictions for negative R_d values demonstrating more reliability than the positive. Due to the relative lack of experimental data for positive R_d values (more particularly values closer to 0.5) it was expected that the prediction curves for $R_d = 0.5$ would be largely inaccurate. Despite this, the predictions being conservative does assist in reducing the likelihood of unintended damage removal when spectrum reduction is being performed. As such the overly conservative behaviour observed in Figures 4.29 & 4.32 was expected to cause failure predictions under variable amplitude loading to also be premature.

The reason for the majority of the discrepancy between the experimental and prediction curves can be observed in Figure 4.28, the best fit curve is representing data sets which are either steeper or shallower (some more notably then others) than it. However, as parts of single tests are commonly both shallower and steeper than the curve, the integration process sees this behaviour "averaging out" meaning the failure points of the prediction are regularly close to the cycle count at experimental failure. Through implementation of MATLAB script the Block Sequences were used for failure prediction with the CRGM. Crack growth for each cycle within each block was individually calculated with the crack length plotted at the end of each block (Figures 4.33-4.36).

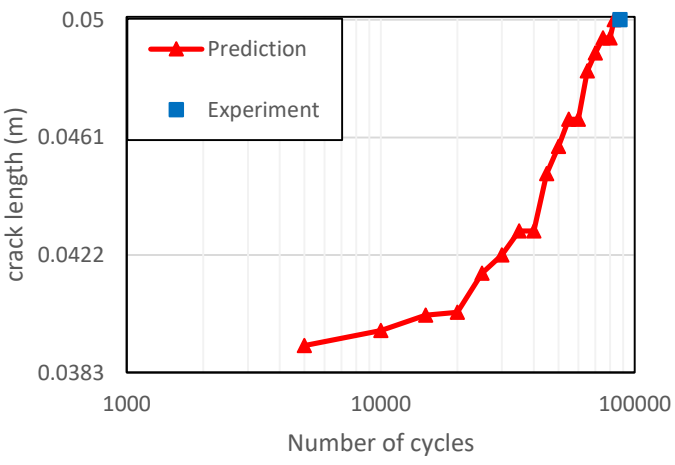

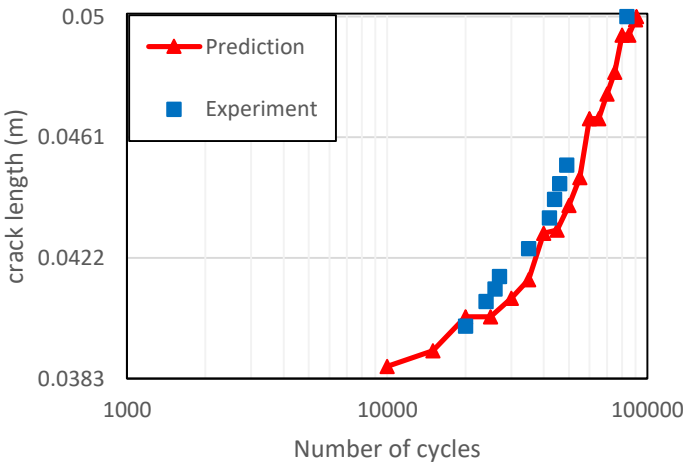

Figure 4-33 Crack growth curves for IM7/977-3 loaded with Block Sequence A compared to predictions using Equation 4.9 (L-H left, H-L, right)

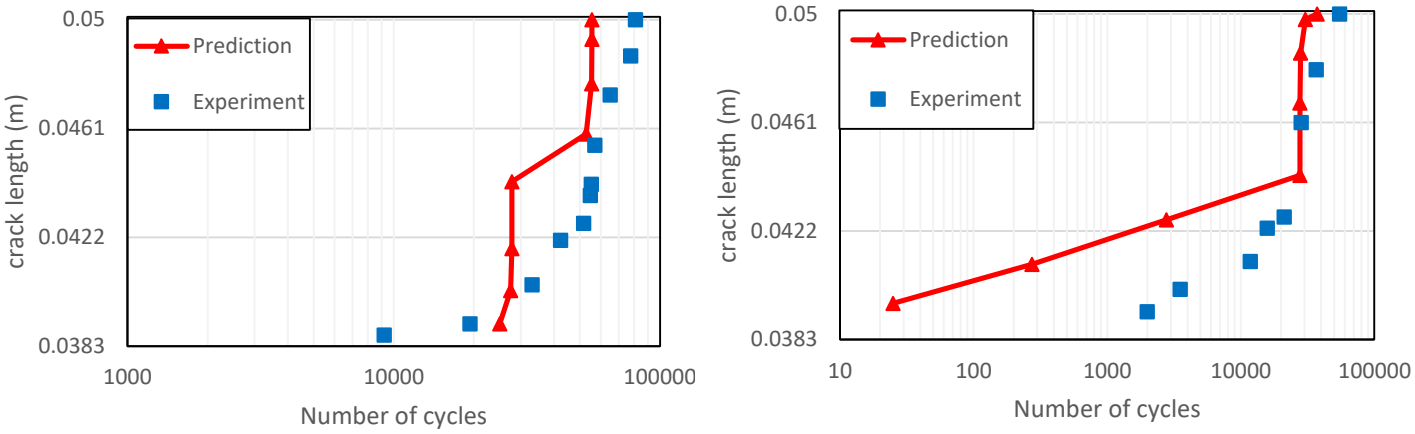

Figure 4-34 Crack growth curves for IM7/977-3 loaded with Block Sequence B compared to predictions using Equation 4.9 (L-H left, H-L, right)

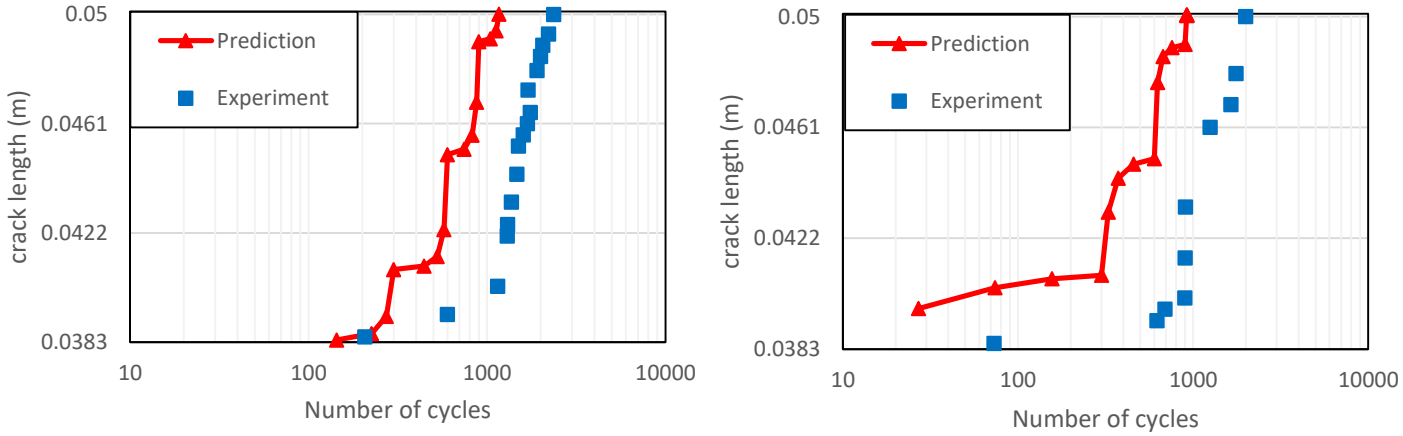

Figure 4-35 Crack growth curves for IM7/977-3 loaded with Block Sequence C compared to predictions using Equation 4.9 (L-H left, H-L, right)

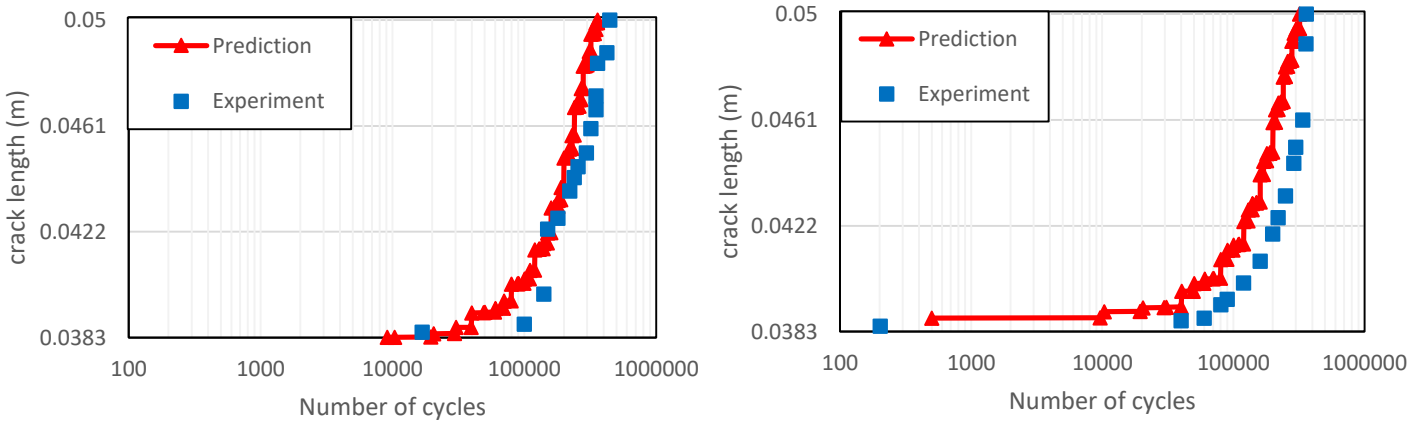

Figure 4-36 Crack growth curves for IM7/977-3 loaded with Block Sequence D compared to predictions using Equation 4.9 (L-H left, H-L, right)

The crack growth behaviour exhibited experimentally is generally reproduced through the CGRM. Block Sequence D most closely represents the growth curve of a constant amplitude test as both experimental and prediction curves are relatively smooth, this is due to the consistently low damage dealt by each block. The other cases (more notably C) demonstrate that each block has a different damage content which is reflected in the crack propagating at different rates throughout each pass.

Similarly to the RSM results, the CGRM failure predictions were tabulated with the pass counts calculated to enable a more representative comparison.

Table 4-10 Comparison of the cycle count at failure for experimental fatigue tests based on the low-high and high-low block sequence tests; crack growth rate model (CGRM). The numbers in the brackets are the pass counts, each block is considered to be 0.25 passes for Sequences A, B and C and 0.125 for Sequence D

	Block Sequence A		**Block Sequence B**		**Block Sequence C**		**Block Sequence D**	
	LH	**HL**	**LH**	**HL**	**LH**	**HL**	**LH**	**HL**
Experiment	87,492 (4.37)	83,366 (4.16)	80,787 (2.27)	54,997 (1.99)	2,362 (7.69)	1,993 (6.81)	445,329 (11.15)	360,112 (9.06)
CGRM	90,957 (4.55)	82,917 (4.15)	55,538 (1.88)	37,333 (1.82)	1,171 (3.74)	921 (3.19)	359,602 (8.90)	320,498 (8.12)

The predicted pass counts in Table 4.10 are conservative for all but one case, furthermore results for Block Sequence A are the most accurate with the H-L and L-H sequences within 0.01 and 0.18 passes of the experimental results respectively. Block Sequence D shows the highest variation between the H-L and L-H sequences which reflects the experimental behaviour, while Sequence B shows the smallest variation. Notably Block Sequence C is highly inaccurate with the pass counts approximately half of the experimental counts, this aligns with the constant

amplitude findings in Figures 4.29-4.32 as the highly damaging cycles showed significant inaccuracy. All L-H predictions are larger than the corresponding H-L predictions which is representative of the experimental failure results. With the exception of Block Sequence C, all predicted pass counts are within 20% of the experimental pass counts. Due to the large range of R_d values and loading parameters tested in the Block Sequences the general accuracy is sufficient to justify using the crack growth rate modelling for spectrum reduction, with the intention of tailoring the tested sequence to loading parameters which were best represented.

4.5 Chapter Summary

Static testing and analysis conducted using the ASTM D7905 was completed, enabling the determination of G_{IIc} which provided a measure for designing subsequent fatigue tests. The constant amplitude fatigue testing resulted in the construction of four S-N curves for R_d values: -1, -0.1, 0.1 and 0.5. Through block loading testing the presence of sequence effects was observed for the IM7/977-3 specimens, indicating they needed to be accounted for when developing prediction models. Combining the constant amplitude fatigue data and the block loading data two models were analytically fit to enable fatigue life predictions: a residual strength model and a crack growth rate model. Both models produced conservative predictions for the vast majority of loading conditions, showing good agreement with the experimental pass counts. As both models display consistency and a sufficient level of accuracy they are appropriate for implementation when performing spectrum reduction.

Being capable of calculating the crack length at any given cycle in a test, the crack growth rate model is preferable to the RSM when considering the process of spectrum reduction.

End of Chapter 4

Chapter 5

Performing Spectra Reduction and an Extension of the Fatigue Simplification Methodology to M18/1/G939 Specimens

5.1 Introduction

Having developed models capable of attributing damage to cycles within a fatigue spectrum, this chapter will detail the application of two spectrum reduction techniques; truncation and cycle merging. Following testing under a scaled version of FALSTAFF, several adjustments were performed to align the spectrum more with the constant amplitude loading conditions previously conducted to improve the accuracy of the implemented modelling and therefore encourage conservative reductions. This chapter will begin by detailing the extension of the previously described methodology to M18/1/G939 specimens. Static testing was displayed earlier in Section 4.3.1 and was utilised to design a series of constant amplitude fatigue tests. Crack growth modelling was subsequently implemented to not only compare with experimental tests, but also to assist with performing spectrum truncation and cycle merging.

5.2 Experimental Procedure

Fatigue tests were conducted using the setup and execution procedure detailed in Section 3.3 Fatigue Testing.

5.3 Crack Growth Modelling of M18/G939

To generate the crack growth rate model described in Section 4.4.2, a data set must first be collected from conducting a series of constant amplitude fatigue tests. After which the analytical modelling was performed with the assistance of FEA to scale G_{II} to improve the data fitting.

5.3.1 Constant Amplitude Fatigue Testing

A series of constant amplitude fatigue tests were conducted for the woven specimen in the same manner detailed in Chapter 4. Much like Table 4.5, Table 5.1 was constructed by rearranging Equation 4.4 for P_{max} in terms of G_{IIc} to then determine the displacement limits using the results from compliance calibration conducted in Section 3.4.1.

Table 5-1 Average maximum load and displacement limits for constant amplitude fatigue test for M18/1/G939 specimens

	G_{II}	P (N)	$P/P_{load\ drop}$ (%)	Disp (mm)
10%	132.82	246.76	31.62	1.221
20%	265.64	348.97	44.72	1.726
30%	398.46	427.40	54.77	2.114
40%	531.28	493.52	63.25	2.441
50%	664.10	551.77	70.71	2.729
60%	796.92	604.43	77.46	2.990
70%	929.74	652.86	83.67	3.230
80%	1062.56	697.94	89.44	3.453
90%	1195.38	740.27	94.87	3.662
100%	1328.20	780.32	100	3.860

The same four R_d values tested for the unidirectional specimen were chosen for the woven specimens (-1, -0.1, 0.1 and 0.5). The test limits were chosen such that the risk of static failure and excessively long tests were low. As detailed in Chapter 4, specimens were considered to have failed once the crack propagated to the centre load nose (11.7mm of crack growth). The crack growth data is displayed in Figures 5.1 to 5.4.

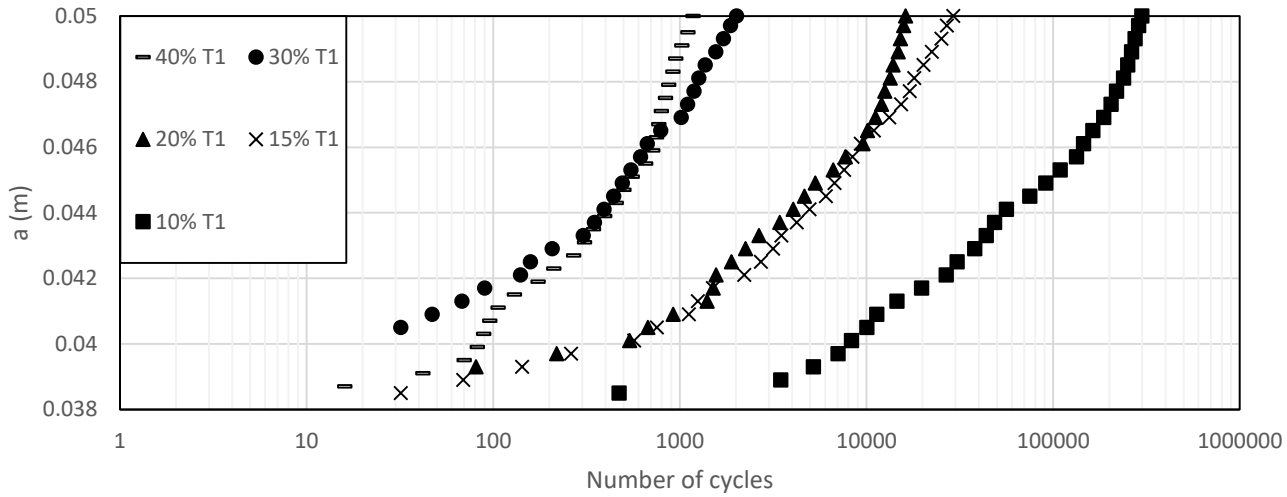

Figure 5-1 Crack growth data for M18/1/G939 loaded with R_d=-1 constant amplitude displacement controlled fatigue tests

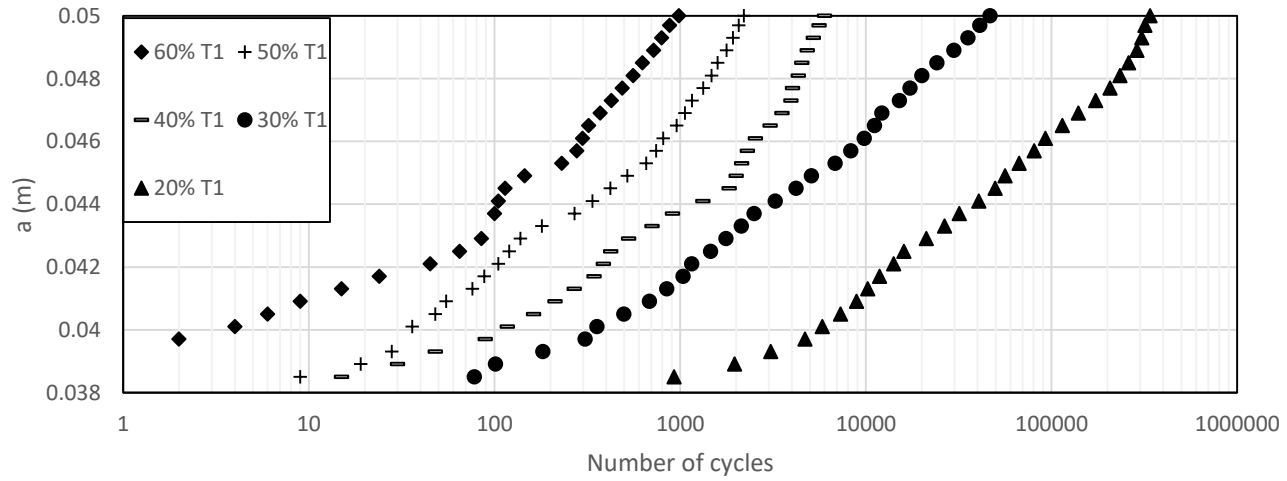

Figure 5-2 Crack growth data for M18/1/G939 loaded with R_d=-0.1 constant amplitude displacement controlled fatigue tests

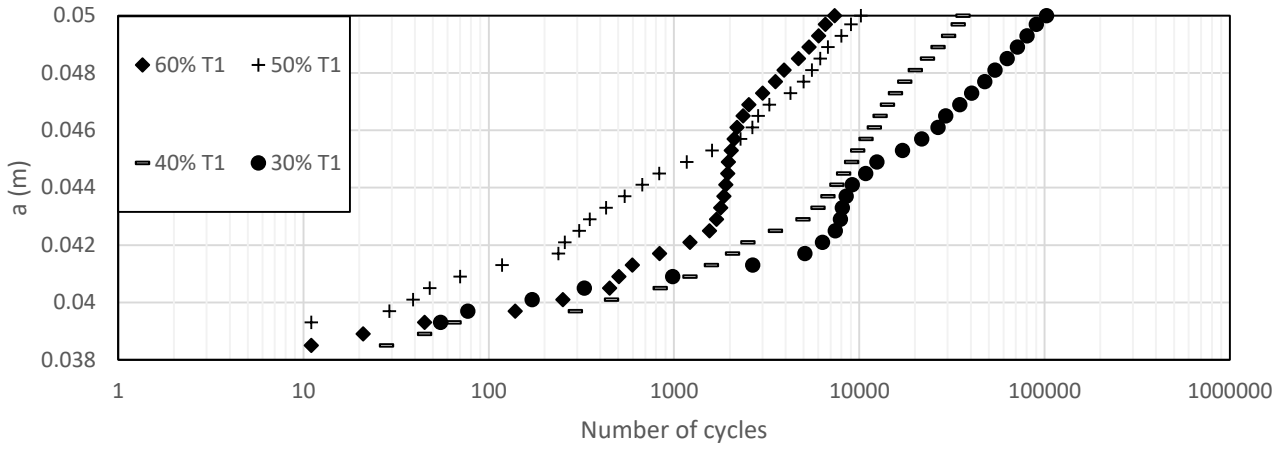

Figure 5-3 Crack growth data for M18/1/G939 loaded with R_d=0.1 constant amplitude displacement controlled fatigue tests

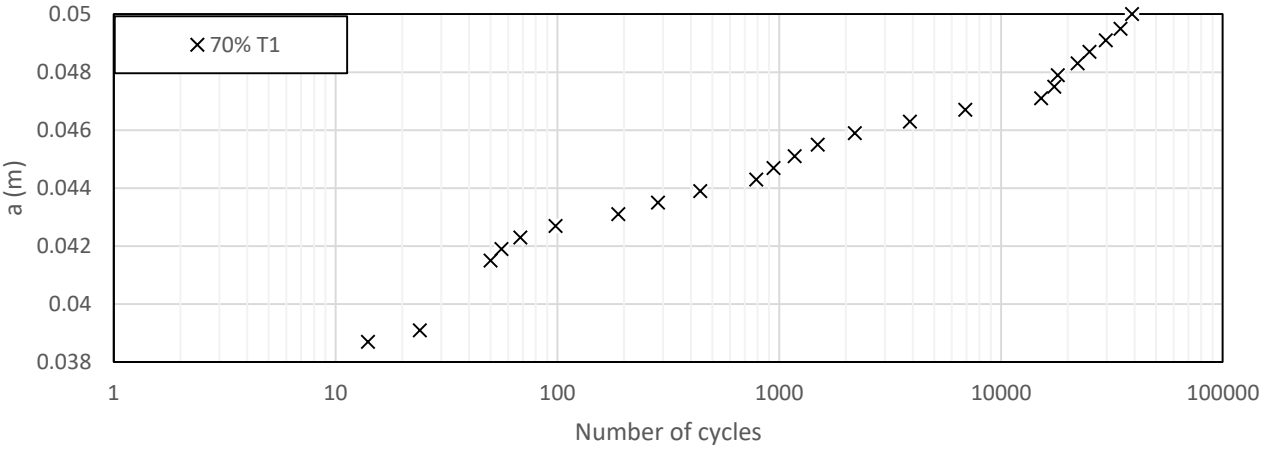

Figure 5-4 Crack growth data for M18/1/G939 loaded with R_d=0.5 constant amplitude displacement controlled fatigue tests

Comparing the crack growth data for the M18/1/G939 with the IM7/977-3 it is apparent that under the same $\%G_{IIc}$ loading (for the same R_d value), the woven specimens can endure more fatiguing by orders of magnitude. For example under loading conditions: $\%G_{IIc} = 40\%$, R=-1 the unidirectional specimen failed after ~80 cycles, while the woven specimen failed after ~6000 cycles. The failure points from each constant amplitude fatigue test were organised by their

corresponding R_d value and then plotted against the displacement level (r_d) to generate curves similar to S-N curves (Figure 5.5).

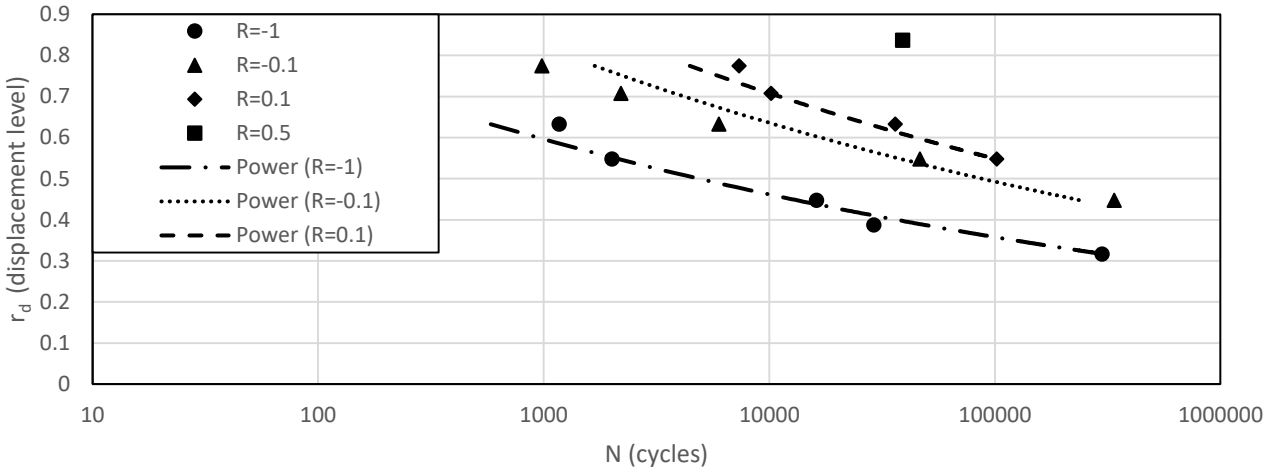

Figure 5-5 r_d-N curves for M18/1/G939 for R_d=-1, -0.1, 0.1 and 0.5 under displacement control

Similarly to the unidirectional specimens, no endurance limit was experimentally observed. Furthermore, due to the increased fatigue resistance of the woven specimens the test limits for high R_d values needed to be increased to ensure failure occurred within a reasonable time frame (generally <1,000,000 cycles). With the previously mentioned limits on accuracy which higher R_d values presented (see Section 4.3.2) combined with the need for more severe loading, testing for R=0.5 was halted to prevent unnecessary specimen loss (either due to overloading or excessively long testing).

5.3.2 Crack Growth Rate Modelling

Theoretical G_{II} values were calculated using Equation 4.5 for the woven specimens. These values were compared with J integral values acquired using ABAQUS modelling previously described in Section 4.3.1 which had found agreement with Equation 4.5 when implemented for the

unidirectional specimen. G_{II} was found to both decrease at a faster rate (as a function of crack length) but was also significantly larger in value for the woven specimen than values calculated from Equation 4.5.

To address this, an adjustment was made to G_{II} which scaled the theoretical values by using Equation 5.1 to achieve the values acquired from FEA. This also resulted in sufficient inclination of the crack growth rate curves to avoid substantial over/under estimations.

Table 5-2 Comparison of G_{II} values acquired from using Equation 4.5 and from FEA (J integral) under a loading of 2.1143mm. A scaling factor representing the ratio of the FEA and theoretical values is presented.

Crack length (m)	G_{II} **(Equation 3)**	G_{II} **(FEA)**	$\frac{G_{II}}{G_{II,initial}}$	**Scaling Factor**
0.0383	464.1	678.7	1	1.462
0.04	460.1	659.9	0.991	1.434
0.045	431.5	597.4	0.930	1.384
0.05	386.6	499.1	0.833	1.291

$$G_{II,adj} = \left(F_1 * \frac{G_{II}}{G_{II_{initial}}} + F_2\right) * G_{II} \qquad \text{Equation 5.1}$$

$G_{II_{initial}}$ is the value of G_{II} for the given loading conditions (δ_{max}, R_d) when the specimen is pristine (a=0.0383m), while F_1 and F_2 are constants with values of 0.9576 and 0.5024 respectively determined through linear fitting the data presented in Table 5.2.

Crack growth rate data was generated for the fatigue data presented in Figures 5.1-5.4 and is displayed in Figure 5.6.

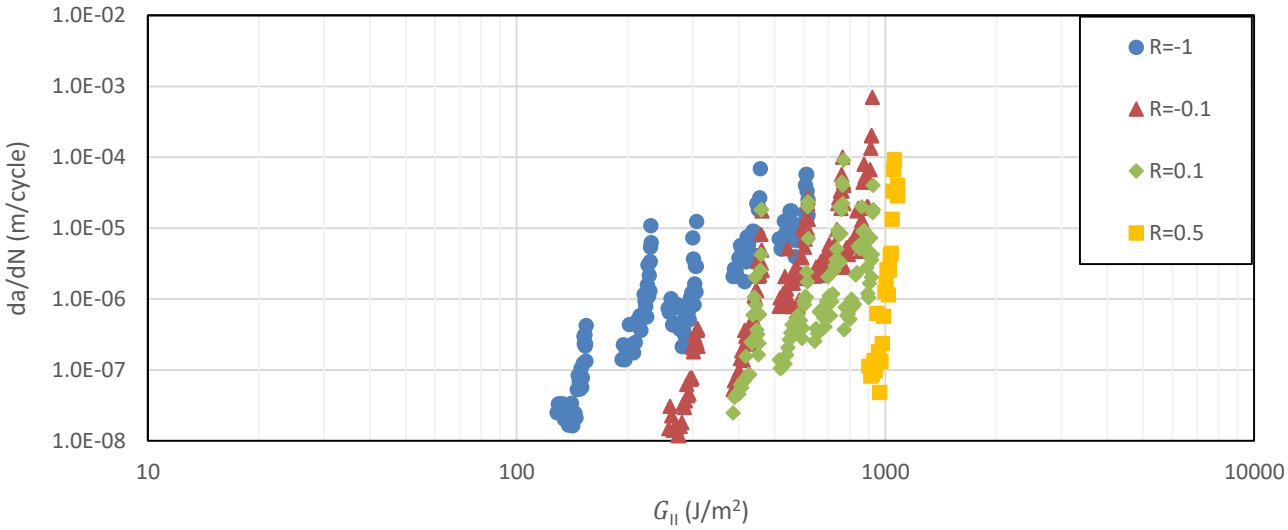

Figure 5-6 Crack growth rate data as a function of G_{II} for M18/1/G939 specimens using Equations 4.4

Through the application of Equation 4.8 (with $\mu_f = 0.55$) the crack growth data was collapsed onto a single curve in a similar manner to the unidirectional data. Notably, unlike the unidirectional crack growth behaviour (Figure 4.24), no initial slow growth was experimentally observed for the woven tests. As a result adjustments (Equation 4.7) weren't required to align initial crack growth data, however Equation 5.1 was implemented to scale G_{II} to 'match' FEA results. G_{eq} was plotted against da/dN in Figures 5.7.

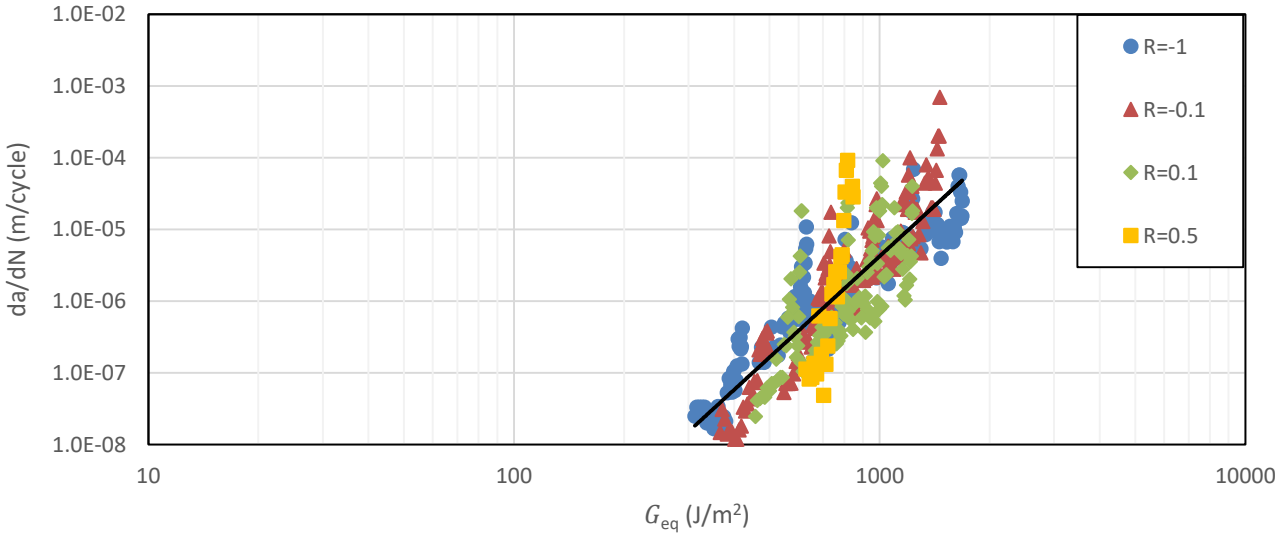

Figure 5-7 Crack growth rate data as a function of G_{eq} for M18/1/G939 specimens using Equations 4.8

Fitting Equation 4.9 using the data in Figure 5.7, D and m were determined to be $3.864 * 10^{-20}$ and 4.680 respectively. By integrating Equation 4.9 the constant amplitude fatigue experimental tests can be predicted for the purpose of comparison.

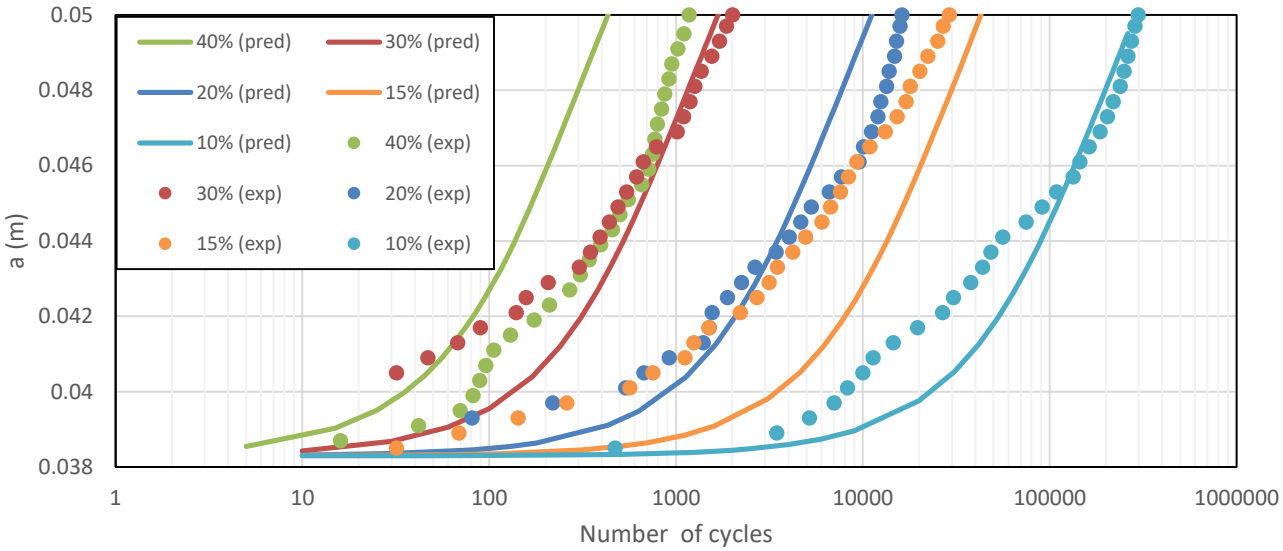

Figure 5-8 Crack growth curves for M18/1/G939 loaded at R_d=-1 under constant amplitude fatigue compared to predictions using Equation 4.9

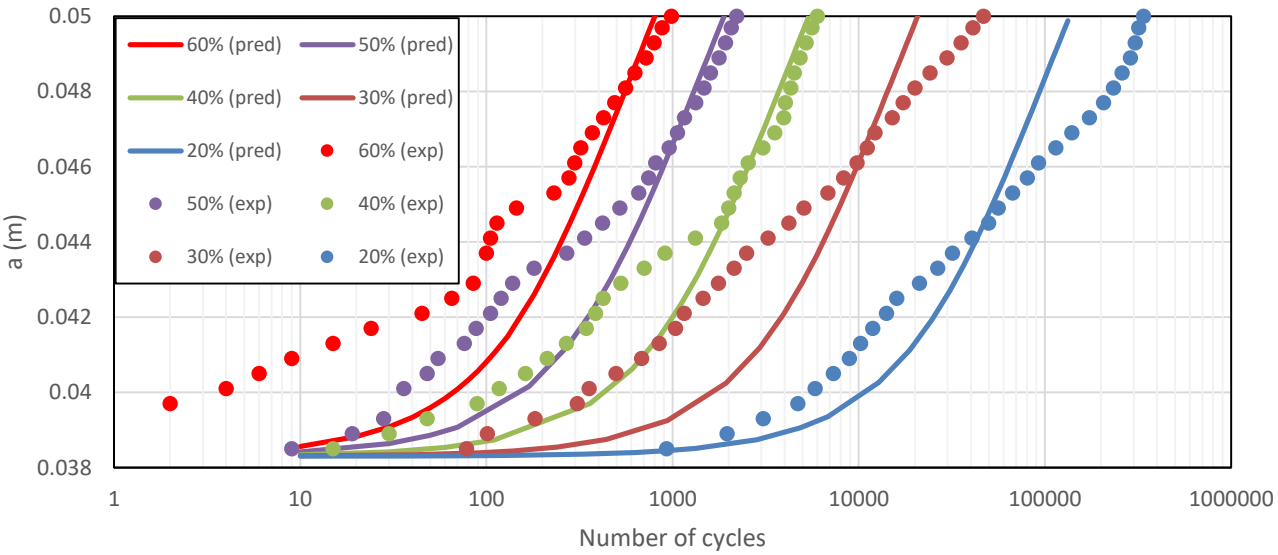

Figure 5-9 Crack growth curves for M18/1/G939 loaded at R_d=-0.1 under constant amplitude fatigue compared to predictions using Equation 4.9

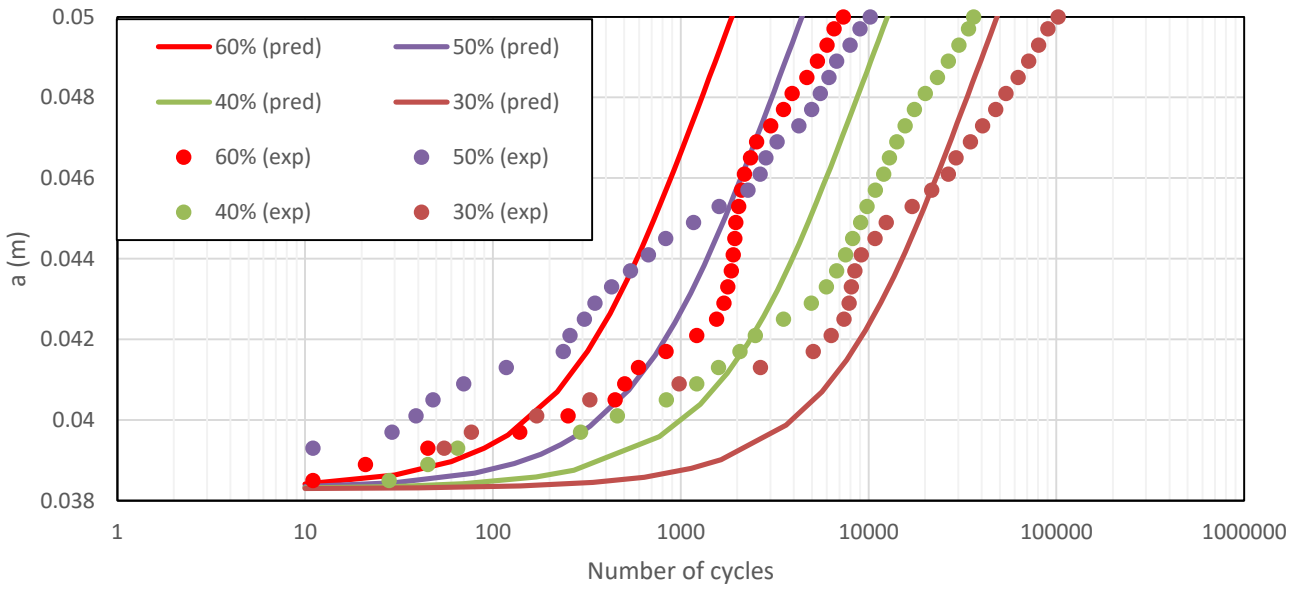

Figure 5-10 Crack growth curves for M18/1/G939 loaded at R_d=0.1 under constant amplitude fatigue compared to predictions using Equation 4.9

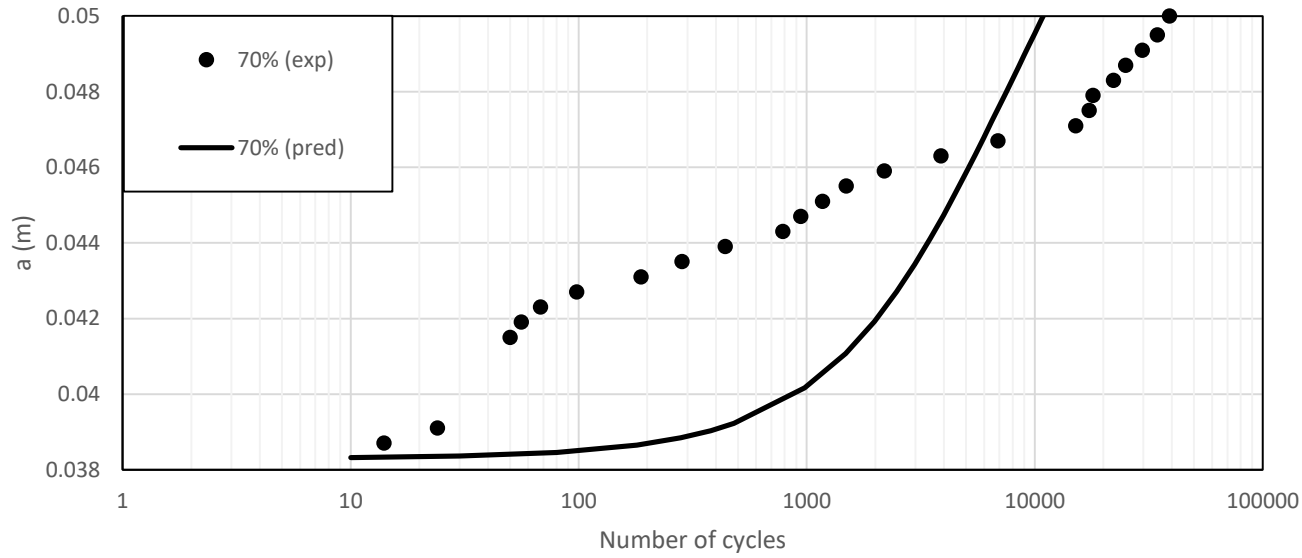

Figure 5-11 Crack growth curve for M18/1/G939 loaded at R_d=0.5 under constant amplitude fatigue compared to predictions using Equation 4.9

The CGRM predictions for the woven specimens under constant amplitude loading demonstrate notably higher accuracy then the unidirectional specimens, for both R_d=-1 and R_d=-0.1 this is most apparent. For R_d=0.1 and R_d=0.5 the prediction curves while conservative, do not resemble the crack growth behaviour exhibited experimentally (Figure 5.11 most clearly demonstrates this). The general improvement of the accuracy of the prediction curves can be attributed to the characteristics of the experimental data, most importantly the seeming lack of any short crack effects. Upon comparing Figure 5.7 with Figure 4.28, it is clear that individual tests in Figure 5.7 align with the fitting curve while only the bulk of data points (irrespective of test) align in Figure 4.28. Based off of the experimental crack growth rate data and the corresponding fitting curves, the crack propagation of woven specimens is characterised by the CGRM more so then the unidirectional specimens.

Having established the CGRM for M18/1/G939, both variable amplitude loading predictions and spectrum reduction techniques are implementable and will be discussed in Section 5.4.

5.3.3 Specimen Retesting

As the tested ENF specimens are sufficiently long such that overhang exceeds 11.7mm, the possibility for reusing specimens for subsequent experimental loading was investigated. By physically shifting specimens in the reversible three point test fixture the effective crack length can be adjusted to 38.3mm. To validate reuse, both numerical and experimental testing was performed, with the FEA model discussed in Chapter 3 being utilised.

The experimental loading was mimicked in ABAQUS through shifting the relative position of the specimen and the support/load rollers, the total crack length was also extended by 12.7mm to account for propagation during fatigue loading. Static loading was then simulated up to a displacement of 6mm with experimental testing subsequently performed for comparison (Figure 5.12).

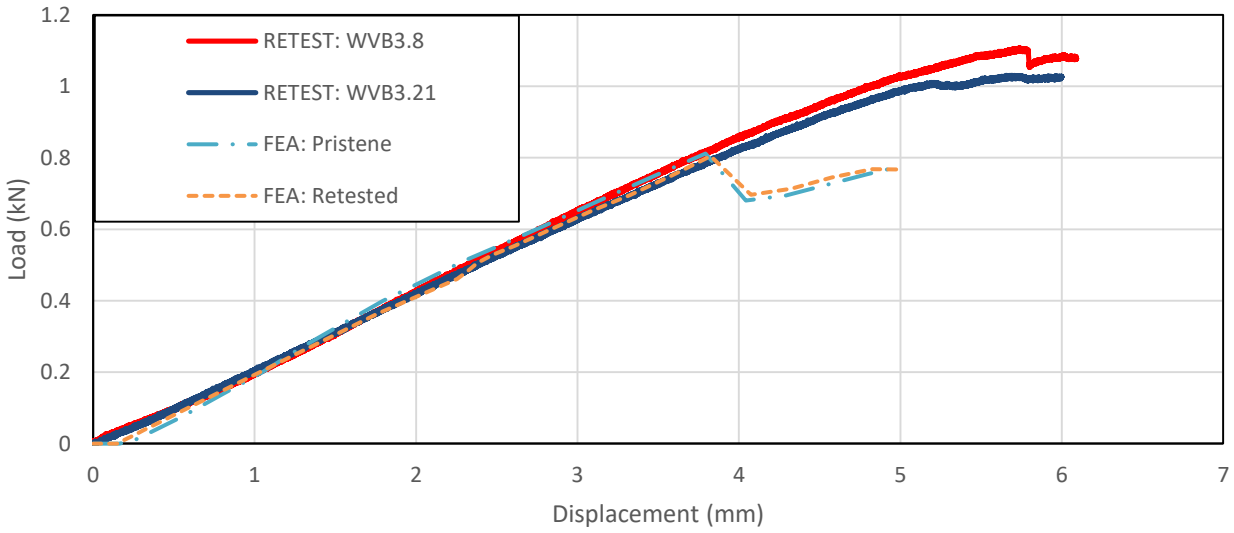

Figure 5-12 Comparison of both experimental and FEA static load/displacement data from testing of pristine specimens and retested specimens

The FEA indicates that the stiffness and displacement at which cracking occurs is similar for the pristine and retested specimens. However, while the experimental data does indicate that the stiffness of the specimens is largely the same, the failure point has been extended by 1.5-2mm.

Constant amplitude fatigue loading was conducted on previously tested specimens for R_d=-1. Specimens were selected such that the loading conditions corresponded to those which were experienced in a pristine condition. The failure points from the retests were plotted alongside the R_d=-1 r_d-N curve presented in Figure 5.5 for comparison (Figure 5.13).

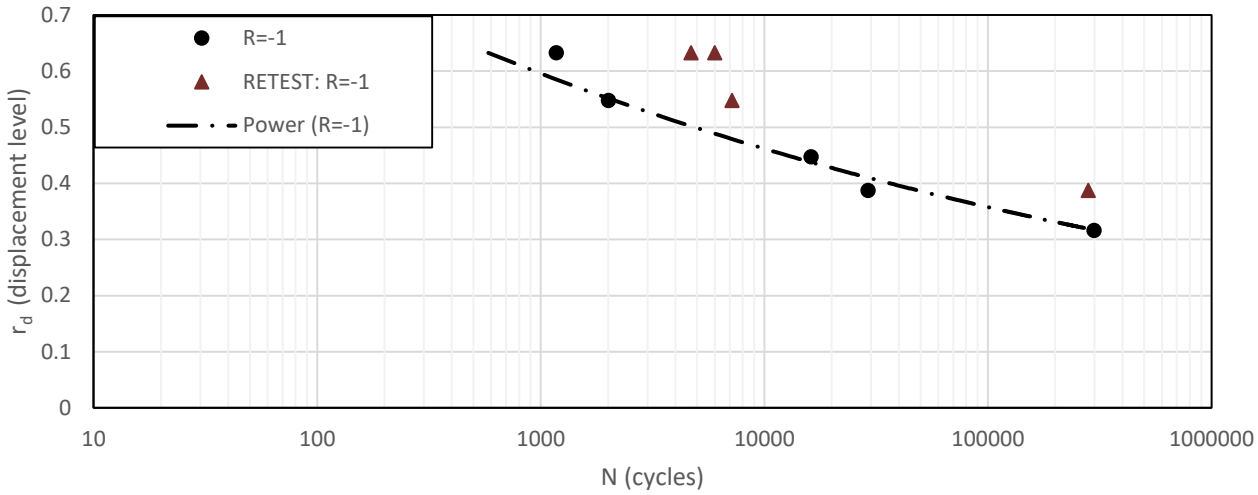

Figure 5-13 Comparison of experimental r_d-N data for M18/1/G939 from the testing of pristine specimens and retested specimens

Figure 5.13 demonstrates that the retests have a substantially longer fatigue life than the pristine condition tests. While experimental scatter is a reality of composite fatigue testing, there is approximately an order of magnitude of difference between the retests and pristine tests indicating the loading/specimen conditions aren't equivalent. When also considering the static results displayed in Figure 5.13, it is likely that the region at (and possibly beyond) the crack tip differ notably between tested and untested specimens. Due to the consistency of the material stiffness between test configurations, the same effective crack length was achieved for both test setups. The point at which static failure occurs (crack propagation) in Figure 5.12 and the failure points in Figure 5.13 indicate that the fatigue resistance of the tested specimens may have been strengthened.

Due to the significant difference between the two test configurations, specimens in this study weren't retested outside of the tests conducted in this section.

5.4 Variable Amplitude Fatigue Spectrum

This section will first detail the variable amplitude spectrum which will be the subject of spectrum reduction. The independent application of truncation and cycle merging will then be investigated with a comparison being made between predictions and experimental findings.

5.4.1 Original FALSTAFF Spectrum

For this study, the variable amplitude fatigue spectrum which was the subject of reduction was an adjusted version of The Fighter Aircraft Loading Standard for Fatigue (FALSTAFF). FALSTAFF is a standardised wing root area manoeuvre dominated spectrum, which is comprised of 35,966 turning points with 32 different load levels, representing 200 flights [124].

The normalised FALSTAFF sequence was initially scaled to achieve a peak displacement of 1.18mm for fatigue testing.

The vast majority of cycles within the sequence have a positive R_d ratio and a maximum displacement less than 0.5mm. Hence most cycles within this FALSTAFF sequence reside outside of the experimental test range of constant amplitude fatigue tests (see Chapter 4).

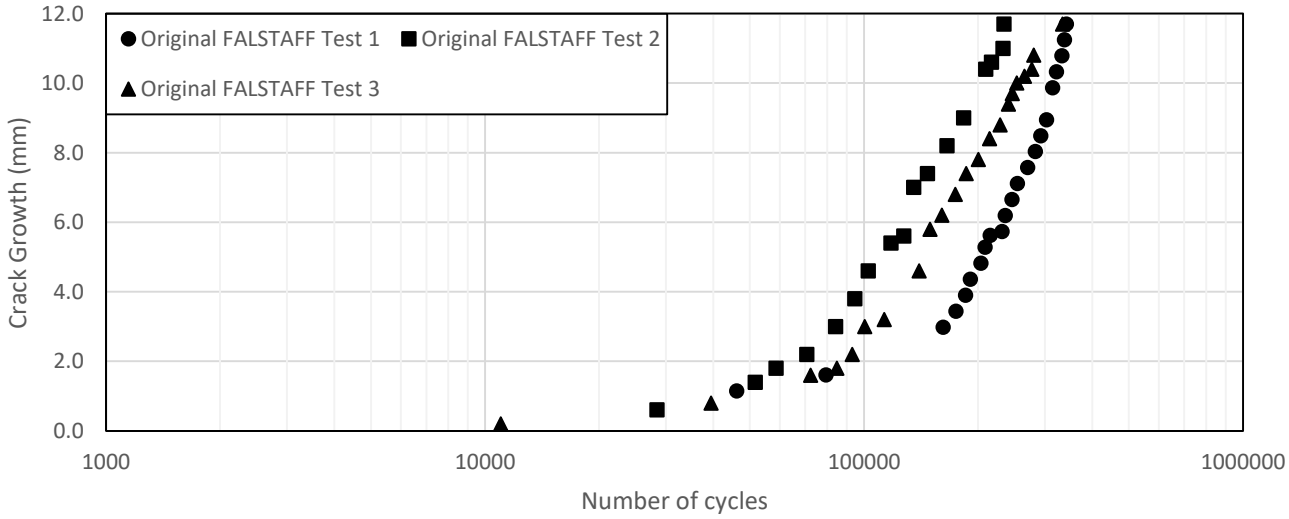

Figure 5-14 Crack growth curves of IM7/977-3 unidirectional specimens under the scaled FALSTAFF loading spectrum

A total of three complete variable amplitude fatigue tests were conducted using IM7/977-3 specimens. Failure occurred after an average of 16 passes of the FALSTAFF spectrum as depicted in Figure 5.14. The tests had a notably high variance with failure occurring over the range of ~200,000 to ~340,000 cycles (11-19 passes), where FALSTAFF is comprised of 17,983 cycles per pass. The test failed at the following points: Test 1 – 19 passes, Test 2 – 13 passes, Test 3 – 18.6 passes.

Basic truncation of FALSTAFF was performed using the Walker-Miner prediction model (Chapter 4). Two compressed sequences were created; one where all remaining cycles have fatigue lives of $5 * 10^8$ cycles or more, and one where all remaining cycles have fatigue lives of $1 * 10^6$ cycles or more.

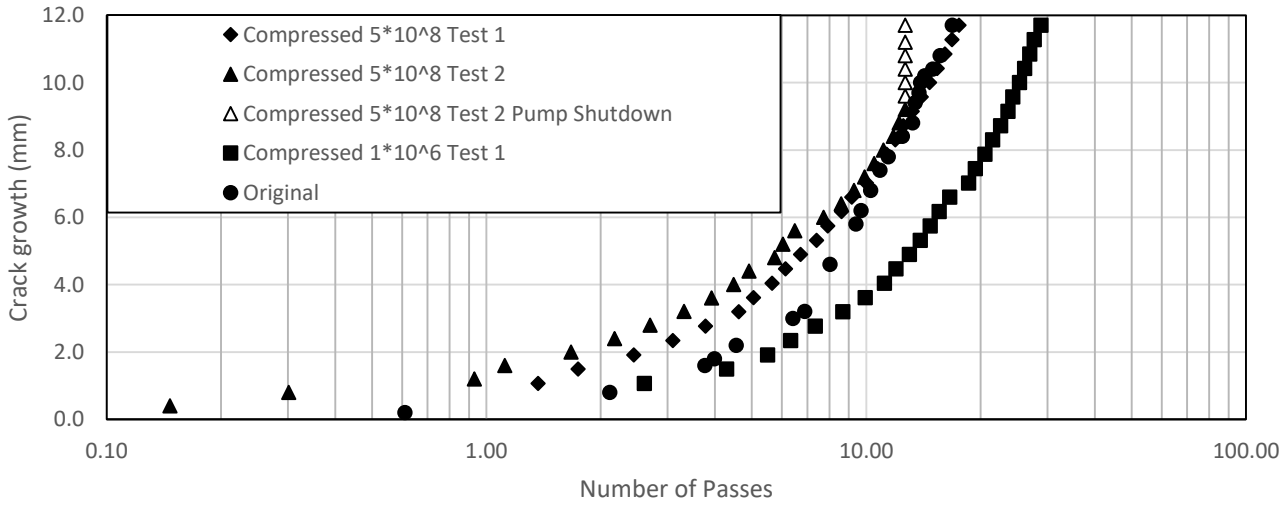

Figure 5-15 Crack growth curves of IM7-977-3 unidirectional specimens under truncated FALSTAFF loading spectrums using Walker-Miner predictions

Two tests were conducted with a set fatigue life of $5 * 10^8$cycles as the non-damaging criterion (load truncation level of 18.3%). The number of cycles removed was approximately 28% of the original sequence. The pass count resided within the range of the uncompressed spectrum tests, with failure occurring at ~17.6 passes (Figure 5.15). One of the tests (Compressed 500 mil Test

2) failed prematurely due to a pump shutdown, hence instantaneous growth from ~8.5mm to 11.7mm is depicted.

One experimental fatigue test was conducted based on the compressed spectrum with a fatigue life set to 1,000,000 cycles. Failure now occurred after ~29 passes of the compressed FALSTAFF spectrum (Figure 5.3). This is significantly larger than the 16 passes achieved for the original spectrum. Thus the inaccuracies associated with the Walker-Miner approach has resulted in some 'damaging' cycles to be deemed 'non-damaging' thus resulting in a non-conservative truncation. The test data depicted above can be used for development and validation for spectrum simplification and life prediction methods. The above results also indicated that eliminating "non-damaging" cycles is limited by the number of cycles which can be omitted. For further condensation of the loading spectrum another approach of cycle merging must be adopted.

To address the poor accuracy of the Walker-Miner approach and the excessive removal of damaging cycles, additional damage prediction models were implemented (see Chapter 4). Furthermore the FALSTAFF sequence was adjusted to ensure that the majority of cycles within the sequence reside within the experimental test range.

5.4.2 Adjusted FALSTAFF Spectrum

Adjustments were made to the FALSTAFF sequence to align the loading cycles more closely with the previously conducted experimental testing while retaining the majority of the turning points from the original sequence.

To maximise the use of available data obtained during the constant amplitude fatigue tests covering a range of R stress ratios (Section 2.3), the following adjustments were applied to the normalised FALSTAFF sequence.

1. The mean value of the sequence adjusted to ~0 (for example, replicates local build up stresses)

2. Scaled the sequence to achieve a peak displacement of 1.48mm
3. Finally clipping the highest peak such that the maximum peak displacement is 1.3mm

The maximum displacement peak of the adjusted FALSTAFF sequence was ~1.3mm (3.0mm for woven specimen), this was to ensure the risk of static failure (or non-fatigue failure) was very low. This was supported by the constant amplitude fatigue tests that were conducted where the maximum displacement 1.3mm did not cause premature failure due to overload.

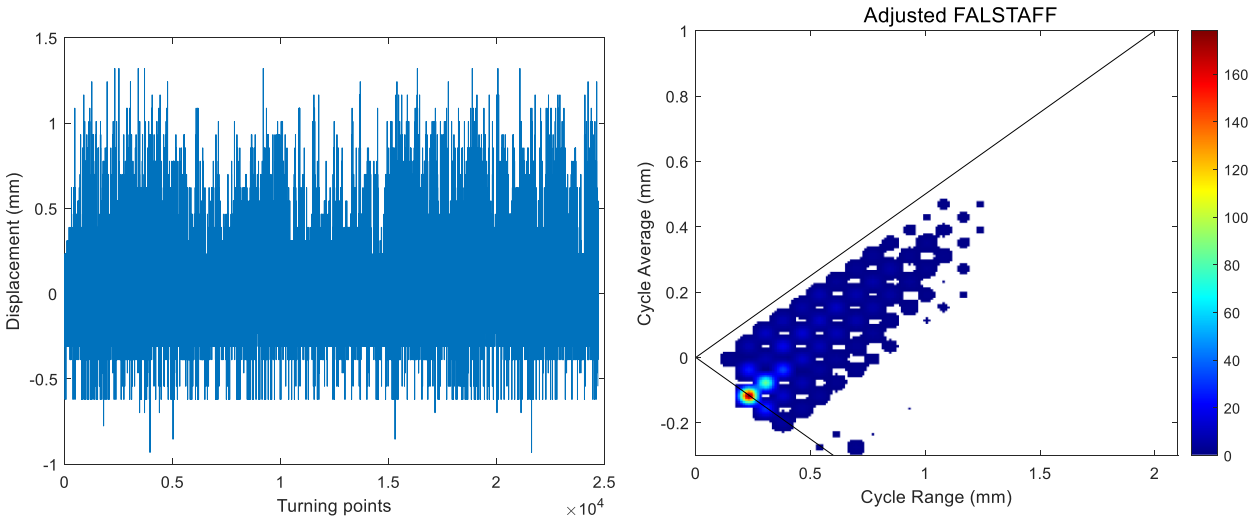

(a) *(b)*

Figure 5-16 (a) Adjusted FALSTAFF sequence after clipping, scaling and shifting,(b)Rainflow counting of adjusted FALSTAFF sequence. The diagonal lines on the histogram represents R_d=0 cycles, above the top line and below the bottom line are R_d>0 cycles

The newly adjusted sequence and its corresponding rainflow counted histogram is displayed in Figure 5.16. The crack growth rate model (CGRM) was then implemented to predict failure under the adjusted sequence.

The uncompressed FALSTAFF sequence used to load the woven specimens possessed a large number of cycles which resided outside the experimental test range (~3.25% G_{IIc}, fatigue lives of 10s of millions of cycles). To address this issue, cycles with magnitudes less than the experimental

test range were scaled (by a constant value) with the FALSTAFF sequence predictions used as a guide.

5.4.3 Truncation - Unidirectional

Truncation of the adjusted FALSTAFF sequence was performed by omitting half cycles (two adjacent turning points within a load sequence) which didn't equal or exceed a crack growth rate threshold (applied for several values), the resulting sequences are detailed in Table 5.3.

Table 5-3 Truncation levels of the adjusted FALSTAFF sequence as a function of crack growth rate omission level

da/dN omission criteria (m/cycle)	**Half cycles remaining after filtering**	**Truncation (%)**	**Predicted pass count**	**Predicted difference in pass count (%)**
$0.5 * 10^{-6}$	214	99%	10.10	225%
$0.5 * 10^{-7}$	1,144	95%	4.58	47.5%
$0.5 * 10^{-8}$	2,851	88%	3.39	9.2%
$0.5 * 10^{-9}$	5,567	77%	3.11	0.4%
$0.5 * 10^{-10}$	8,395	66%	3.08	-0.6%
$0.5 * 10^{-11}$	14,799	40%	3.09	-0.4%
–	24,691	0%	3.10	0%

If a half cycle had a corresponding crack growth rate less than the selected value in the left most column in Table 5.3, then the points comprising the half cycle were marked for removal. However, as each turning point in the loading sequence contributes to two different half cycles, both half cycles must have a sufficiently low crack growth rate for the common turning point to be omitted. Otherwise, if only one of the half cycles satisfies this condition then the common turning point was retained. The crack growth rate attributed to each half cycle was calculated from predicted crack growth occurring during the first pass of the sequence. The methods for calculating the crack growth rate of each half cycle and the predicted pass count are discussed in detail in Chapter 4.

This process was carried out using a MATLAB script and the resultant sequence was checked to insure there were no intermediate points (e.g. For three consecutive points: -1.0 mm to 0.2 mm to 0.8 mm, 0.2 mm is the intermediate point while for -1.0 mm to 0.8 mm to 0.2 mm there is no intermediate point).

Similarly to the block loading cases described in Chapter 4, failure predictions under FALSTAFF loading were performed by using a MATLAB script in tandem with Equation 4.9. The original and reduced sequences were each tested numerous times and are displayed in Figures 5.17 and 5.18.

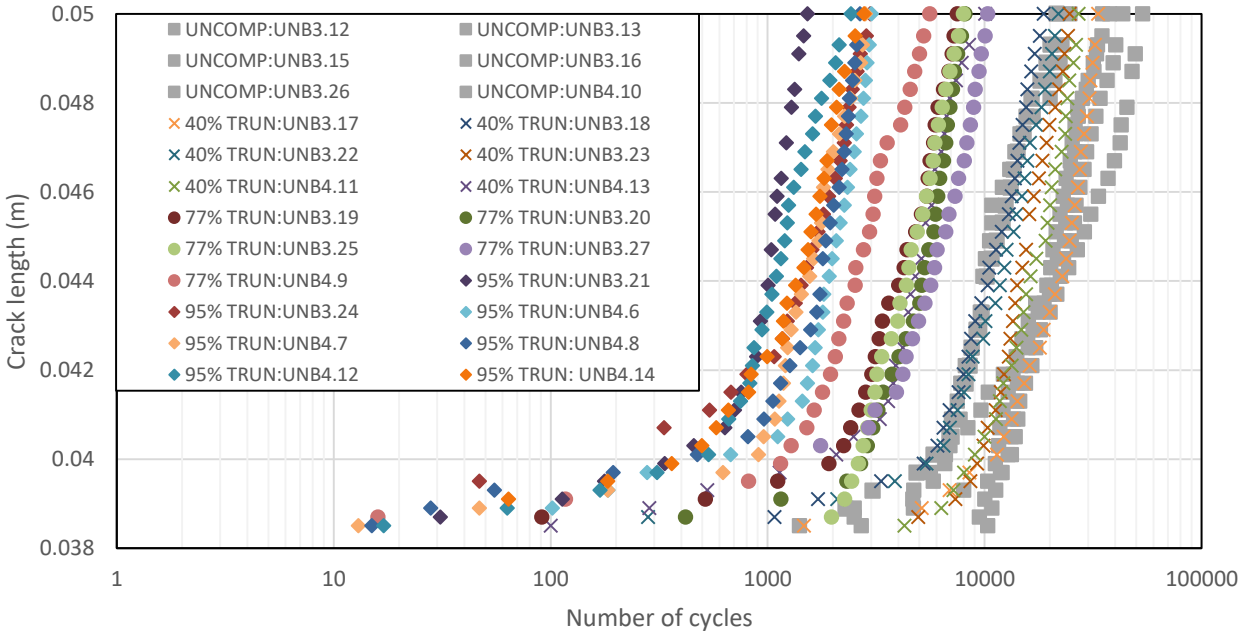

Figure 5-17 Crack growth data of unidirectional specimens loaded under an adjusted FALSTAFF sequence and several truncated variations in terms of cycle count. The uncompressed tests are depicted as UNCOMP, while the truncated tests are expressed as XX% TRUN, both followed by the specimen ID.

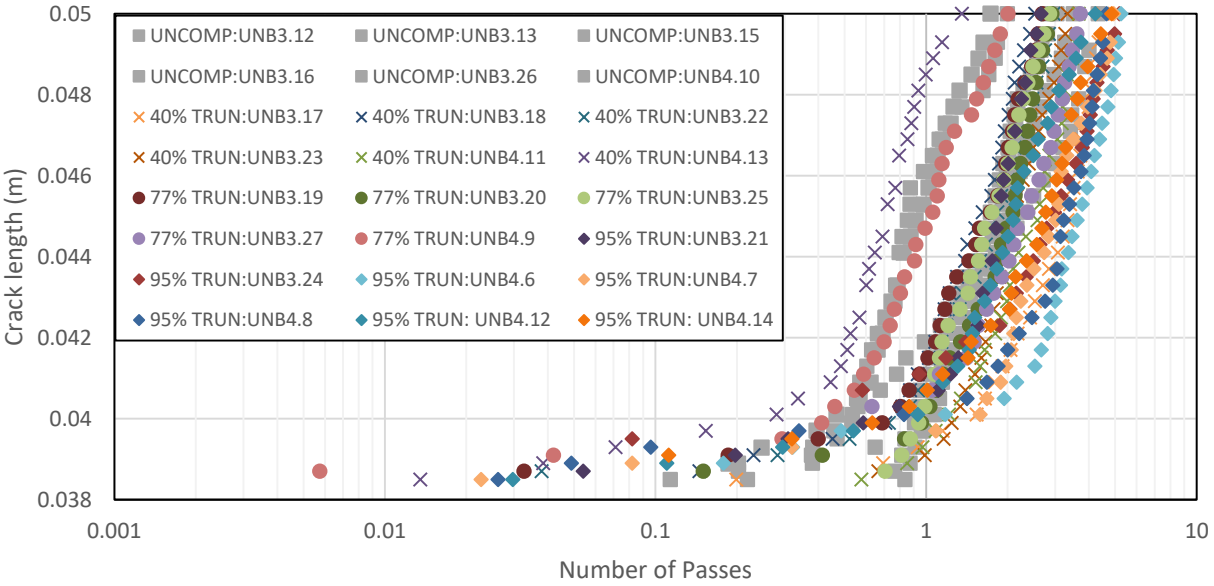

Figure 5-18 Crack growth data of unidirectional specimens loaded under an adjusted FALSTAFF sequence and several truncated variations in terms of pass count. The uncompressed tests are depicted as UNCOMP, while the truncated tests are expressed as XX% TRUN, both followed by the specimen ID.

Figure 5.17 demonstrates the significant decrease in the test times following truncation as tests last 1,000s of cycles rather than 10,000s, while Figure 5.18 shows that many of the compressed tests reside within the pass range of the original sequence. The predicted failure pass count of a specimen under each load sequence was calculated by first rainflow counting (using indexing) a given sequence and then applying Equations 4.7-4.9 to determine the crack growth contributed by each half and full cycle.

The statistics of the failure distributions have been tabulated in Table 5.4 to enable comparisons between different levels of truncations and its effect on the mean failure point, with the distribution of failure points displayed in Figure 5.19.

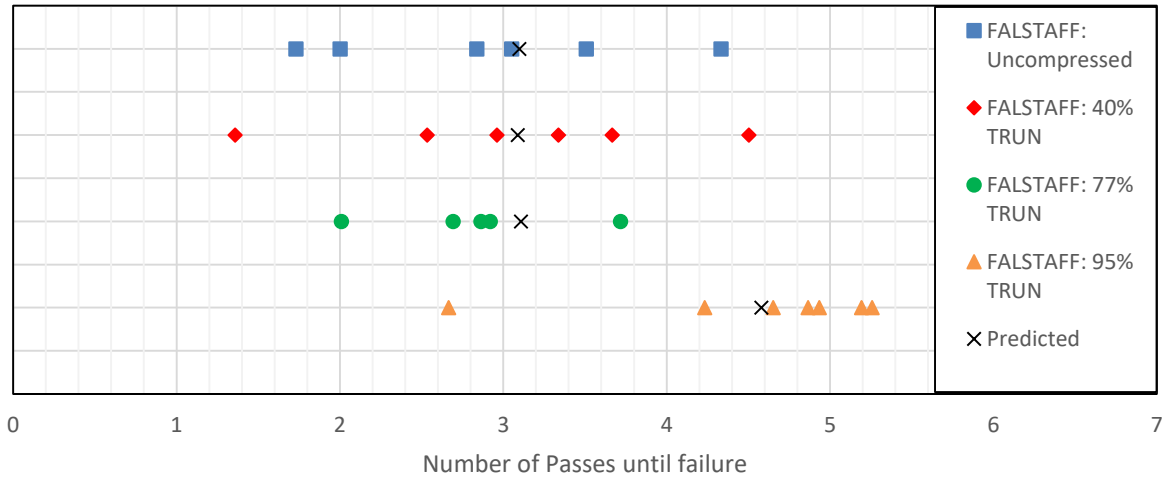

Figure 5-19 Distribution of failure points of each FALSTAFF fatigue loading test displayed in Figures 5.17 and 5.18 with a corresponding prediction for each set of tests. The vertical axis separates each set of tests.

Table 5-4 Statistics of unidirectional specimen failure under uncompressed and truncated FALSTAFF sequences

FALSTAFF sequence	Mean failure pass count (Log-Norm)	Prediction	B-Basis Value	95% CI (Log-Norm)
Uncompressed	2.945	3.100	1.389	[2.071, 3.818]
40% compressed	3.132	3.090	1.402	[1.657, 4.607]
77% compressed	2.856	3.110	1.789	[2.501, 3.211]
95% compressed	4.575	4.580	3.045	[3.678, 5.473]

The B-Basis values were calculated using a small sample size formula described in [125] indicating the threshold for 90% survivability with 95% confidence. These values would be useful to consider when implementing damage tolerance management to account for the scatter in the fatigue life of composite components.

The 40% and 77% truncated versions of the FALSTAFF sequence both resided within the original sequences test range which indicated that the shortened versions were somewhat representative of the original. The mean failure pass counts of the individual sequences were within 0.28 passes (within 10%) of each other and the 95% confidence intervals (CI) encompasses these values, with the exception of the 95% compressed sequence. Hence the difference between the 40% and 77% sequences is relatively low, implying that little damage was omitted/added, however the significant increase in the pass count for the 95% compressed sequence indicates the damage content was significantly decreased. A similar trend was found when comparing the B-Basis values for each data set, with the 95% compressed sequence having a B-base value at least 70% larger than the other three data sets. Furthermore, the analytical prediction of failure under each loading sequence was within 10% of the experimental mean (Log-Norm).

The implementation of indexed rainflow counting paired with Equations 4.7- 4.9 enabled these accurate failure predictions, however the predicted pass counts for the 40% and 66% compressed sequences show a negative percentage change from the original, indicating damage was added (Table 5.3). This behaviour can be attributed to the manner in which turning points were omitted during the truncation procedure. As described previously, each turning point contributes to the presence of two half cycles and upon the omission of a turning point new (potentially more damaging) half cycles can be generated. To account for this behaviour, rainflow counting before conducting truncation will result in all subsequently reduced sequences having equal or less damage than the original sequence. The author calculated the percentage change in pass count based on performing rainflow counting before truncation and found a negligible difference from the results provided in Table 5.3.

Therefore truncation levels of 40% and 77% have been achieved with only a small adjustment to the damage content occurring as a result.

5.4.4 Truncation – Woven

The same damage ranked truncation procedure was performed for the FALSTAFF sequence which loaded the woven specimens, with Table 5.5 depicting the degree of truncation corresponding to the omission criteria.

Table 5-5 Truncation levels of the adjusted FALSTAFF sequence for woven specimen as a function of crack growth rate omission level

da/dN omission criteria (m/cycle)	Half cycles remaining after filtering	Truncation (%)	Predicted pass count	Predicted difference in pass count (%)
$0.1 * 10^{-5}$	294	99%	18.23	306%
$0.8 * 10^{-7}$	1,266	95%	10.41	132%
$0.5 * 10^{-8}$	3,594	85%	6.24	39%
$0.5 * 10^{-9}$	6,392	74%	4.87	8%
$0.3 * 10^{-10}$	9,666	60%	4.66	4%
$0.3 * 10^{-11}$	14,970	40%	4.62	3%
–	24,691	0%	4.49	0%

If the acceptable amount of damage loss through truncation is taken as 5%, then the truncation limit resides between 60% and 74%. The adjusted FALSTAFF sequence and truncated variants were each tested several time and crack length data is displayed in Figures 5.20 and 5.21.

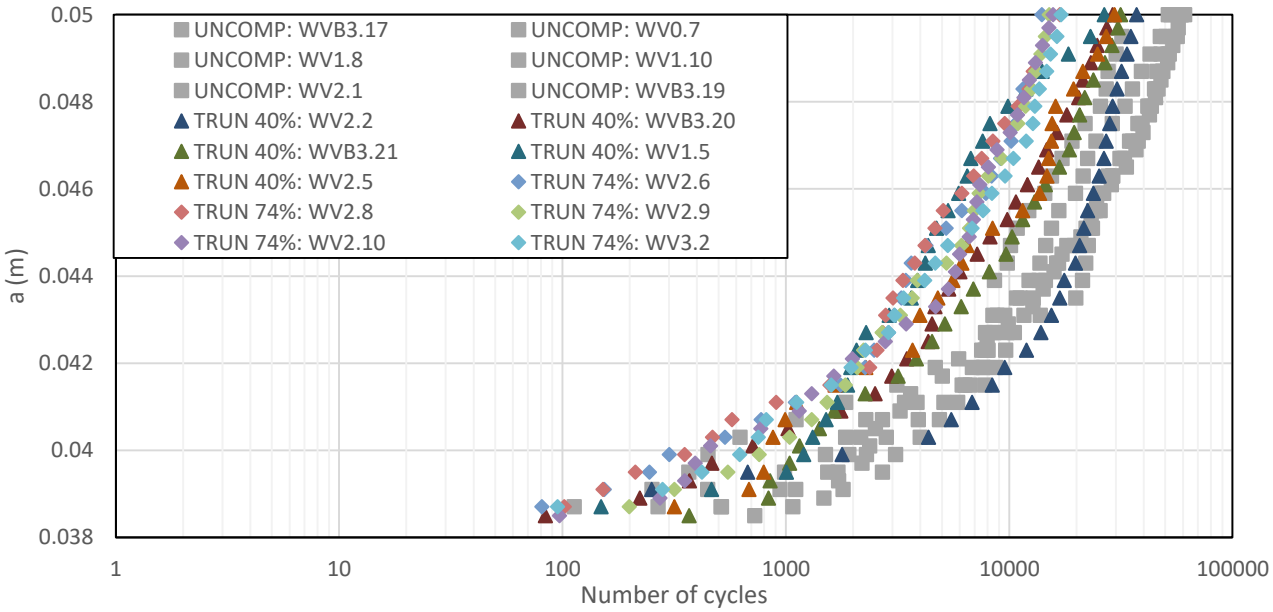

Figure 5-20 Crack growth curves of woven specimens loaded under an adjusted FALSTAFF spectrum and two truncated variations in terms of cycle count

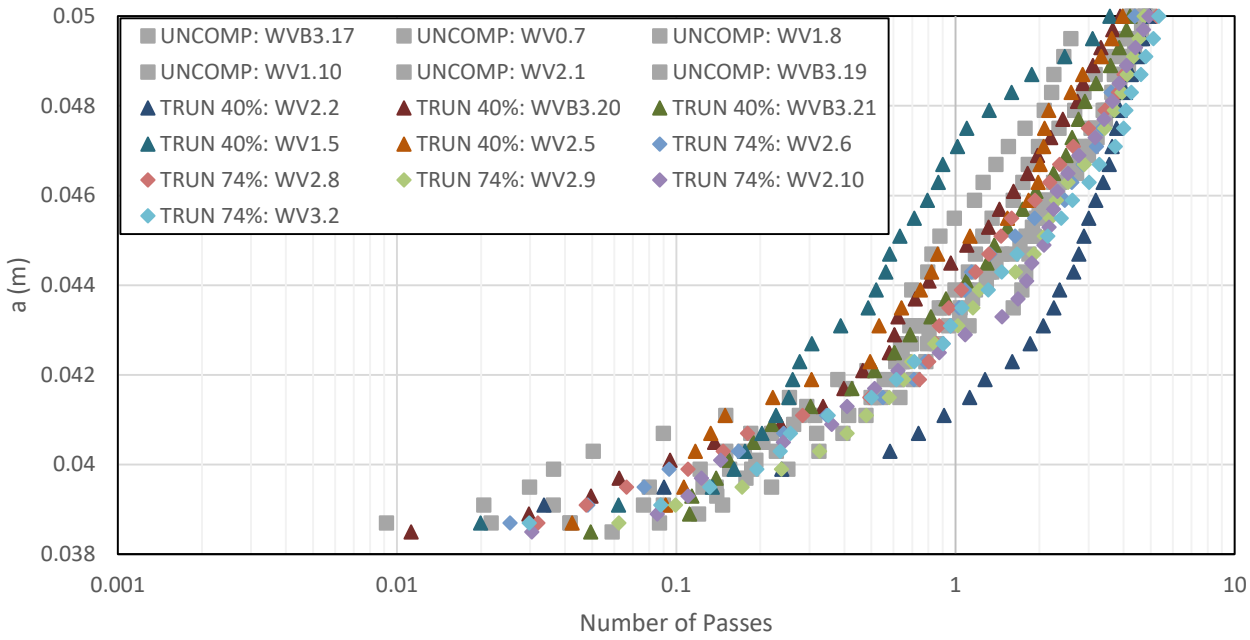

Figure 5-21 Crack growth curves of woven specimens loaded under an adjusted FALSTAFF spectrum and two truncated variations in terms of pass count

Figure 5.21 depicts most of the crack growth data from individual tests collapsing on each other, with the failure pass counts encompassing a brief range of values. As was performed in Chapter 5, predictions of failure under each load sequence were calculated. However, these notably under predicted the damage content of one sequence with the uncompressed, 40% truncated and 74% truncated sequences having failure counts after 4.487, 4.620 and 4.865 passes respectively. The trend of the predicted failure pass count increasing with the severity of truncation is consistent with the technique as turning points are only being removed from the original sequence hence the damage content should only decrease. Regardless, when comparing the distribution of failure points (Figure 5.22) the generated sequences evidently have similar damage content with the original due to significant overlap, indicating that the ranking of half cycles has sufficient accuracy to enable conservative truncation.

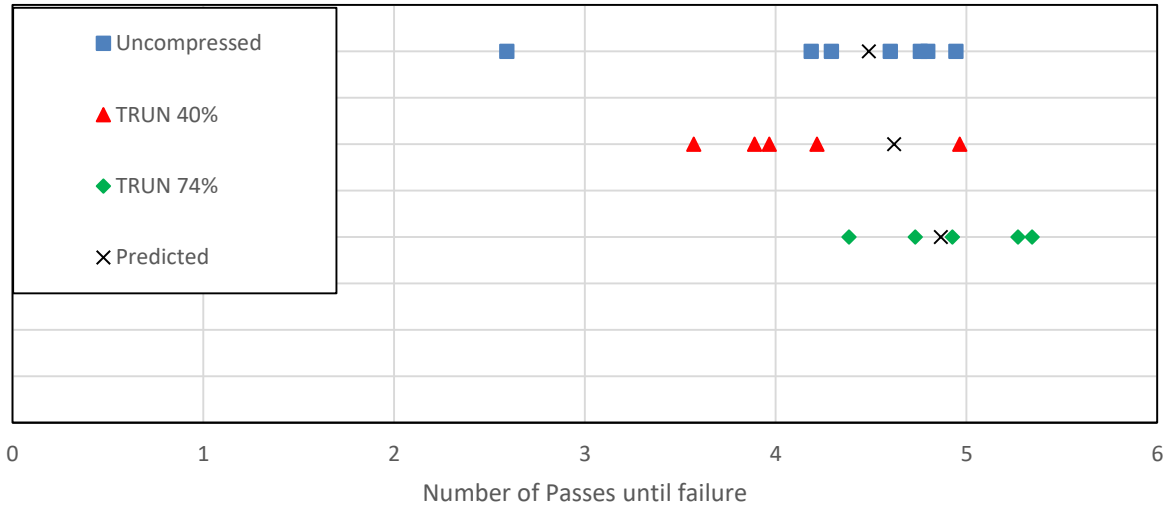

Figure 5-22 Distribution of failure points of each FALSTAFF fatigue loading test displayed in Figures 5.20 and 5.21 with a corresponding prediction for each set of tests

The failure distribution statistics for the uncompressed and truncated sequences are provided in Table 5.6.

Table 5-6 Statistics of woven specimen failure under uncompressed and truncated FALSTAFF sequences

FALSTAFF sequence	Mean failure pass count (Log-Norm)	Prediction	B -Basis Value	95% CI (Log-Norm)
Uncompressed	4.335	4.487	2.995	[3.616, 5.054]
40% compressed	4.127	4.620	3.286	[3.899, 4.354]
74% compressed	4.934	4.865	4.323	[4.793, 5.076]

The comparison of the 95% CI between sequences strongly indicates a decrease in fidelity through the application of truncation due to the notable decrease in the variance of data sets. However, as a single data point in the uncompressed data set is responsible for the sizable 95% CI, it is conducive to also consider the mean failure pass count and the scatter displayed in Figure 5.22. Overall the 40% compressed sequence has a somewhat larger damage content then the

uncompressed version, though due to 95% CI overlap and the relatively small difference in mean pass count this can be attributed to the limited sample size. Similarly the 74% compressed sequence possess significant overlap with the uncompressed sequence, but also exceeds the longest pass count of said sequence. Considering the relatively small scatter of the 74% compressed failure points it is reasonable to assert that the damage content was slightly decreased during the truncation procedure, which agrees with the behaviour exhibited during the application for unidirectional specimens. Predictions for the truncated sequences demonstrated good agreement with the experimental mean values, being slightly non-conservative.

5.4.5 Cycle Merging – Unidirectional

Cycle merging involves the substitution of turning points to replace many adjacent turning points in a sequence. This process uses equivalent damage calculations to ensure that the relatively large number of turning points being replaced has the same damage content as the few new turning points (Figure 5.23). Three different sequences were created by performing cycle merging, one with a ~40% length reductions compared to the uncompressed FALSTAFF sequence, one with a ~80% reduction and one with a ~90% reduction.

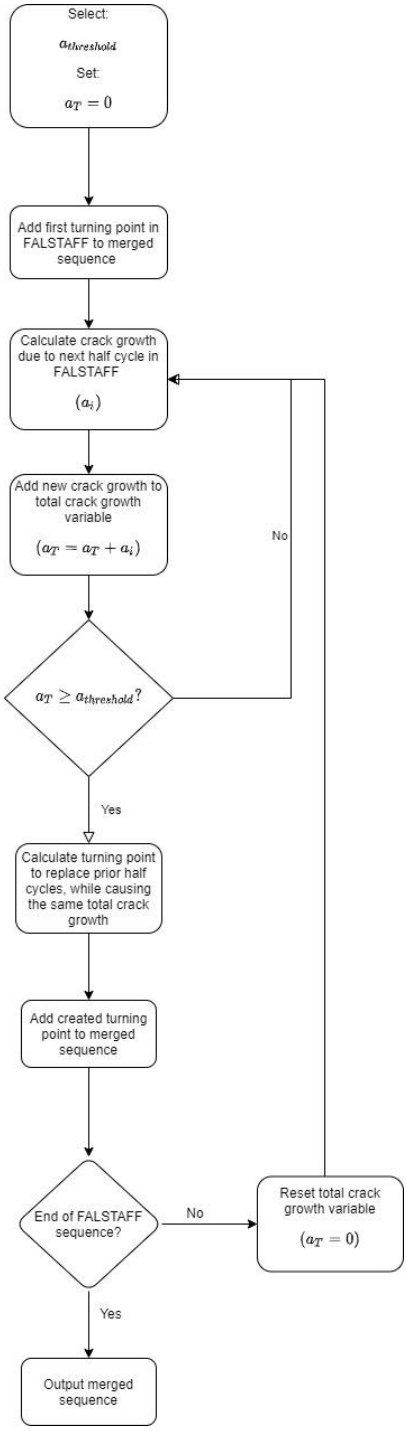

Figure 5-23 Flow chart of MATLAB script which performed cycle merging on the FALSTAFF sequence

A crack growth threshold was utilised to control how the FALSTAFF sequence was split into segments, each segment was merged and replaced with a single turning point. Crack growth predictions were performed on the uncompressed sequence (from the first turning point to the

last) until the total crack growth was equal to or greater than the selected threshold. At this stage all the turning points which contributed to the previous growth were defined as one segment and a single representative turning point was substituted in place of this segment (referred to as MERG-S). Crack growth predictions then recommenced from the newly included turning point and this process was repeated until the entire FALSTAFF sequence had been considered.

A variant of this method was also implemented which instead of replacing one segment with a single turning point, a block of repeating turning points is substituted in (referred to as MERG-B) to ensure the turning points remain below the maximum of the original sequence. The purpose of MERG-B was to prevent pseudo-static failure for occurring. Predictions for sequences created under both MERG-S and MERG-B are displayed in Table 5.7, showing that the damage content is near identical for sequences compressed to the same degree except for the 90% reduced sequences. As discussed in Section 5.4.3, indexed rainflow counting was applied before the damage calculations for life predictions. Therefore, a discrepancy between the damage calculations used for failure predictions and the damage calculations utilised when implementing cycle merging exists.

Table 5-7 Pass failure count of cycle merged FALSTAFF sequences produced using MERG-S and MERG-B methods.

FALSTAFF sequence	**Prediction MERG-S (Passes)**	**Prediction MERG-B (Passes)**
40% Merged	1.797	1.745
80% Merged	2.982	3.008
90% Merged	4.776	5.997

The merged sequences were each tested numerous times and are displayed in Figures 5.24 – 5.27 along with the experimental results from the uncompressed sequence.

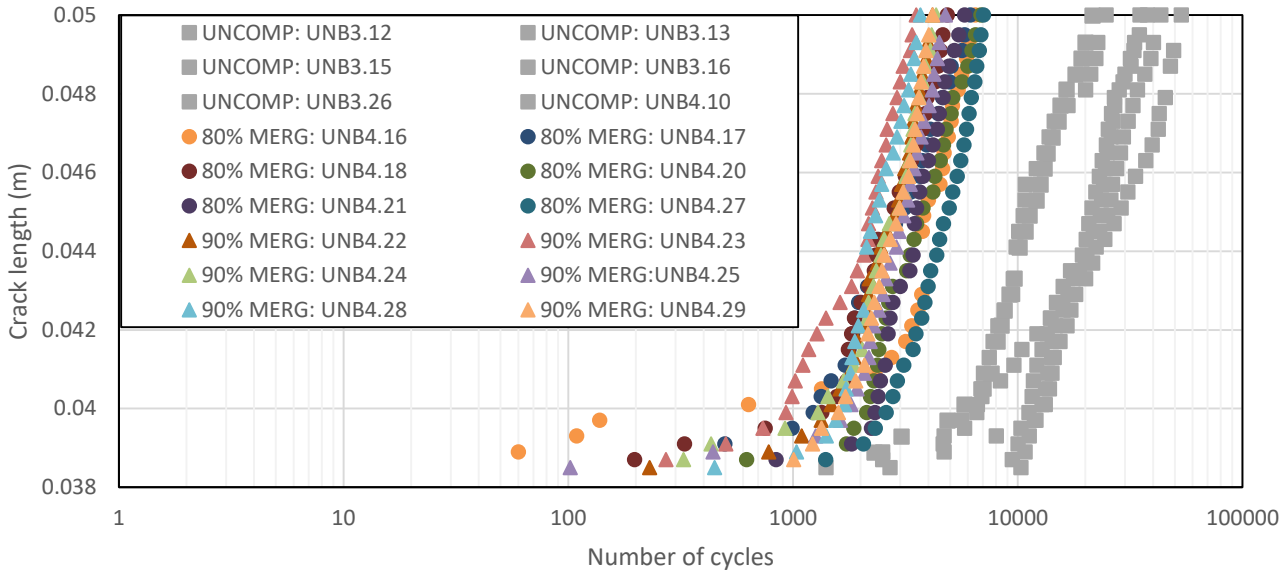

Figure 5-24 Crack growth curves of unidirectional specimens loaded under an adjusted FALSTAFF spectrum and two merged variations in terms of cycle count

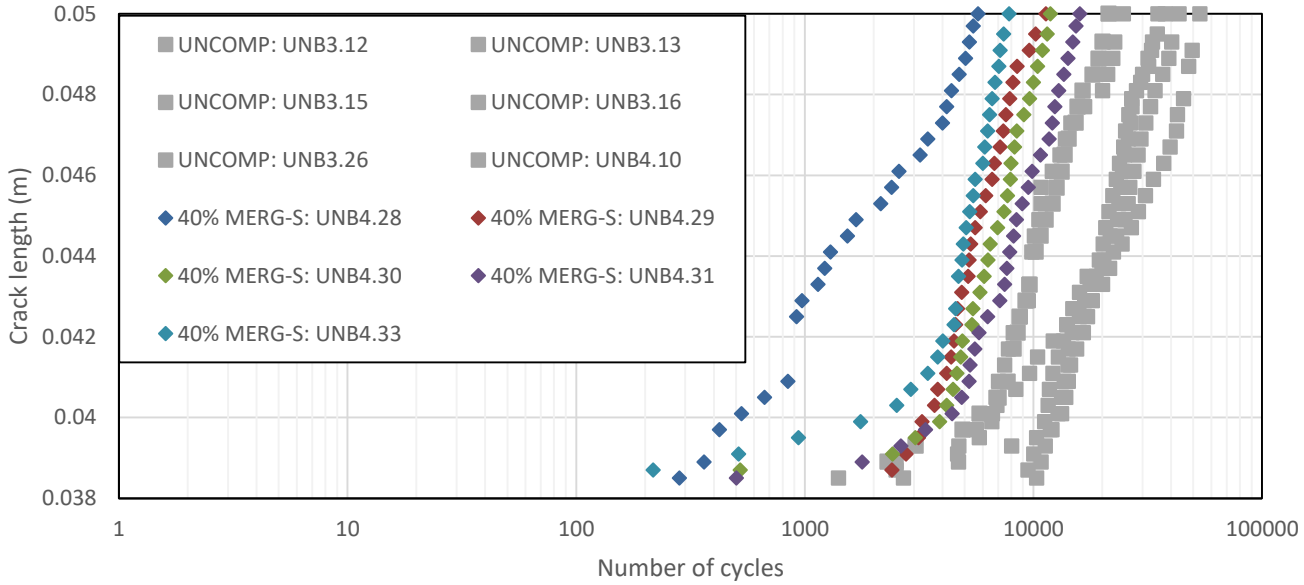

Figure 5-25 Crack growth curves of unidirectional specimens loaded under an adjusted FALSTAFF spectrum and 40% merged variation in terms of cycle count

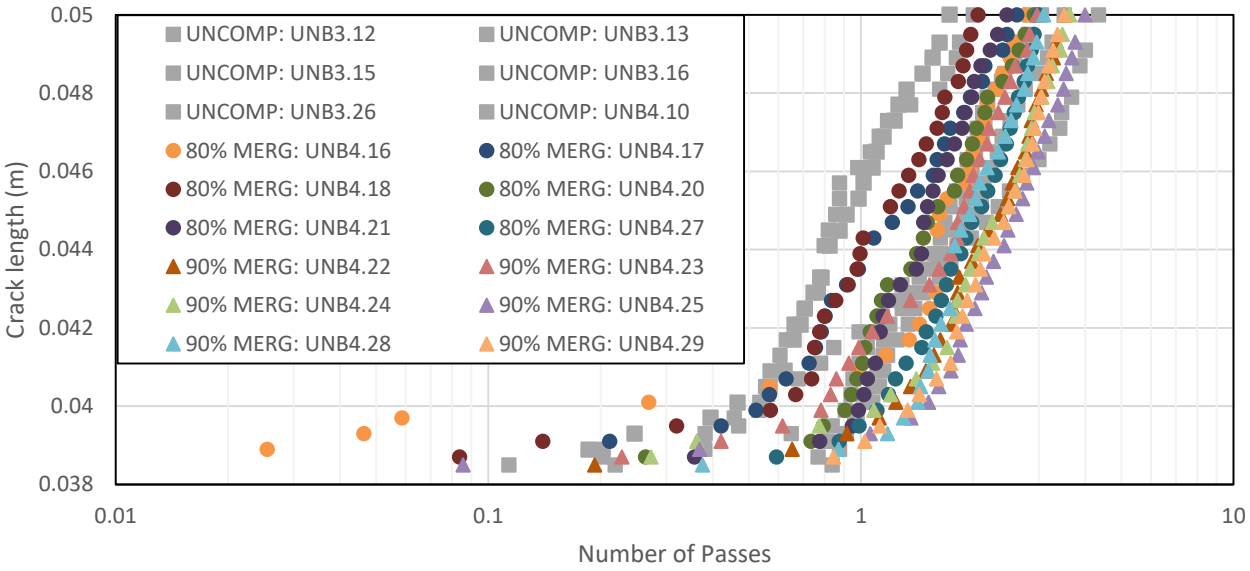

Figure 5-26 Crack growth curves of unidirectional specimens loaded under an adjusted FALSTAFF spectrum and two merged variations in terms of pass count

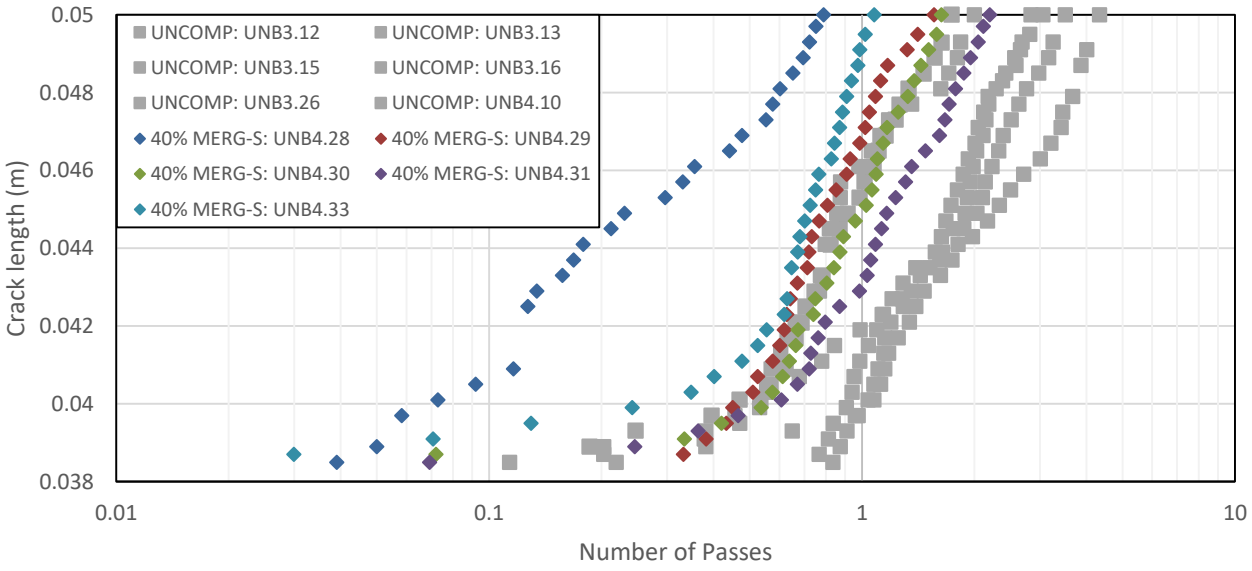

Figure 5-27 Crack growth curves of unidirectional specimens loaded under an adjusted FALSTAFF spectrum and 40% merged variation in terms of pass count

As previously displayed in Figures 5.17 and 5.18 for the truncation result, Figures 5.24 – 5.27 depict the experimental merging results in terms of cycle count and pass count. The notable decrease is test times is observable in Figure 5.24, while the test results from two of the merged sequences all reside within the range of experimental results from the uncompressed sequence (Figure 5.26).

The statistics of the failure distributions have been tabulated in Table 5.8 to enable comparisons between different levels of cycle merging and its effect on the mean failure point, with the distribution of failure points displayed in Figure 5.28.

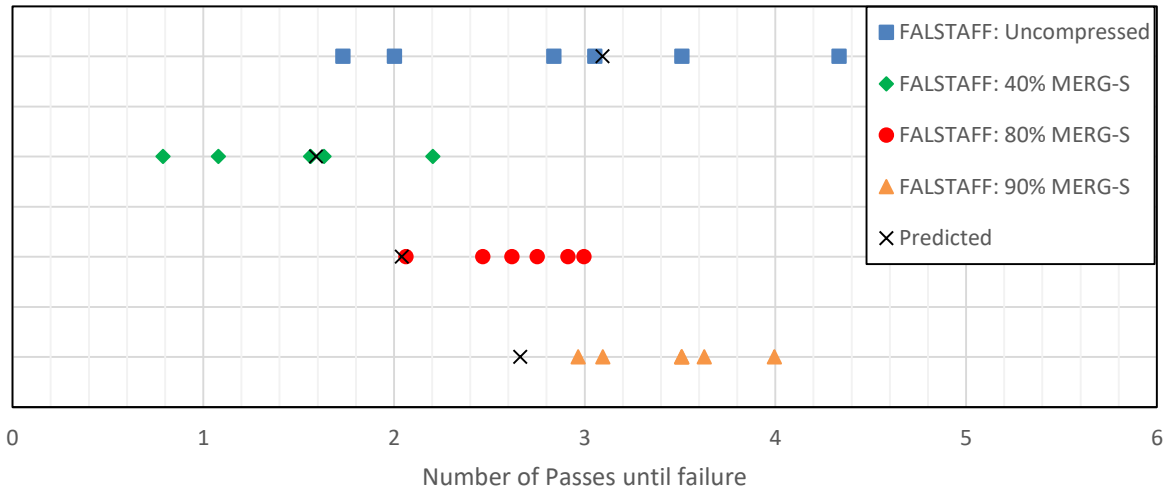

Figure 5-28 Distribution of failure points of each FALSTAFF fatigue loading test displayed in Figures 5.24 – 5.27 with a corresponding prediction for each set of tests

Table 5-8 Statistics of unidirectional specimen failure under uncompressed and cycle merged FALSTAFF sequences

FALSTAFF sequence	Mean failure pass count (Log-Norm)	Prediction	B -Basis Value	95% CI (Log-Norm)
Uncompressed	2.945	3.094	1.389	[2.071, 3.818]
40% Merged	1.480	1.591	0.656	[1.149, 1.811]
80% Merged	2.639	2.041	2.136	[2.535, 2.894]
90% Merged	3.453	2.662	2.894	[3.340, 3.566]

The 80% and 90% sets of experimental results from the merged FALSTAFF sequences fell within the data range of the uncompressed sequence. However, the 95% confidence intervals in Table 5.8 demonstrate that the variances of the merged sequences are significantly lower than the uncompressed. Furthermore, the uncompressed experimental results encompass both sets of merged test data. As the 80% and 90% merged sequences do not have overlapping 95% confidence intervals this indicates that the damage content of the two differs. This significant change in the variance of failure points signals for the fidelity of the sequence to be considered alongside the damage content.

The 80% merged sequence reflects the more conservative tests (lower pass counts) within the uncompressed test data, while the 90% merged sequence covers longer, less damaging tests. As the more damaging (shorter fatigue life) tests are of greater concerns when considering a sequences damage content, the 80% merged sequence is representative of the critical failure points of the uncompressed sequence.

The 40% merged sequence results demonstrated agreement with the failure prediction however the data spread indicates that a significant amount of damage was added to the sequence. When examined alongside the 80% and 90% data sets the manner in which cycle merging was performed becomes more clearly responsible for this difference in damage content. As all turning points but the first are replaced with new points, the longer the new merged sequence is, the more errors created by the prediction model (when creating these new turning points) can become apparent. Furthermore, the level of accuracy of the prediction model for given loading conditions (δ_{max}, R_d) will also influence how the damage content changes.

5.4.6 Cycle Merging - Woven

As described in Section 5.4.5, MERG-B was implemented to prevent pseudo-static failure from occurring by substituting blocks of turning points rather than a single turning point. Two

sequences were generated using MERG-B one which is 81% shorter than the uncompressed sequence and the other 90% shorter with the crack growth data displayed in Figures 5.29 and 5.30.

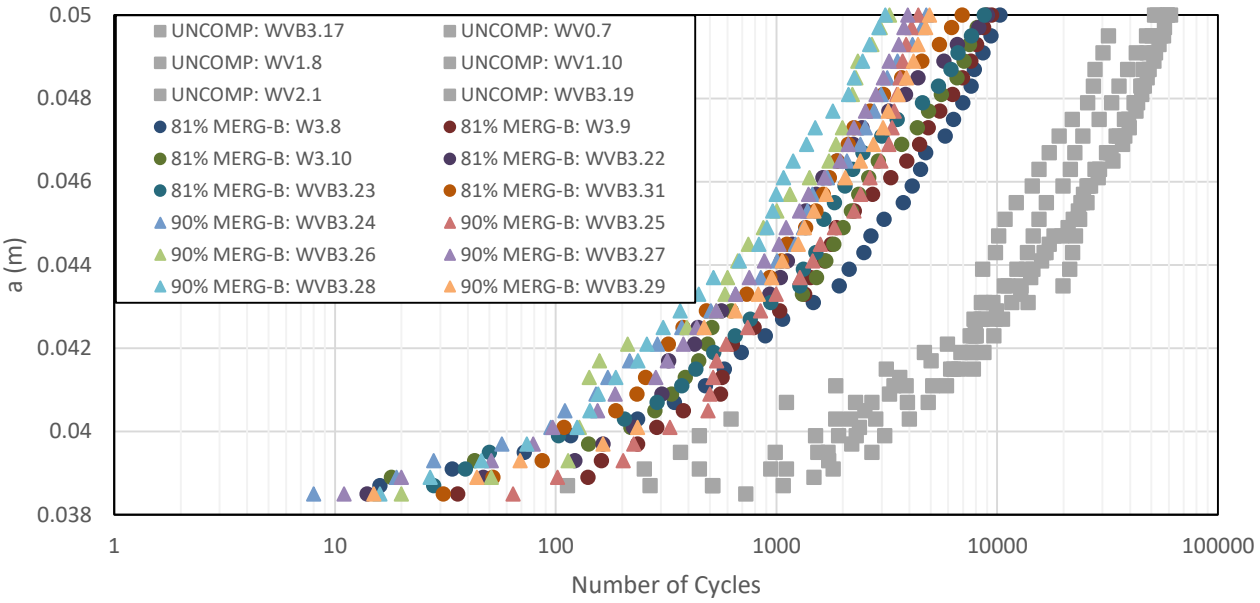

Figure 5-29 Crack growth curves of woven specimens loaded under an adjusted FALSTAFF spectrum and two merged variations in terms of cycle count

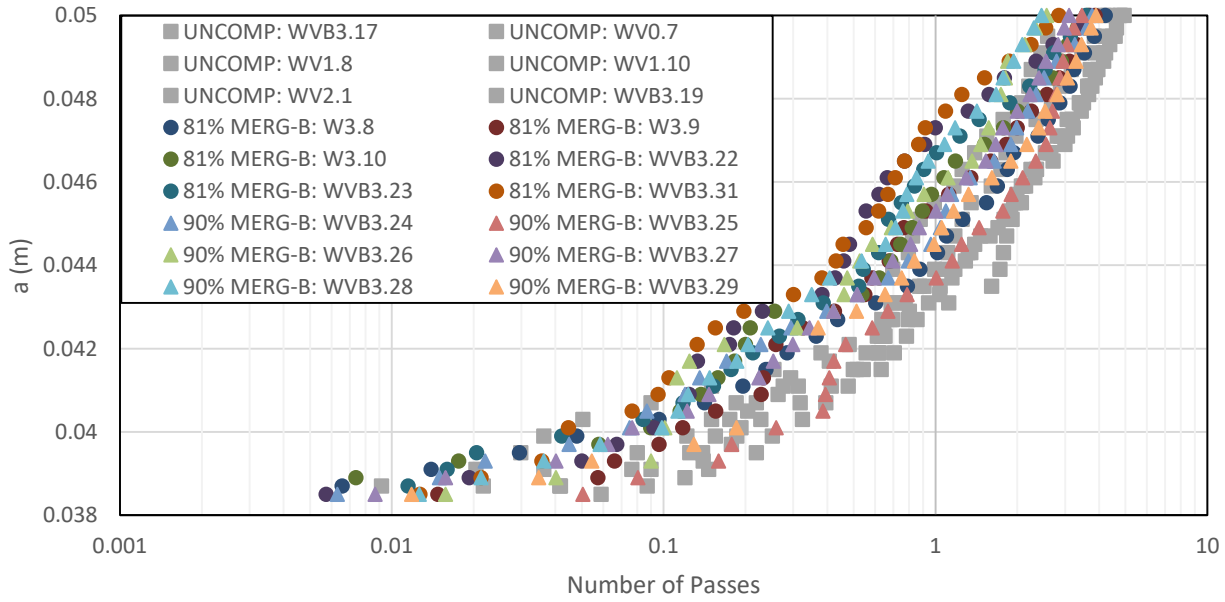

Figure 5-30 Crack growth curves of woven specimens loaded under an adjusted FALSTAFF spectrum and two merged variations in terms of pass count

The significant decrease in test time can be easily observed in Figure 5.29 with the two 'bands' of crack growth data sets. As with previous comparisons of tests by pass count, Figure 5.30 portrays the similarity of the damage contents of each sequence. The statistics of the failure distributions have been tabulated in Table 5.9 to enable comparisons between different levels of cycle merging and its effect on the mean failure point, with the distribution of failure points displayed in Figure 5.31.

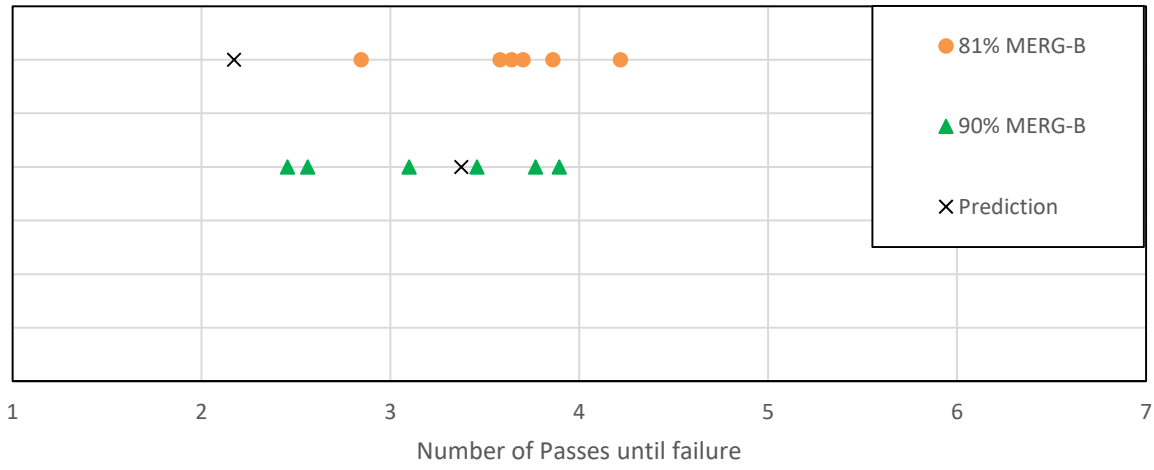

Figure 5-31 Distribution of failure points of each FALSTAFF fatigue loading test displayed in Figures 5.29 and 5.30 with a corresponding prediction for each set of tests

Table 5-9 Statistics of woven specimen failure under uncompressed and cycle merged FALSTAFF sequences

FALSTAFF sequence	Mean failure pass count (Log-Norm)	Prediction	B -Basis Value	95% CI (Log-Norm)
81% Merged	3.648	2.173	2.951	[3.463, 3.833]
90% Merged	3.218	3.377	2.255	[2.896, 3.540]

Both the 81% and 90% merged sequences possess a higher damage content than the uncompressed sequence based on the mean failure pass count values and scatter displayed in Figure 5.31. While sequences with higher damage contents do provide conservative life

predictions of the original, being overly conservative leads to over-design. The 81% merged sequence prediction indicate that damage is being underestimated, furthermore the predicted damage decrease from the 81% merged sequence to the 90% sequence which doesn't reflect the experimental results.

The peak displacement (3mm) of each sequence corresponds to the limit for a ~60% G_{IIc} constant amplitude test, which was commonly the most severe test for each R_d value (if tested at all), with predictions typically being conservative. As a significant number of turning points were created with magnitudes close to the maximum, the predictions therefore may be a result of the limited range of loading conditions in the test data.

Similarly to the case of truncation, the failure prediction calculations paired with experimental results indicate the calculation of equivalent half cycles is reasonably accurate while the absolute damage (crack growth due to each half cycle) is not. The variance of the 81% and 90% merged sequences are notably larger than those from Section 5.4.4, but the variances of the two sequences are also similar to each other in the same way that the 80% and 90% MERG-S sequences are. Therefore, the change in fidelity from 19% the original sequence's length to 10% was insignificant. More so then the unidirectional specimens, the implementation of cycle merging for use with the woven specimens has demonstrated the relative complexity of maintaining both damage content and fidelity when compared to truncation.

5.5 Comparison of Crack Surfaces Using Scanning Electron Microscopy (SEM)

A qualitative comparison of the crack surfaces was performed using scanning electron microscopy (SEM). Specimens which were loaded under the 90% merged FALSTAFF sequence were examined alongside those loaded under the uncompressed FALSTAFF sequence to determine whether the damage mechanisms remained consistent following severe spectrum compression. Images were chosen to be as representative of the overall crack surfaces as possible. The samples were imaged using an FEI Nova NanoSEM 450 with an accelerating voltage of 5kV at 5mm working distance. Beam current was controlled around 20pA to avoid sample charging while still maintaining a good signal to noise ratio for large area mapping. Tiled maps were then acquired and stitched using FEI MAPS software package.

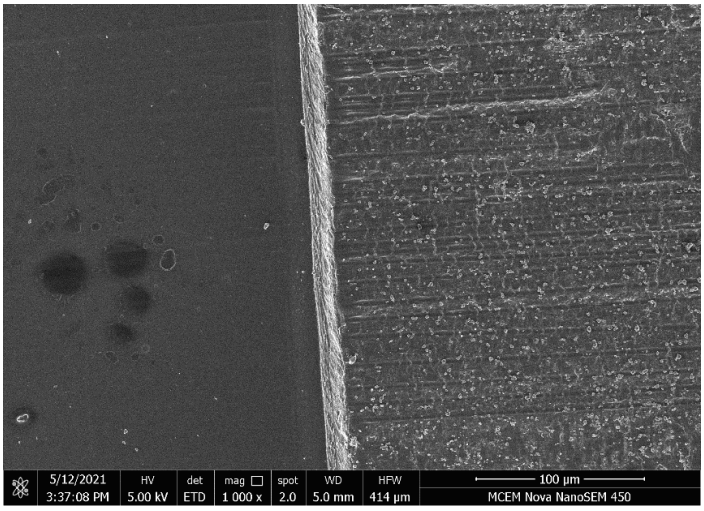

Figure 5-32 SEM image of a unidirectional specimen's crack surface, with the left section being the precracked region where a Teflon insert was present. The right region is where crack propagation occurred due to loading under a variation of the FALSTAFF sequence.

For the unidirectional specimens the crack propagated from left to right (in Figure 5.33), parallel with the fibres.

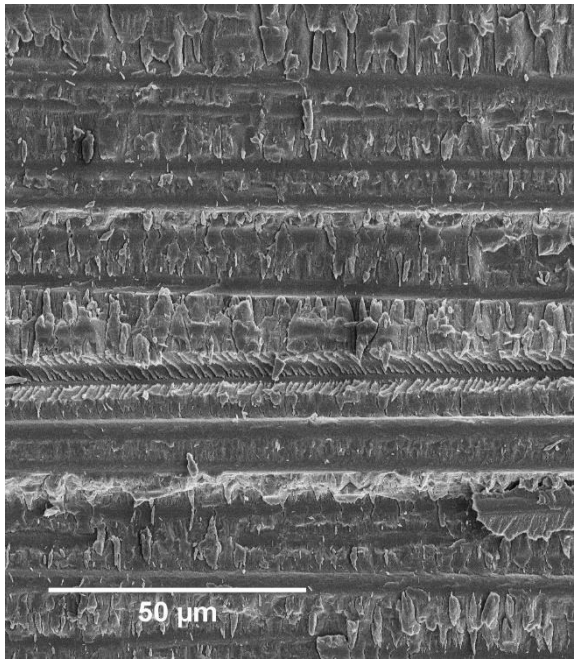

(a)

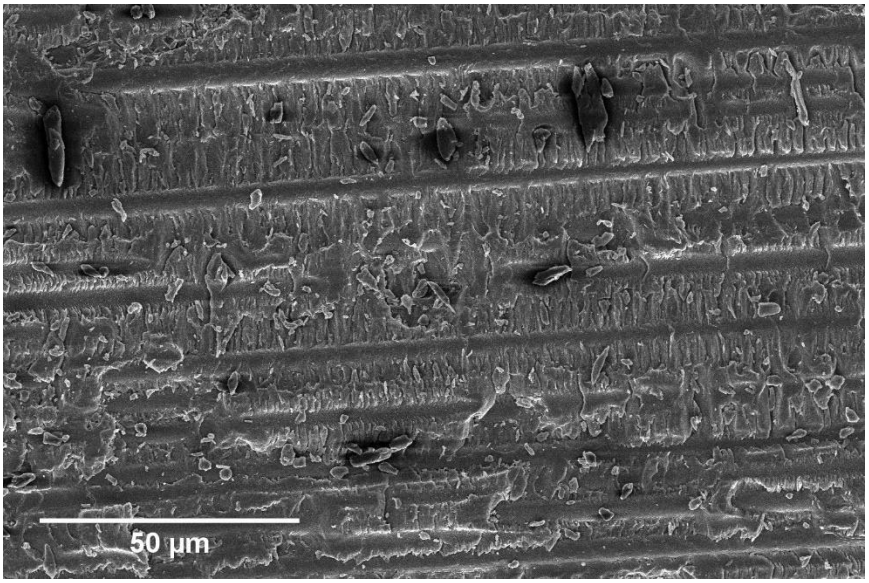

(b)

Figure 5-33 SEM images of unidirectional specimen crack surfaces having experienced mode II fatigue loading under variations of FALSTAFF sequence (a) Uncompressed (b) 90% Merged

Primarily matrix cracking was observed with gouge marks being perpendicular to the fibre direction, numerous cusps were visible between fibres. Several instances of interfacial damage were observed in the forms of fibre imprints and exposed fibres, demonstrating failure between the fibre-matrix interfaces for the unidirectional specimens. For the two examined specimens in Figure 5.33, the same general morphologies were observed across the scanned area of the fatigue induced crack growth region.

Scans were performed for the woven specimens at the meeting point of several tows to observe the damage morphology of fibres in differing orientations (Figure 5.34), again with the crack travelling from left to right.

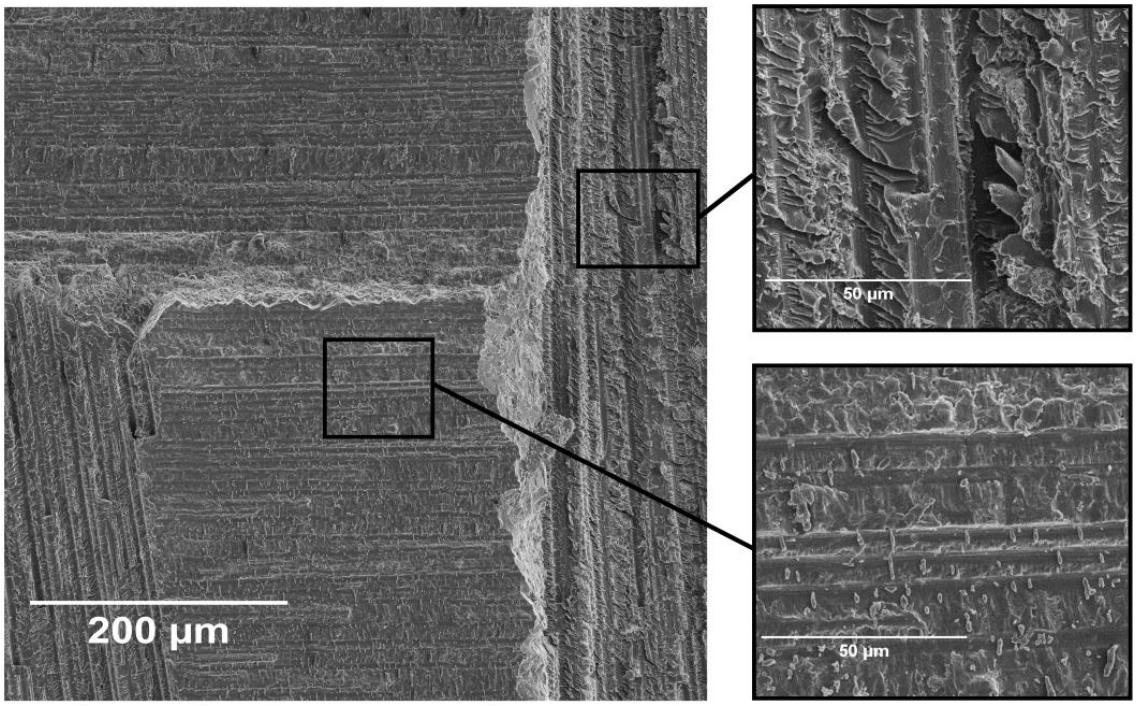

(a)

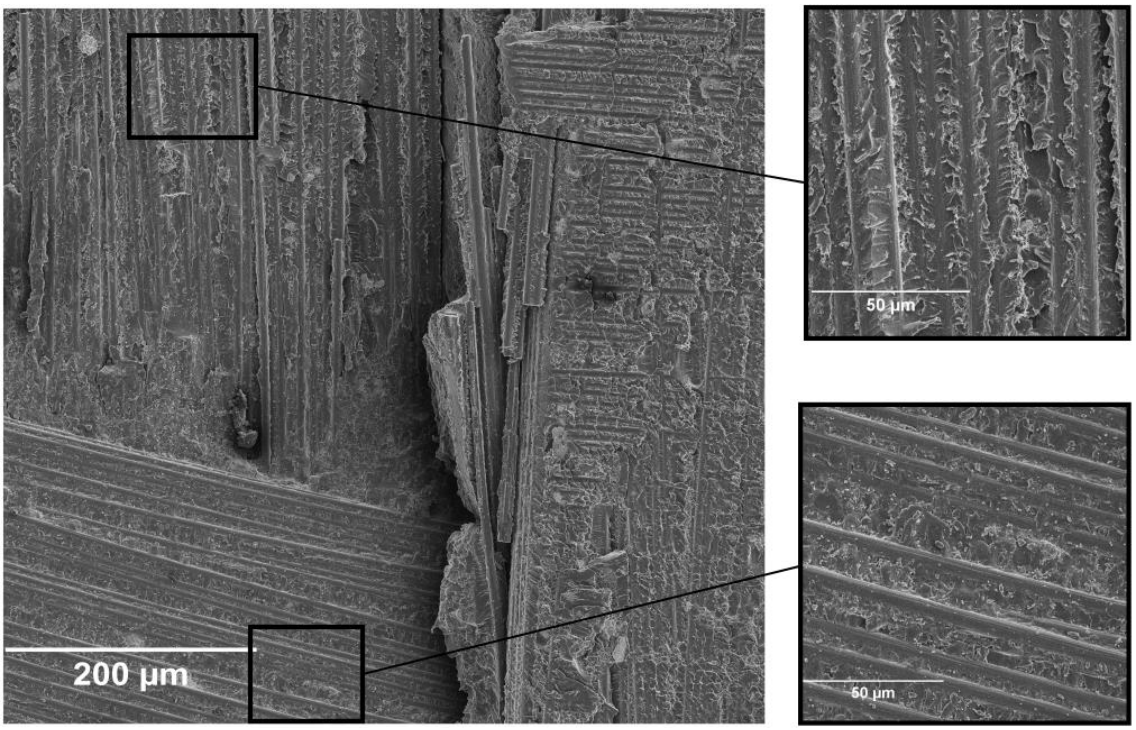

(b)

Figure 5-34 SEM images of woven specimen crack surfaces having experienced mode II fatigue loading under variations of FALSTAFF sequence (a) Uncompressed (b) 90% Merged

Tows with fibres positioned perpendicular to the crack propagation direction displayed a high proportion of fibre imprints than exposed fibres (matrix dominant fracture surface). Failure also appeared to be more brittle than that displayed by other tows, with cusps being clearly defined.

Tows which were aligned with the crack growth direction demonstrated predominantly exposed fibres, hence being fibre dominant fracture surfaces. Cusps were less pronounced and appeared smoother, indicating that cracking was less brittle than the perpendicular case and as a result the cusps have deteriorated. A notable amount of matrix debris was observed.

From a qualitative perspective, the SEM scans of uncompressed and 90% merged FALSTAFF loaded specimens demonstrate similar crack surfaces for both tested material types. The process

of severe cycle merging as previously described hasn't significantly changed the damage mechanisms experienced under mode II fatigue loading.

5.6 Chapter Summary

Constant displacement amplitude fatigue testing was carried out for the woven specimens, demonstrating a significantly higher fatigue resistance than the unidirectional specimens tested in Chapter 4. The acquired crack growth data aligned more closely to Paris' law with the previously observed short crack effects being absent, thus simplifying the construction of the CGRM. Predictions of constant amplitude loading utilising the CGRM showed good agreement with experimental results, demonstrating a higher proportion of conservative predictions then that of the unidirectional specimens.

Utilising the CGRM developed in Chapter 4 and adapting it, the damage content of the variable amplitude fatigue spectrum, FALSTAFF was determined for both a unidirectional and woven specimen.

To align the fatigue spectrum more so with previous experimental testing conditions the FALSTAFF sequence was modified. Truncation was performed through ranking each half cycle's damage content and then omitting turning points using an omission criteria. Conservative experimental results were achieved for both a 40% and 77% reduction in the spectrums length for the unidirectional specimen, however a 95% reduction led to a noteworthy decrease in the overall damage content of the spectrum. Predictions from the CGRM closely reflected the mean (Log-Norm) values of the experimental failure results falling within 10% of each other.

Two truncation sequences were generated for the woven specimens (40% and 74% reductions in original length), the sequences failure points reside within the data spread of the uncompressed sequence predominantly. However, the mean failure pass count of the 74% sequence was notably higher than the uncompressed version, indicating that a not insignificant amount of damage was

omitted. Experimental results indicate that the relative accuracy of damage calculations (ranking of half cycles) was sufficient to identify low damaging half cycles.

Three new sequences using cycle merging for the unidirectional specimens, one a 40% reduction of the uncompressed sequences length and two others for 80% and 90%. The 40% sequence unlike the other merged sequences had a substantially higher damage content highlighting the importance of both the accuracy of the prediction model utilised but also the method for performing cycle merging, as errors seemed to compound with the length of the newly merged sequence. While the experimental scatter for loading under both 80% and 90% sequences resided within the range of the uncompressed test results, the variance of each set of tests had significantly reduced when compared to the uncompressed version.

The technique of cycle merging was also extended to the woven specimens, though specifically through implementation of MERG-B rather than MERG-S. The two merged sequences (81% and 90% reductions in original length) had notably higher damage contents then the original but comparably similar variances, indicating that the substituted cycle blocks were excessively damaging. The notably higher damage content of these merged spectra was reflected experimentally and also in corresponding predictions, highlighting the importance in accounting for the segment linking half cycles when performing cycle merging. To ensure the fatigue life prediction accuracy, it is important to keep the R_d-ratio of the new cycles generated through merging within the R-ratio range used when the modified Paris law is generated (to keep spectrum fidelity, this should be kept further within the R_d-ratio range of the uncompressed spectrum).

The issues encountered with the implementation of cycle merging in this chapter will be examined and addressed in Chapter 6.

End of Chapter 5

Chapter 6

Combination of Truncation and Cycle Merging

6.1 Introduction

Having successfully performed truncation for the IM7/977-3 and M18/1/G939 specimens, this chapter addresses the sources of error which led to damage content discrepancy in the application of cycle merging observed in Chapter 5. An understanding of these factors informed the combination of truncation and cycle merging followed by iterative scaling of the resulting spectrum to maintain damage conservation.

6.2 Experimental Procedure

Fatigue tests were conducted using the setup and execution procedure detailed in Section 3.3 Fatigue Testing.

6.3 Damage Contribution of Truncated Cycles and Life Variation Introduced Through Cycle Merging

The cycles which were omitted during the truncation procedure for the unidirectional (77%) specimens were checked with the prediction and cycle merging damage calculation methods. By performing SHCM the uncompressed sequences were merged to the same degree as prior truncation cases to compare the damage contents (Table 6.1).

Table 6-1 The predicted failure pass counts using SHCM to compare damage omission associated with truncation and cycle merging as well as the cycles removed during the truncation process

	UNCOMP	TRUN (77%)	Truncated cycles	MERG (77%)	Ratio TRUN/UNCOMP	Ratio MERG/UNCOMP
UD	3.094	3.113	11,958	2.780	1.006	0.899

The calculation found the truncated cycles to contribute an insignificant amount of damage, requiring in excess of 10,000 passes to induce failure. By comparison truncation produced the least significant effects on the sequence's damage content as shown through the ratios of predicted fatigue lives. Table 6.1 demonstrates that while the truncated cycles do contribute insignificant amounts of damage, when performing cycle merging they can introduce errors through the equivalent life calculations. Therefore it is reasonable to exclude these cycles from the merging process, by initially performing truncation as demonstrated in Section 6.5 below. With damage retention calculations such as those shown in Table 1 enabling for the appropriate truncation level to be applied before applying cycle merging.

6.4 Cycle Merging Algorithm

This section details the changes that were made to the previously used cycle merging algorithm as well as considerations, to enable for improved sequence damage retention and fidelity.

6.4.1 Damage Preservation Between Segments

As the implemented cycle merging method doesn't incorporate rainflow counting the calculated damage content will differ from that of the predictions (see Section 5.2.5 and 5.2.6). However, the manner in which turning points are replaced also contributes to the adjusted damage content. As the turning points which are selected for merging are replaced by a single point (or multiple for MERG-B) with the first selected point having been retained from a previous iteration, the half cycle comprised of the final selected point and the sequential point is being adjusted. To illustrate this Figure 6.1 displays a sequence of five turning points labelled A-B-C-D-E. If half cycles A-B, B-C and C-D contributed enough damage to surpass/equal the crack growth threshold then they would be replaced with A-D' (where D' is the substituted turning point), this process ignores the half cycle D-E. If both points A and E are retained and D-E is considered then the new sequence A-D'-E should satisfy Equation 6.1.

$$da_{A-D'} + da_{D'-E} = da_{A-B} + da_{B-C} + da_{C-D} + da_{D-E} \qquad \text{Equation 6.1}$$

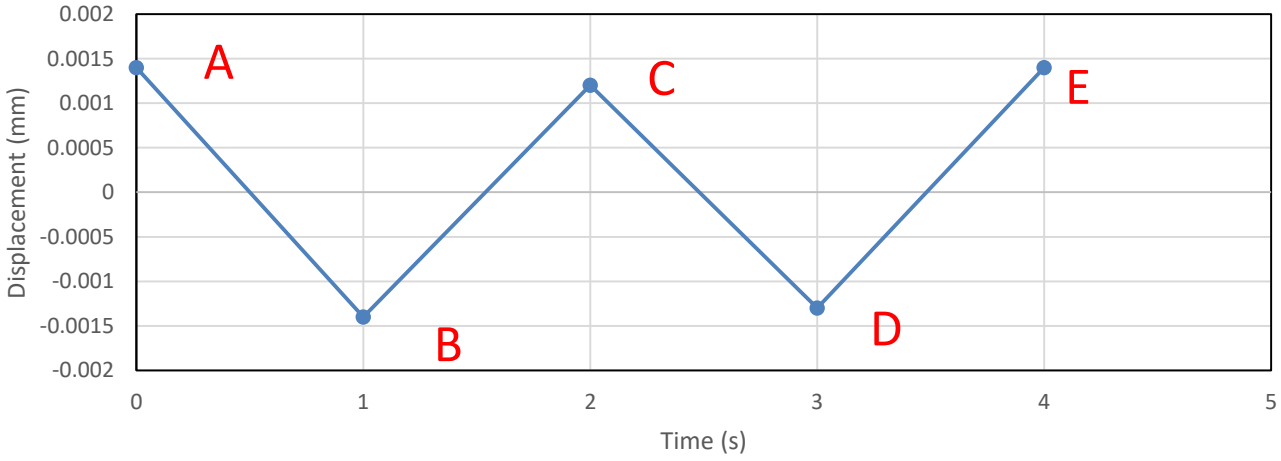

Figure 6-1 Sequence of five turning points (A-B-C-D-E), where points B,C and D are to be replaced with a single turning point through implementation of cycle merging

The right hand side of Equation 6.1 can be determined using Equation 4.9, while the left hand side is dependent on the new turning point. By solving Equation 6.1 the damage contribution of D-E will be accounted for, lessening the discrepancy with the uncompressed damage content. Implementation of this process led to the construction of Table 6.2 which details the theoretical failure predictions of cycle merged sequences using an algorithm which incorporates the concept of Equation 6.1.

Table 6-2 Predictions of failure for unidirectional and woven specimen failure under uncompressed and cycle merged FALSTAFF sequences conducted incorporating Equation 6.1

FALSTAFF sequence	Uncompressed	40% Merged	Equation 6.1 not used	80% Merged	Equation 6.1 not used	90% Merged	Equation 6.1 not used	95% Merged	Equation 6.1 not used
Prediction (Unidirectional)	3.094	2.801	1.591	2.783	2.041	2.520	2.662	2.490	3.453
Prediction (Woven)	4.691	4.508	1.116	4.604	2.173	4.555	3.377	4.874	3.996

Through the adjustment of the cycle merging algorithm, the half cycle following the merged turning points is accounted for resulting in a lessened change to the damage content. However, as is displayed in Table 6.2, a predicted discrepancy still remains between the uncompressed and merged sequences. The application of truncation will assist in addressing the error which is associated with cycles residing outside of the test range. As the vast majority of these cycles are not tested due to the excessive number of cycles required to induce failure, their damage contribution is observed to be negligible. The remaining difference in damage content exists due to the prediction and merging damage calculation methods differing by whether rainflow counting is utilised or not. This can be resolved through an iterative process of scaling the merged sequence to equate the uncompressed and merged predictions. The application of the cycle merging algorithm described in this section, truncation and scaling will be investigated in Section 6.5.

6.4.2 Damage Preservation Within a Segment and the Whole Spectrum

Merging within each segment would be conducted in two different ways. One can be referred to as the sequential half cycle method (SHCM). This method calculates the crack growth (or damage contribution) of each half cycle of the original spectrum and adds these together. When the summation reaches a selected threshold, the segment length is determined and all the original cycles in this segment are merged to form one new cycle. A more sophisticated method, referred as the segmented rainflow method (SRFM), accesses adjacent turning points from a sequence and rainflow counting them, followed by damage calculations to determine whether to merge the segment or not. If the damage contribution is below the selected threshold then the next adjacent turning point is added to the segment and the counting is repeated. While SRFM better preserves damage in the segments, SHCM is easier to apply and calculations performed by the author found the difference in damage content associated with the two methods to be small (<5%). In addition when the iteration method is used, to be discussed below, the differing degree to which damage is preserved between these two methods further diminishes, hence SHCM was implemented.

It is important to note that the damage preservation in a segment would help, but not guarantee, the damage preservation of the full spectrum. As performing rainflow counting on an entire sequence will result in different half/full cycles when compared to rainflow counting individual segments of a sequence, there will be a difference in the damage content following application of SHCM or SRFM, hence it is necessary to add/remove damage accordingly. After performing cycle merging the sequence can be scaled to ensure that the predicted damage content of the new sequence equals that of the uncompressed version. This involves iteratively adjusting a scaling factor while using the life prediction as a guide.

6.5 Combination of Truncation and Cycle Merging

Having found cycle merging to introduce errors in the spectrum's damage content through the equivalent damage calculations (adding/removing damage), the authors infer that the more substitutions that are performed the most significant the change in damage content will be. Therefore it is desirable to minimise the amount of cycle merging performed when simplifying a spectrum. To accomplish this, cycle merging was applied to spectrum which had already undergone truncation. The truncation had reduced the original sequence length by 77%, and the subsequent merging produced a sequence corresponding to a 95% decrease in the original spectrum length (T77% M95%). The truncation level of 77% of the sequence was chosen as little change in the damage content was observed when compared with previous iterations. However, the process for performing cycle merging utilises damage calculations which aren't equivalent to the damage calculations performed for predictions (which implements rainflow counting). Therefore there is a discrepancy between the method to perform merging and the method to judge the accuracy of merging. One aim of the merging process was to attain agreement between the mean pass count prediction of the uncompressed sequence and the merged versions. To achieve this, the T77% M95% sequence was scaled down by ~2.2% such that the predicted mean pass counts for the two sequences were equal (T77% M95%S).

The adjusted FALSTAFF sequence and T77% M95% variants were each tested several times and crack length data is displayed in Figures 6.2 and 6.3.

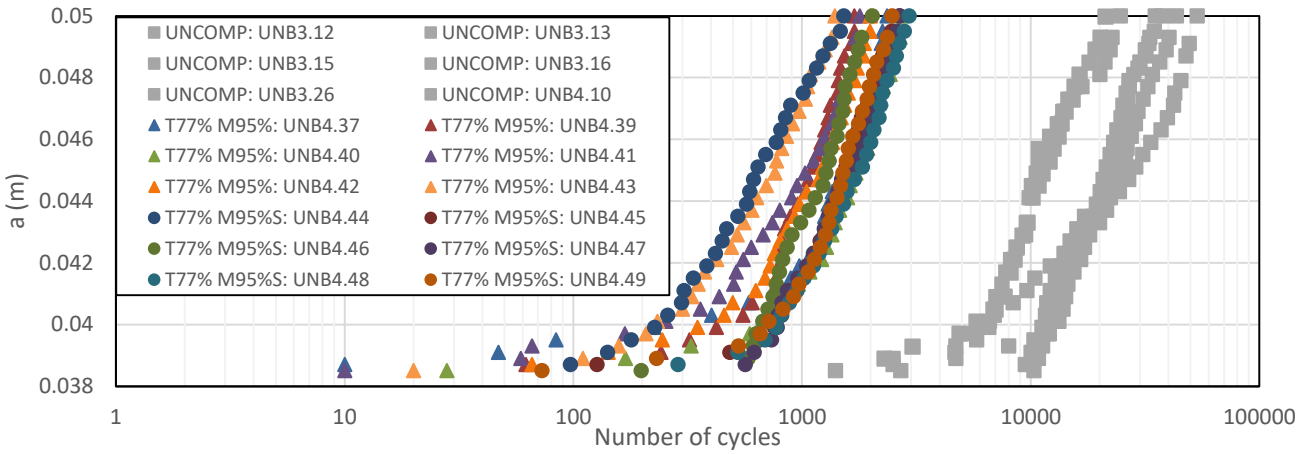

Figure 6-2 Crack growth curves of unidirectional specimens loaded under an adjusted FALSTAFF spectrum and two variations having undergone truncation and cycle merging in terms of cycle count

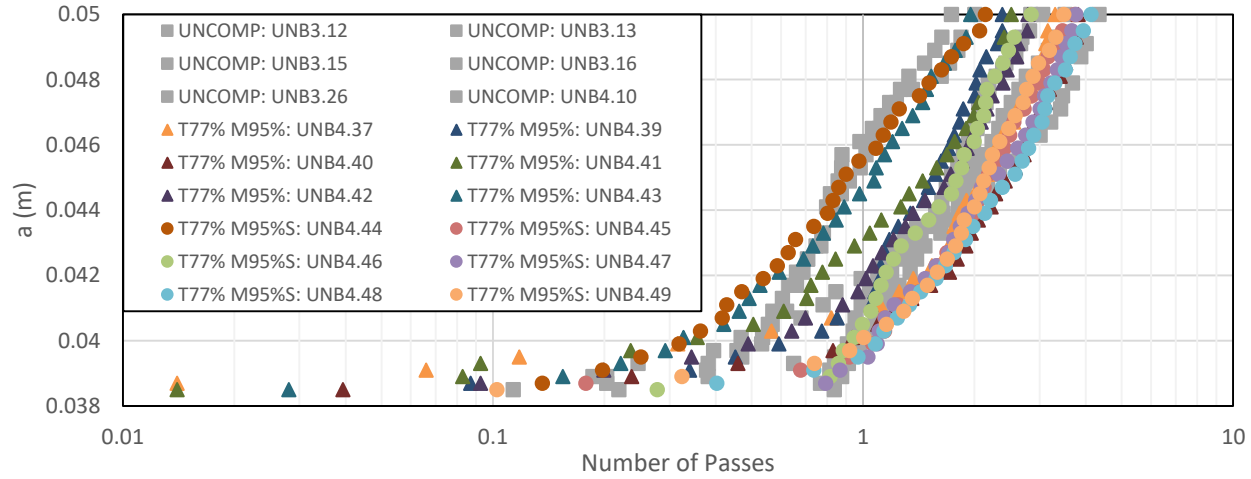

Figure 6-3 Crack growth curves of unidirectional specimens loaded under an adjusted FALSTAFF spectrum and two variations having undergone truncation and cycle merging in terms of pass count

The experimental failure points of each test are plotted with the corresponding predicted failure pass count in Figure 6.4. Loading under the T77% M95% sequences produced experimental distributions which reside within the uncompressed data set, while also displaying a similar mean pass count and failure scatter. The failure distribution statistics for the uncompressed and T77% M95% sequences are provided in Table 6.3.

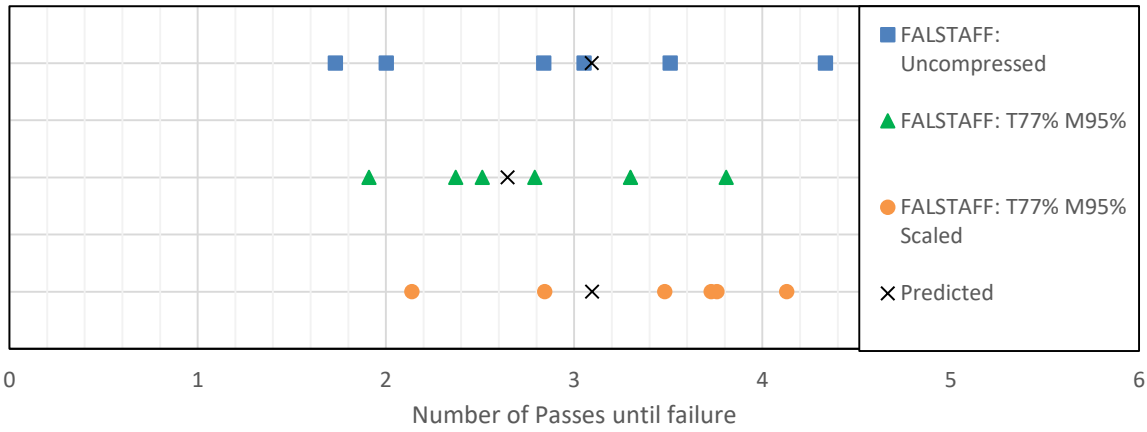

Figure 6-4 Distribution of failure points of each unidirectional FALSTAFF fatigue loading test displayed in Figures 6.2 and 6.3 with a corresponding prediction for each set of tests

Table 6-3 Statistics of unidirectional specimen failure under uncompressed and truncation and cycle merged FALSTAFF sequence

FALSTAFF sequence	Mean failure pass count (Log-Norm)	Prediction	B -Basis Value	Adjusted B Basis Value	95% CI (Log-Norm)
Uncompressed	2.945	3.094	1.389	1.389	[2.071, 3.818]
T77% M95%	2.796	2.646	1.716	1.561	[2.407, 3.184]
T77% M95%S	3.368	3.094	2.179	1.493	[2.816, 3.920]

The sequences which were initially truncated before undergoing merging demonstrated good agreement with the uncompressed sequence both in terms of mean pass count and data

distribution. Demonstrating the benefit of utilising truncation to omit low damaging cycles until the techniques limit is reached (before notably damaging cycles start being removed), and then further reducing the sequences length through substitution of equivalent damage cycles. The ability to iteratively scale the sequence following cycle merging enables for damage to be returned (or removed), overcoming error introduced due to a discrepancy in damage content. The initial implementation of truncation improved the retention of damage content when undergoing cycle merging as was observed with T77% M95% sequences. This can be partially attributed to the lessening degree to which cycles were combined due to the sequence length being shorter.

6.6 Discussion about B-Basis Values

It should be noted that the B-Basis values increased notably as the sequences were compressed (Table 6.3), this is due to the decrease in experimental variance combined with the differences between the experimental means and predictions when compared to the uncompressed sequence. A preliminary approach was applied to indicatively handle this problem involving the application of a linear regression (Figure 6.5) using ratios of the standard deviation, experimental mean and prediction values (select sequence/uncompressed sequence). The 40% and 77% truncated sequences and T77% M95% sequences were the subject of this adjustment. The B-Basis Factor was multiplied to the B-Basis values to obtain the adjustment values (the ideal B-Basis Factors would result in the B-Basis values all equalling the uncompressed value).

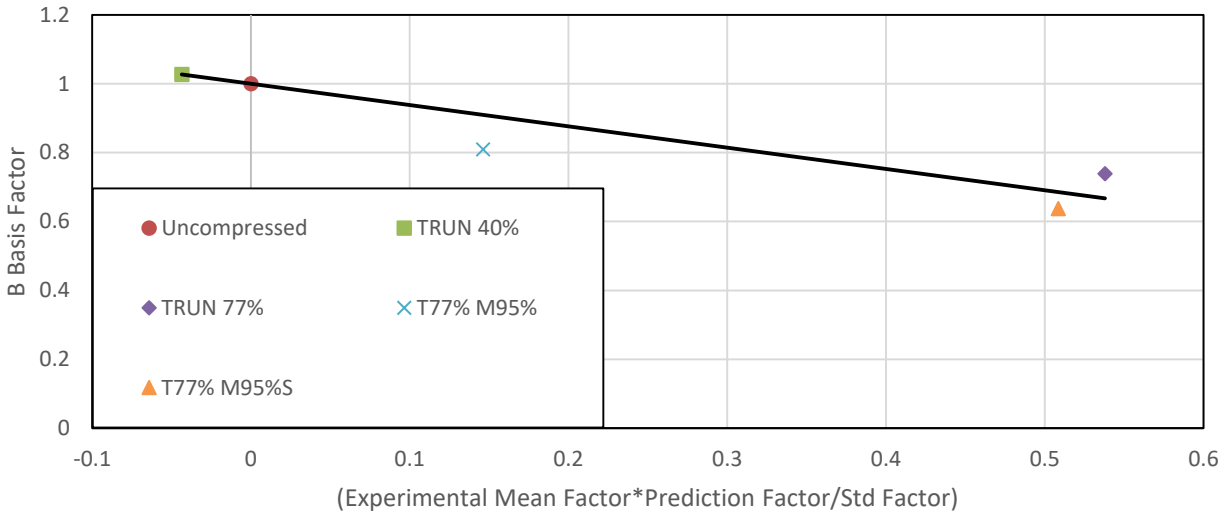

Figure 6-5 Linear regression using experimental mean, prediction and standard deviation factors to adjust the B Basis values of the compressed fatigue spectra

More test data would be required to rigorously address this issue.

6.7 Effects of Spectrum Reduction on R_d Ratio Distribution

To assess the implementation of truncation and cycle merging the modification to the original sequences loading distribution should be considered. Heat maps have been created to illustrate the distribution of loading conditions of sequences at each stage of simplification. As the uncompressed FALSTAFF sequence used was restricted to negative R_d values, the two diagonal lines included on the plots in Figure 6.6 bound all cycles. All predicted failure pass count values for the sequences displayed in Figure 6.6 are listed in Tables 5.4 and 6.3, except for T77%M95% (SRFM) which was predicted to fail after 4.845 passes. Comparing the SHCM and SRFM merging applications indicates that SHCM tends to add damage while SRFM removes it, however the applicability of this observation to other spectra is unknown.

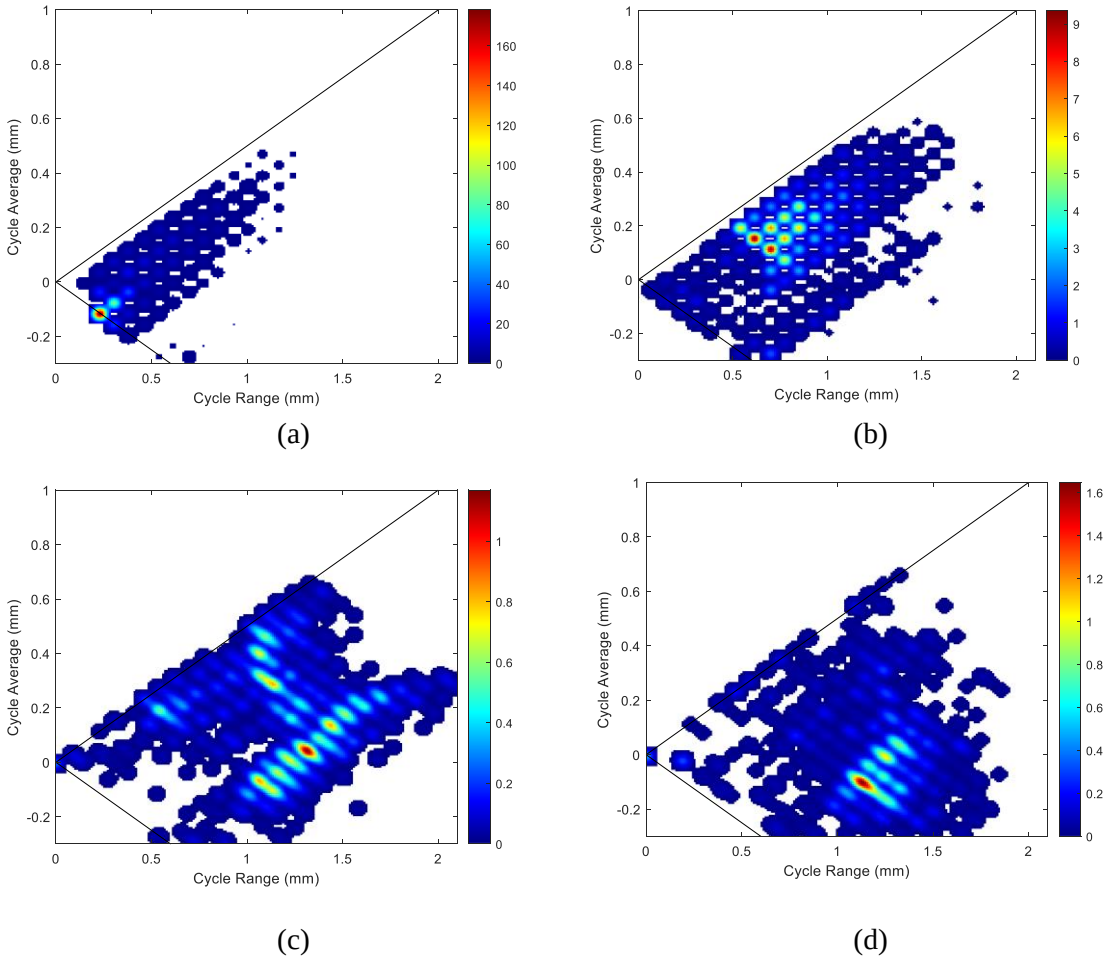

Figure 6-6 Rainflow counting of the adjusted FALSTAFF sequence at different stages of spectrum reduction: (a) Uncompressed (b) TRUN 77% (c) T77%M95% (SHCM) (d) TRUN77%M95% (SRFM). The diagonal lines on the histogram represent R_d=0 cycles, above the top line and below the bottom line are R_d>0 cycles

The process of truncation (Figure 6.6 (a) and (b)) led to a higher proportion of cycles being high damaging (increased cycle range) with the shape of the rainflow distribution relatively similar to the original. While the action of cycle merging (either through SHCM or SRFM) produced more notably different distributions, though all cycles still resided within the R_d ratio bounds of the original. As truncation is the least invasive of the techniques it was expected it would alter the loading distribution the least. Never the less analysing the rainflow matrices of the spectrum as it undergoes simplification enables for fidelity retention to be accessed. Such analysis also presents the question as to whether maintaining the distribution of loading conditions (such as constraining

the bounds of R_d values and cycle range) would significantly improve either/both of damage content and fidelity.

6.8 Chapter Summary

The initial truncation of FALSTAFF by 77% paired with an adjustment to the merging algorithm assisted with addressing the errors introduced with excessive application of cycle merging. A broader experimental scatter was observed with a mean pass count within 6% of the associated prediction. Iterative scaling of the truncated and merged sequence enabled for the damage content to be matched to that of the uncompressed sequence. This addressed the discrepancy existing due to the differing methods for determining damage content when performing cycle merging versus predicting failure.

In conclusion, truncation has demonstrated its capability to remove large amounts of low damaging cycles with relative simplicity, while cycle merging needs further considerations such as iterative scaling to ensure the newly designed sequence is representative of the original both in terms of damage content and fidelity.

End of Chapter 6

Chapter 7

Summary and Conclusions

The purpose of this dissertation was to conservatively implement spectrum reduction techniques on load sequences which would be applied to unidirectional and woven composite specimens. A ground up approach was taken, beginning with static testing followed by constant amplitude fatigue to enable the construction of prediction models. Utilising predictive modelling enabled for damage to be attributed to variable amplitude fatigue loading sequences but also informed the spectrum reduction techniques; truncation and cycle merging. As such this work has several key stages; Firstly, to construct a fatigue prediction model, secondly, to successfully apply reduction techniques to the unidirectional specimens, and finally to extend the general approach of the first two steps to the woven specimens.

With the increasing integration of composite material into aerospace structures the certification and through-life support processes face challenges due to the substantial differences between

composite damage mechanisms and those of metals. With loading sequences taken from in-service vehicles consisting of excessive numbers of turning points, the need and benefits of length reduction is straightforward. To ensure that safe-life predictions are well informed both the fatigue characteristics and damage growth behaviour need to be considered and understood.

7.1 Major Findings

The main conclusions of this thesis and the results from both experimental and numerical testing are detailed in this section.

A component of this work included a literature review paper which was published and has the following details:

- Healey, R., Wang, J., Chiu, W.K., Chowdhury, N.M., Baker, A. and Wallbrink, C., 2021. A Review on Aircraft Spectra Simplification Techniques for Composite Structures. *Composites Part C: Open Access*, p.100131.

7.1.1 Development of fatigue life prediction models

Chapter 4 focused on the characterisation of IM7/977-3 carbon fibre prepreg specimens under mode II fatigue loading and the generation of prediction models. Static testing was conducted using a 100kN Instron servo-hydraulic machine according to the ASTM 7905. Constant amplitude and block loading fatigue tests were subsequently performed using a reversible three point bending fixture. The following conclusions were taken from the experimental testing and modelling:

i. Static testing of IM7/977-3 specimens displayed agreement with both J integral and displacement field FEA, providing a benchmark for the examination of the M18/1/G939 specimen.

ii. The strain energy release rate equation detailed in the ASTM 7905 was confirmed to significantly underestimate G_{II} for M18/1/G939, therefore FEA can be utilised to appropriately scale up these values.

iii. Constant amplitude fatigue testing was conducted for IM7/977-3 under mode II loading and no endurance limits were observed experimentally.

iv. Block loading fatigue testing demonstrated loading sequence effects with H-L being consistently more damaging than L-H loading.

v. Adjustments to a residual strength model were created to allow for displacement controlled fatigue data to be properly incorporated. Enabling for life predictions under variable amplitude loading, and producing more accurate and conservative estimates than the Walker-Miner approach for tested block loading sequences.

vi. Adjustments to a crack growth model were implemented to collapse crack growth data from constant amplitude testing, accounting for short crack effects in the context of displacement control loading. Both constant amplitude and block loading predictions displayed good agreement with experimental observations.

The work presented in this chapter is primarily covered in the following publications:

- Healey, R., Chowdhury, N.M., Chiu, W.K. and Wang, J., 2019. Experimental and numerical determination of mode II fracture toughness of woven composites verified through unidirectional composite test data. *Polymers and Polymer Composites*, *27*(9), pp.557-566.
- Chowdhury, N.M., Healey, R., Wang, J., Chiu, W.K. and Wallbrink, C., 2020. Using a residual strength model to predict mode II delamination failure of composite materials under block fatigue loading. *International Journal of Fatigue*, *135*, p.105563.

7.1.2 Performing spectra reduction and an extension of the fatigue simplification methodology to a M18/1/G939 material

Using the prediction modelling described in Chapter 4, Chapter 5 applies both truncation and cycle merging to reduce the length of an adjusted FALSTAFF sequence for both specimen types. Truncation was implemented by ranking each half cycle with the original sequence and then omitting those which possessed the smallest damage until notable changes to the overall content

became apparent. Merging combined adjacent turning points to single points through equivalent damage calculations. All newly created sequences were then tested using the reversible three point bending test fixture with crack growth data recorded, with scanning electron microscopy being performed to compare crack surfaces. The following points highlight the findings from this work:

i. M18/1/G939 demonstrated a higher fatigue resistance under mode II loading when compared to the IM7/977-3 constant amplitude fatigue data
ii. Crack growth modelling produced conservative constant amplitude fatigue predictions with FEA being utilised to appropriately scale G_{II}
iii. Retested specimens which previously underwent constant amplitude fatigue loading demonstrated notably longer fatigue lives even though the initial crack length was the same as initial testing (achieved by shifting the specimen in test fixture).
iv. Truncation successfully reduced the length of the original sequence by 40% and 77% with comparable damage for IM7/977-3. A 95% truncation resulted in a significant decrease in the overall damage content, hence the 'limit' of truncation exists between the reduction percentages of 77% and 95% for this sequence. Crack growth rate modelling produced conservative and accurate predictions for the uncompressed and truncated sequences.
v. Truncation was performed on FALSTAFF sequences for M18/1/G939 which was scaled with a maximum displacement of 3.0mm. Two sequences were generated (40% and 74%) and used to fatigue specimens. The 74% truncated sequence presented a notably higher means failure pass count to the uncompressed version, indicating that damaging cycles were omitted.
vi. Independent implementation of cycle merging produced three new sequences for IM7/977-3; a 40% reduction in length as well as 80% and 90%. The 40% sequence demonstrated a notably higher damage content then the original, indicating that excessive substitution calculations lead to accumulated error. The other two reduced sequences

resided within the uncompressed experimental range but with significantly reduced variances. The predictions for each sequence were either within 5% of the experimental mean pass count or conservative.

vii. Two sequences were produced through the application of MERG-B with reduction levels of 81% and 90%. Both showed an increase in mean damage content paired with a decrease in variance, similar to behaviour observed with the unidirectional specimens.

viii. Qualitative comparison of scanning electron microscopy images depicted similar crack surface characteristics between a specimen which underwent loading from the uncompressed FALSTAFF sequence and the 90% merged version.

The work presented in this chapter is primarily covered in the following publications:

- Healey, R., Wang, J., Wallbrink, C. and Chiu, W.K., 2021. Predicting mode II delamination growth of composite materials to assist simplification of fatigue spectra by truncating non-damaging cycles validated with experiment. *International Journal of Fatigue*, *145*, p.106117.
- Healey, R., Wang, J., Wallbrink, C., Chiu, W.K. and Xu, Z., 2021. The application of cycle merging and an extension of a fatigue spectrum simplification methodology from unidirectional to woven composite materials, *International Journal of Fatigue*, Under Review

7.1.3 Combination of truncation and cycle merging

The final component of this thesis was the adjustment of the cycle merging algorithm followed by the combination of truncation and cycle merging with iterative scaling. The following conclusions were drawn:

i. Applying cycle merging to the 74% truncated sequence improved damage retention when compared to pure cycle merging, with similar failure distribution being observed and an overall 95% reduction in length. Successful down scaling of the sequence T77% M95% led to agreement between the uncompressed and new sequences prediction values. Experimental scatter of both T77% M95% and T77% M95%S strongly resembled that of

the uncompressed sequence. Therefore cycle merging has demonstrated its ability to overcome the reduction limitations of truncation.

ii. To reduce the alteration of the damage content of a sequence which undergoes cycle merging, consideration was given to the half cycle following the segment being substituted. Theoretical failure predictions for merged sequences demonstrated an improved similarity to the original sequence following this adjustment.

The work presented in this chapter is primarily covered in the following publication:

- Healey, R., Wang, J., Wallbrink, C., Chiu, W.K. and Xu, Z., 2021. The application of cycle merging and an extension of a fatigue spectrum simplification methodology from unidirectional to woven composite materials, *International Journal of Fatigue*, Under Review

7.2 Recommendations

The following recommendations for future work should be considered to further spectrum reduction for composite materials.

i. Mode II delamination was the failure mode examined in this work. Investigating other forms of loading such as mode I, III and mixed modes would be an important extension to this project.

ii. The spectrum reduction methodology detailed was extended from a unidirectional specimen to a woven specimen to demonstrate it having sufficient generality for application to several composite types. Further exploration of other composite layups and specimen types would better inform the applicability of this method.

iii. The examined spectrum was simplified while keeping the global maximum displacement of the sequence constant while maintain the R_d values within the constant amplitude test range. However, further constraining the cycle merging procedure to better maintain the loading distribution may improve the damage retention and fidelity of the original spectrum.

iv. Numerical analysis concerning composite fatigue under spectrum loading has seen very little work at the time of writing. Developing a computational model which can predict fatigue damage under complex loading would enable for spectrum simplification procedure to be implemented and tested quickly.

End of Chapter 7

Bibliography

1. Healey, R., J. Wang, W.K. Chiu, N.M. Chowdhury, A. Baker, and C. Wallbrink, *A review on aircraft spectra simplification techniques for composite structures.* Composites Part C: Open Access, 2021. **5**: p. 100131.

2. ASTM-International, *ASTM D6115-97(2011)*, in *Standard Test Method for Mode I Fatigue Delamination Growth Onset of Unidirectional Fiber-Reinforced Polymer Matrix Composites*. West Conshohocken, PA.

3. International, A., *ASTM D7905 / D7905M-14*, in *Standard Test Method for Determination of the Mode II Interlaminar Fracture Toughness of Unidirectional Fiber-Reinforced Polymer Matrix Composites*. 2014: West Conshohocken.

4. Mehrabadi, F. and M. Khoshravan, *Mode III interlaminar fracture and damage characterization in woven fabric-reinforced glass/epoxy composite laminates*. Vol. 47. 2013. 1583-1592.

5. ASTM-International, *ASTM D 6671/D 6671M - 06*, in *Standard Test method for Mixed mode I- Mode II Interlaminar Fracture Toughness of Unidirectional Fiber Reinforced Polymer Matrix Composites*. 2010: West Conshohocken, PA.

6. ASTM-International, *ASTM D5528-13*, in *Standard Test Method for Mode I Interlaminar Fracture Toughness of Unidirectional Fiber-Reinforced Polymer Matrix Composites*. 2013: West Conshohocken, PA.

7. ASTM-International, *ASTM D7905 / D7905M-14*, in *Standard Test Method for Determination of the Mode II Interlaminar Fracture Toughness of Unidirectional Fiber-Reinforced Polymer Matrix Composites*. 2014: West Conshohocken.

8. International, A., *ASTM D 5687/D 5687M -95 (Reapproved 2002)*, in *Standard Guide for Preparation of Flat Composite Panels with Processing Guidelines for Specimen Preparation*. 1995, ASTM

9. Bower, A.F., *Applied mechanics of solids*. 2009, CRC press. 1-795.

10. Davidson, B.D., C.S. Altonen, and J.J. Polaha. *Effect of stacking sequence on delamination toughness and delamination growth behavior in composite end-notched flexure specimens*. in *Proceedings of the 1994 Symposium on Composite Materials: Testing and Design (Twelfth Volume), May 16, 1994 - May 17, 1994*. 1996. Montreal, Can: ASTM.

11. Pereira, A.B. and A.B. De Morais, *Mode II interlaminar fracture of glass/epoxy multidirectional laminates.* Composites Part A: Applied Science and Manufacturing, 2004. **35**(2): p. 265-272.

12. Shokrieh, M.M., H. Rajabpour-Shirazi, M. Heidari-Rarani, and M. Haghpanahi, *Simulation of mode I delamination propagation in multidirectional composites with R-curve effects using VCCT method.* Computational Materials Science, 2012. **65**: p. 66-73.

13. Heidari-Rarani, M. and M. Sayedain, *Finite element modeling strategies for 2D and 3D delamination propagation in composite DCB specimens using VCCT, CZM and XFEM approaches.* Theoretical and Applied Fracture Mechanics, 2019. **103**: p. 102246.

14. Alizadeh, F. and C. Guedes Soares, *Experimental and numerical investigation of the fracture toughness of Glass/Vinylester composite laminates.* European Journal of Mechanics - A/Solids, 2019. **73**: p. 204-211.

15. Herráez, M., N. Pichler, G.A. Pappas, C. Blondeau, and J. Botsis, *Experiments and numerical modelling on angle-ply laminates under remote mode II loading.* Composites Part A: Applied Science and Manufacturing, 2020. **134**: p. 105886.

16. Jahanian, E. and A. Zeinedini, *Influence of drilling on mode II delamination of E-glass/epoxy laminated composites.* Theoretical and Applied Fracture Mechanics, 2018. **96**: p. 398-407.

17. Ge, Y., X. Gong, A. Hurez, and E. De Luycker, *Test methods for measuring pure mode III delamination toughness of composite.* Polymer Testing, 2016. **55**: p. 261-268.

18. Israr, H.A., K.J. Wong, and M.N. Tamin. *Numerical Simulations of Mixed-Mode II+III Delamination in Carbon/Epoxy Composite Laminate*. in *Modeling, Design and Simulation of Systems*. 2017. Singapore: Springer Singapore.

19. Rice, J., *A Path Integral and the Approximate Analysis of Strain Concentration by Notches and Cracks.* Journal of Applied Mechanics, 1968. **35**: p. 379-386.

20. Sarrado, C., A. Turon, J. Renart, and J. Costa, *An experimental data reduction method for the Mixed Mode Bending test based on the J-integral approach.* Composites Science and Technology, 2015. **117**: p. 85-91.

21. Zhao, Y., W. Liu, L.K. Seah, and G.B. Chai, *Delamination growth behavior of a woven E-glass/bismaleimide composite in seawater environment.* Composites Part B: Engineering, 2016. **106**: p. 332-343.

22. Healey, R., N.M. Chowdhury, W.K. Chiu, and J. Wang, *Experimental and numerical determination of mode II fracture toughness of woven composites verified through unidirectional composite test data.* Polymers and Polymer Composites, 2019. **27**(9): p. 557-566.

23. Chowdhury, N.M., W.K. Chiu, J. Wang, and P. Chang, *Experimental and finite element studies of bolted, bonded and hybrid step lap joints of thick carbon fibre/epoxy panels used in aircraft structures.* Composites Part B: Engineering, 2016. **100**: p. 68-77.

24. Chowdhury, N.M., J. Wang, W.K. Chiu, and P. Chang, *Experimental and finite element studies of thin bonded and hybrid carbon fibre double lap joints used in aircraft structures.* Composites Part B: Engineering, 2016. **85**: p. 233-242.

25. Franco, L.A.L., M.L.A. Graça, and F.S. Silva, *Fractography analysis and fatigue of thermoplastic composite laminates at different environmental conditions.* Materials Science and Engineering: A, 2008. **488**(1): p. 505-513.

26. Harris, B., *A historical review of the fatigue behaviour of fibre-reinforced plastics*. Fatigue in composites. 2003: Woodhead Publishing. 3-35.

27. Talreja, R., *1 - A conceptual framework for studies of durability in composite materials*, in *Fatigue of Textile Composites*, V. Carvelli and S.V. Lomov, Editors. 2015, Woodhead Publishing. p. 3-27.

28. Dieter, G.E., *Mechanical Metallurgy*. 3rd ed ed. 1988, McGraw-Hill,Boston,MA: Mc Graw-Hill Series in Material Science and Engineering.

29. Talreja, R., *Fatigue of Composite Materials: Damage Mechanisms and Fatigue-Life Diagrams.* Proceedings of the Royal Society of London. Series A, Mathematical and Physical Sciences, 1981. **378**(1775): p. 461-475.

30. Mandell, J.F., *Chapter 7 - Fatigue Behavior of Short Fiber Composite Materials*, in *Composite Materials Series*, K.L. Reifsnider, Editor. 1991, Elsevier. p. 231-337.

31. Basquin, O.H., *The exponential law of endurance tests.* Proc Am Soc Test Mater, 1910. **10**: p. 625-630.

32. Goodman, J., *Mechanics Applied to Engineering*. 1919, London: Longmans, Green and Co.

33. Smith, J.O., *The Effect of Range of Stress on the Fatigue Strength of Metals.* Bulletin No. 334. University of Illinois, Engineering Experiment Station, Urbana, IL,Feb. 1942. See also Bulletin No. 316, Sept. 1939., 1942.

34. Morrow, J., *Fatigue properties of metals, section 3.2. In: Fatigue Design Handbook, Pub. No. AE-4. Soc. of Automotive Engineers*. 1968: Warrendale, PA.

35. Smith, K.N., T. Topper, and P. Watson, *A stress–strain function for the fatigue of metals (stress-strain function for metal fatigue including mean stress effect).* Vol. 5. 1970. 767-778.

36. Walker, K., *The Effect of Stress Ratio During Crack Propagation and Fatigue for 2024-T3 and 7075-T6 Aluminum*, in *The Effect of Stress Ratio During Crack Propagation and Fatigue for 2024-T3 and 7075-T6 Aluminum*. 1970.

37. Dowling, N., C. Calhoun, and A. Arcari, *Mean Stress Effects in Stress-life Fatigue and the Walker Equation.* Fatigue & Fracture of Engineering Materials & Structures, 2009. **32**: p. 163-179.

38. Fatinah, T.S., K.S. Basaruddin, A.S.A. Rahman, and M.S.A. Majid, *Effect of mean stress and amplitude stress on mechanical stress-strain response of chopped strand mat (CSM) composite under cyclic load.* AIP Conference Proceedings, 2017. **1885**(1): p. 020094.

39. J., S.H. and M.J. F., *The effect of mean stress on damage predictions for spectral loading of fibreglass composite coupons.* Wind Energy, 2005. **8**(1): p. 93-108.

40. Mortazavian, S. and A. Fatemi, *Effects of mean stress and stress concentration on fatigue behavior of short fiber reinforced polymer composites*. Fatigue and Fracture of Engineering Materials and Structures, 2016. **39**(2): p. 149-166.

41. Lu, Z., B. Feng, and C. Loh, *Fatigue behaviour and mean stress effect of thermoplastic polymers and composites*. Vol. 12. 2018. 150-157.

42. Nijssen, R.M. *Fatigue Life Prediction and Strength Degradation of Wind Turbine Rotor Blade Composites*. 2006.

43. Ansell, M.P., I.P. Bond, and P.W. Bonfield, *Constant life diagrams for wood composites and polymer matrix composites.* 1993. **5**: p. 692-692.

44. F. Mandell, J. and H. J. Sutherland, *Optimized Goodman Diagram for the Analysis of Fiberglass Composites Used in Wind Turbine Blades*. 2005.

45. F. Mandell, J., D. D. Samborsky, N. K. Wahl, and H. J. Sutherland, *Testing and Analysis of Low Cost Composite Materials Under Spectrum Loading and High Cycle Fatigue Conditions*. 2019.

46. Miner, M.A., *Cumulative damage in fatigue.* American Society of Mechanical Engineers -- Journal of Applied Mechanics, 1945. **12**(3): p. -159---164.

47. Broendsted, P., Andersen, S I, and Lilholt, H, *Fatigue damage accumulation and lifetime prediction of GFRP materials under block loading and stochastic loading*. 1997: Denmark.

48. Reis, P.N.B., J.A.M. Ferreira, J.D.M. Costa, and M.O.W. Richardson, *Fatigue life evaluation for carbon/epoxy laminate composites under constant and variable block loading.* Composites Science and Technology, 2009. **69**(2): p. 154-160.

49. Adam, T., N. Gathercole, H. Reiter, and B. Harris, *Life prediction for fatigue of T800/5245 carbob-fibre composites: II. Variable-amplitude loading.* International Journal of Fatigue, 1994. **16**(8): p. 533-547.

50. Van Paepegem, W. and J. Degrieck, *Effects of load sequence and block loading on the fatigue response of fiber-reinforced composites.* Mechanics of Advanced Materials and Structures, 2002. **9**(1): p. 19-35.

51. Harris, B., N. Gathercole, H. Reiter, and T. Adam, *Fatigue of carbon-fibre-reinforced plastics under block-loading conditions.* Composites Part A: Applied Science and Manufacturing, 1997. **28**(4): p. 327-337.

52. Manjunatha, C.M., N. Jagannathan, K. Padmalatha, A.J. Kinloch, and A.C. Taylor, *Improved variable-amplitude fatigue behavior of a glass-fiber-reinforced hybrid-toughened epoxy composite.* Journal of Reinforced Plastics and Composites, 2011. **30**(21): p. 1783-1793.

53. Pochiraju, K.V., G. Tandon, G.A. Schoeppner, *Long-term durability of polymeric matrix composites.* Springer Science & Business Media, 2011.

54. Schoeppner, G.A. and M.S. Tillman, *Composite Structures Durability Design and Substantiation*, in *Long-Term Durability of Polymeric Matrix Composites*, K.V. Pochiraju, G.P. Tandon, and G.A. Schoeppner, Editors. 2012, Springer US: Boston, MA. p. 427-481.

55. Naik, R.A., *Durability of Composites in Aircraft Engine Applications*, in *Long-Term Durability of Polymeric Matrix Composites*. 2012, Springer. p. 597-624.

56. Military, M.-H.-f., *MIL-HDBK-17-3F: Composite Materials Handbook, Polymer Matrix Composites: Materials Usage, Design, and Analysis*. US Department of Defense. 17.

57. Schön, J. and T. Nyman, *Spectrum fatigue of composite bolted joints.* International Journal of Fatigue, 2002. **24**(2): p. 273-279.

58. Xiong, J.J. and R.A. Shenoi, *A load history generation approach for full-scale accelerated fatigue tests.* Engineering Fracture Mechanics, 2008. **75**(10): p. 3226-3243.

59. Dowling, N.E., *A Review of Fatigue Life Prediction Methods*. 1987, SAE International.

60. Veers, P., T. D. Ashwill, H. J. Sutherland, D. L. Laird, D. W. Lobitz, D. Griffin, J. F. Mandell, W. Musial, K. Jackson, M. Zuteck, A. Miravete, S.W. Tsai, and J. L. Richmond, *Trends in the Design, Manufacture and Evaluation of Wind Turbine Blades*. Vol. 6. 2003. 245-259.

61. Owen, M.J. and R.J. Howe, *The accumulation of damage in a glass-reinforced plastic under tensile and fatigue loading.* Journal of Physics D: Applied Physics, 1972. **5**(9): p. 1637-1649.

62. Bond, I.P. and I.R. Farrow, *Fatigue life prediction under complex loading for XAS/914 CFRP incorporating a mechanical fastener*. International Journal of Fatigue, 2000. **22**(8): p. 633-644.

63. Post, N.L., S.W. Case, and J.J. Lesko, *Modeling the variable amplitude fatigue of composite materials: A review and evaluation of the state of the art for spectrum loading.* International Journal of Fatigue, 2008. **30**(12): p. 2064-2086.

64. Chou, P.C. and R. Croman, *Residual Strength in Fatigue Based on the Strength-Life Equal Rank Assumption.* Journal of Composite Materials, 1978. **12**(2): p. 177-194.

65. Post, N.L., *Reliability based design methodology incorporating residual strength prediction of structural fiber reinforced polymer composites under stochastic variable amplitude fatigue loading. Diss*. 2008, Virginia Tech.

66. Sarkani, S., G. Michaelov, D. P. Kihl, and D. L. Bonanni, *Comparative Study of Nonlinear Damage Accumulation Models in Stochastic Fatigue of FRP Laminates*. Vol. 127. 2001.

67. Broutman, L. and S. Sahu, *A New Theory to Predict Cumulative Fatigue Damage in Fiberglass Reinforced Plastics*, in *A New Theory to Predict Cumulative Fatigue Damage in Fiberglass Reinforced Plastics*. 1972.

68. Hahn, H.T. and R.Y. Kim, *Proof Testing of Composite Materials.* Journal of Composite Materials, 1975. **9**(3): p. 297-311.

69. Reifsnider, K.L. and R. Jamison, *Fracture of fatigue-loaded composite laminates.* International Journal of Fatigue, 1982. **4**(4): p. 187-197.

70. Yao, W.X. and N. Himmel, *A new cumulative fatigue damage model for fibre-reinforced plastics.* Composites Science and Technology, 2000. **60**(1): p. 59-64.

71. Yang, J.N. and M.D. Liu, *Residual Strength Degradation Model and Theory of Periodic Proof Tests for Graphite/Epoxy Laminates*.* Journal of Composite Materials, 1977. **11**(2): p. 176-203.

72. D'Amore, A., M. Giorgio, and L. Grassia, *Modeling the residual strength of carbon fiber reinforced composites subjected to cyclic loading.* International Journal of Fatigue, 2015. **78**: p. 31-37.

73. Yang, J.N. and C.T. Sun, *Proof Test and Fatigue of Unnotched Composite Laminates.* Journal of Composite Materials, 1980. **14**(2): p. 168-176.

74. Damore, A. and L. Grassia, *Constitutive law describing the strength degradation kinetics of fibre-reinforced composites subjected to constant amplitude cyclic loading.* Mechanics of Time-Dependent Materials, 2016. **20**(1): p. 1-12.

75. D'Amore, A., M. Giorgio, and L. Grassia, *Modeling the residual strength of carbon fiber reinforced composites subjected to cyclic loading.* International Journal of Fatigue, 2015. **78**: p. 31-37.

76. Califano, A. and R. Dell'Aversano, *Theoretical approach to the study of fatigue of composites under spectrum loading.* AIP Conference Proceedings, 2018. **1981**(1): p. 020143.

77. Chowdhury, N.M., R. Healey, J. Wang, W.K. Chiu, and C. Wallbrink, *Using a residual strength model to predict mode II delamination failure of composite materials under block fatigue loading.* International Journal of Fatigue, 2020. **135**: p. 105563.

78. Gamstedt, E.K. and B.A. Sjögren, *An experimental investigation of the sequence effect in block amplitude loading of cross-ply composite laminates.* International Journal of Fatigue, 2002. **24**(2): p. 437-446.

79. Hosoi, A., H. Kawada, and H. Yoshino, *Fatigue characteristics of quasi-isotropic CFRP laminates subjected to variable amplitude cyclic two-stage loading.* International Journal of Fatigue, 2006. **28**(10): p. 1284-1289.

80. Koch, I., G. Just, M. Brod, J. Chen, A. Doblies, A. Dean, M. Gude, R. Rolfes, C. Hopmann, and B. Fiedler, *Evaluation and modeling of the fatigue damage behavior of polymer composites at reversed cyclic loading.* Materials, 2019. **12**(11).

81. Plumtree, A., M. Melo, and J. Dahl, *Damage evolution in a [±45]2S CFRP laminate under block loading conditions.* International Journal of Fatigue, 2010. **32**(1): p. 139-145.

82. Yao, L., Y. Sun, M. Zhao, R.C. Alderliesten, and R. Benedictus, *Stress ratio dependence of fibre bridging significance in mode I fatigue delamination growth of composite laminates.* Composites Part A: Applied Science and Manufacturing, 2017. **95**: p. 65-74.

83. Paris, P. and F. Erdogan, *A Critical Analysis of Crack Propagation Laws.* Journal of Basic Engineering, 1963. **85**(4): p. 528-533.

84. Irwin, G., *Analysis of Stresses and Strains near the End of a Crack Traversing a Plate*. Journal of Applied Mechanics, 1957. **24**: p. 361-364.

85. Hartman, A. and J. Schijve, *The effects of environment and load frequency on the crack propagation law for macro fatigue crack growth in aluminium alloys.* Engineering Fracture Mechanics, 1970. **1**(4): p. 615-631.

86. Krueger, R. *Development of a benchmark example for delamination fatigue growth prediction*. in *25th Technical Conference of the American Society for Composites and 14th US-Japan Conference on Composite Materials 2010, September 20, 2010 - September 22, 2010*. 2010. Dayton, OH, United states: DEStech Publications Inc.

87. O'Brien, T.K., W.M. Johnston, and G.J. Toland, *Mode II interlaminar fracture toughness and fatigue characterization of a graphite epoxy composite material.* 2010.

88. Matsubara, G., H. Ono, and K. Tanaka, *Mode II fatigue crack growth from delamination in unidirectional tape and satin-woven fabric laminates of high strength GFRP*. International Journal of Fatigue, 2006. **28**(10): p. 1177-1186.

89. Mall, S., G. Ramamurthy, and M.A. Rezaizdeh, *Stress ratio effect on cyclic debonding in adhesively bonded composite joints.* Composite Structures, 1987. **8**(1): p. 31-45.

90. Hosoi, A., Y. Arao, H. Karasawa, and H. Kawada, *High-cycle fatigue characteristics of quasi-isotropic CFRP laminates.* Advanced Composite Materials, 2007. **16**(2): p. 151-166.

91. Rans, C., R. Alderliesten, and R. Benedictus, *Misinterpreting the results: How similitude can improve our understanding of fatigue delamination growth.* Composites Science and Technology, 2011. **71**(2): p. 230-238.

92. Alderliesten, R.C., J. Schijve, and S.v.d. Zwaag, *Application of the energy release rate approach for delamination growth in Glare.* Engineering Fracture Mechanics, 2006. **73**(6): p. 697-709.

93. Jones Ac, R., S. Pitt, A.J. Bunner, and D. Hui, *Application of the Hartman–Schijve equation to represent Mode I and Mode II fatigue delamination growth in composites*. Vol. 94. 2012. 1343–1351.

94. Anilchandra, A.R., R. Bojja, N. Jagannathan, and C. Manjunatha, *Prediction of mode II delamination propagation life under a standard spectrum loading in a carbon fiber composite*. Vol. 51. 2017. 2827-2833.

95. Yao, L., R. Alderliesten, M. Zhao, and R. Benedictus, *Bridging effect on mode I fatigue delamination behavior in composite laminates.* Composites Part A: Applied Science and Manufacturing, 2014. **63**: p. 103-109.

96. Jones Ac, R., A. Kinloch, J. Michopoulos, A. J. Brunner, and N. Phan, *Delamination Growth in Polymer-Matrix Fibre Composites and the Use of Fracture Mechanics Data for Material Characterisation and Life Prediction*. Vol. 180. 2017. 316-333.

97. Khan, R., R. Alderliesten, S. Badshah, and R. Benedictus, *Effect of stress ratio or mean stress on fatigue delamination growth in composites: Critical review.* Composite Structures, 2015. **124**: p. 214-227.

98. C. Wallbrink, B.K., *Spectrum Truncation or Spectrum Compression? : When time and money matters and nothing less than a fraction of the original spectrum is acceptable*, in *ICAF 2017 Symposium*. 2017: Nagoya, Japan.

99. Vine, J., L. Krake, and B. Krieg. *Helicopter airframe fatigue spectra truncation and verification*. in *11th International Fatigue Congress, FATIGUE 2014, March 2, 2014 - March 7, 2014*. 2014. Melbourne, VIC, Australia: Trans Tech Publications Ltd.

100. Schubbe, J.J., *Evaluation of fatigue life and crack growth rates in 7050-T7451 aluminum plate for T-L and L-S oriented failure under truncated spectra loading.* Engineering Failure Analysis, 2009. **16**(1): p. 340-349.

101. Hailing, T., B. Rui, Z. Jianyu, Z. Xiaoling, and F. Binjun, *Influence of Low Load Truncation Level on Crack Growth for Al 2324-T39 and Al 7050-T7451.* Chinese Journal of Aeronautics, 2009. **22**(4): p. 401-406.

102. Bao, R. and X. Zhang, *Fatigue crack growth behaviour and life prediction for 2324-T39 and 7050-T7451 aluminium alloys under truncated load spectra.* International Journal of Fatigue, 2010. **32**(7): p. 1180-1189.

103. Homola, P., R. Růžek, and J. Běhal, *Effect of Loading Spectrum Clipping and Truncation on Fatigue Crack Growth Behavior of 7475-T7351 Aluminum Alloy under Variable Amplitude Loading.* Procedia Engineering, 2015. **101**: p. 203-210.

104. Wanhill, R.J.H., *Flight simulation fatigue crack growth testing of aluminium alloys: Specific issues and guidelines.* International Journal of Fatigue, 1994. **16**(2): p. 99-110.

105. Schijve, J., A.M. Vlutters, Ichsan, and J.C. ProvóKluit, *Crack growth in aluminium alloy sheet material under flight-simulation loading.* International Journal of Fatigue, 1985. **7**(3): p. 127-136.

106. Kujawski, D. and S. Stoychev, *Effects of spectrum modification on fatigue crack growth.* Fatigue and Fracture of Engineering Materials and Structures, 2010. **33**(3): p. 161-173.

107. Badaliance R, H.D., *Effects of fighter attack spectrum on composite fatigue life.* Air Force Wright Aeronaughtical Laboratories, 1981. **AFAWL-TR-81-3001**.

108. Clark, G. and T.J. Van Blaricum, *Load spectrum modification effects on fatigue of impact-damaged carbon fibre composite coupons.* Composites, 1987. **18**(3): p. 243-251.

109. Schön, J., *Spectrum fatigue loading of composite bolted joints—small cycle elimination.* International Journal of Fatigue, 2006. **28**(1): p. 73-78.

110. Strizhius, V., *Fatigue Damage Accumulation Under Quasi-Random Loading of Composite Airframe Elements.* Mechanics of Composite Materials, 2016. **52**(4): p. 455-468.

111. Phillips, E.P., *Effects of Truncation of a Predominantly Compression Load Spectrum on the Life of a Notched Graphite/Epoxy Laminate*, K.N. Lauraitis, Editor. 1981, ASTM International: West Conshohocken, PA. p. 197-212.

112. Cytec-Engineered-Materials, *CYCOM 977-3 Epoxy Resin Technical Data Sheet*. 2017.

113. Nelson, E., A. Hansen, D. Kenik, and T.-E. Tay. *Delamination and damage progression in a composite laminate subjected to bending using multicontinuum theory*. in *52nd AIAA/ASME/ASCE/AHS/ASC Structures, Structural Dynamics and Materials Conference, April 4, 2011 - April 7, 2011*. 2011. Denver, CO, United states: American Institute of Aeronautics and Astronautics Inc.

114. Hexcel-Corperation, *HexPly M18/1 180 C curing epoxy matrix product data*. 2015.

115. Brink, W.M.v.d., G.v.d. Vrie, and M. Nawijn, *Modelling and simulation of damage in woven fabric composites on meso-macro level using the independent mesh method.* International Journal of Materials Engineering Innovation, 2013. **4**(2): p. 84-100.

116. De Baere, I., W. Van Paepegem, and J. Degrieck, *On the feasibility of a three-point bending setup for the validation of (fatigue) damage models for thin composite laminates.* Polymer Composites, 2008. **29**(10): p. 1067-1076.

117. Anilchandra, A., R. Bojja, N. Jagannathan, and C. Manjunatha, *Variable amplitude fatigue testing to characterize mode II delamination in a polymer composite.* Transactions of the Indian Institute of Metals, 2016. **69**(2): p. 421-424.

118. Healey, R., N.M. Chowdhury, W.K. Chiu, and J. Wang, *Experimental and numerical determination of mode II fracture toughness of woven composites verified through unidirectional composite test data.* Polymers and Polymer Composites. **0**(0): p. 0967391119853736.

119. Dong, X., H. Zhao, L. Zhang, H. Cheng, and J. Gao, *Geometry effects in four-point bending test for thin sheet studied by finite element simulation.* Materials Transactions, 2016. **57**(3): p. 335-343.

120. Rizov, V., *Fibre Type Effect on Mixed-Mode I/II Interlaminar Fracture in Polymer Composites.* Polymers and Polymer Composites, 2016. **24**: p. 179-184.

121. Das, S., P. Choudhury, S. Halder, and P. Sriram, *Stress and Free Edge Delamination Analyses of Delaminated Composite Structure Using ANSYS.* Procedia Engineering, 2013. **64**: p. 1364-1373.

122. Esmaeel, R.A. and F. Taheri, *Delamination detection in laminated composite beams using the empirical mode decomposition energy damage index.* Composite Structures, 2012. **94**(5): p. 1515-1523.

123. O'Brien, T.K., W.M. Johnston, G.J. Toland, and L.R. Center, *Mode II interlaminar fracture toughness and fatigue characterization of a graphite epoxy composite material*. 2010: National Aeronautics and Space Administration, Langley Research Center.

124. Aicher W, B.J., van Dijk GM, Ertelt J, Hu¨ck M, de Jonge JB, et al, *Description of a fighter aircraft loading standard for fatigue evaluation FALSTAFF*. 1976.

125. Rouchon, J. *Fatigue and Damage Tolerance Evaluation of Structures: The Composite Materials Response*. in *25th symposium of the International Committee on Aeronautical Fatigue*. May 2009. Rotterdam, The Netherlands: National Aerospace Laboratory NLR.